The Loschmidt Echo in Disordered Systems

by

Ye Cheng CHEN

A Thesis submitted to the Faculty of Graduate Studies of

The University of Manitoba

in partial fulfilment of the requirements of the degree of

MASTER OF SCIENCE

Department of Physics and Astronomy

University of Manitoba

Winnipeg

Abstract

Anderson localization is a wave interference phenomena. The single-particle wave functions become localized for an arbitrary amount of disorder for one-dimensional disordered systems in the thermodynamic limit. The localization characteristics of disordered systems allows us to measure the sensitivity of time reversal in the presence of small perturbations, namely the Loschmidt echo, which indirectly shows dynamical phase transitions via the return rate function. For single-particle non-interacting problems, calculating the Loschmidt echo for large system sizes is straightforward. For many-particle interacting problems, however, it is computationally affordable only for small system sizes. Using both single-particle and many-particle Hamiltonian approaches, we numerically investigate the disorder-averaged Loschmidt echo and dynamical phase transitions for quantum quenches in the disordered SSH model and the disordered XXZ spin model where analytical solutions are not attainable. We show that dynamical phase transitions persist for weakly disordered systems and finite system sizes.

Acknowledgements

I, Ye Cheng Chen, would like to thank my supervisor Dr. Jesko Sirker for the invaluable opportunity to pursue graduate studies in physics and his ongoing assistance, support and encouragement throughout my thesis development. Words cannot express my feelings, nor my thanks for all your help. During this period, I was confronted with many obstacles and challenges, but I also met many friends and colleagues who offered me help when I really needed it. I appreiciate the helps from my friends and colleagues: Jinwei Rao, Ming Kai, Philip Jager, Max Kiefer, Andrew Urichuk, Kyle Monkman, Yutong Zhao, Ying Yang, Amin Naseri, and Susan Beshta. I am grateful for my committee members Dr. Johan van Lierop and Dr. Mario Bieringer for reviewing my thesis and providing positive feedbacks. I acknowledge the financial supports from the University of Manitoba Graduate Fellowship (UMGF) and my supervisor Dr. Jesko Sirker. I am grateful for the WestGrid Compute Canada for providing computational resources and support. Last but not least, I thank my wife, my son, my mother and my father for understanding and supporting my desire to pursue my dream in physics.

Contents

List of Tables

List of Figures

Chapter 1

Introduction

In the past few decades, the field of quantum condensed matter physics, which deals with the macroscopic and microscopic physical properties of matter, has shown rapid ongoing development. While it is concerned with “condensed" phases commonly seen in liquids and solids, recent interests focus on more exotic condensed phases, such as superconducting phases at low temperatures [13, 14], ferromagnetic and antiferromagnetic phases of spin systems [15, 16], and the Bose-Einstein condensates found in the experimental realization of ultra-cold atomic gases [4, 17, 18]. Semi-classical non-interacting theories for solid-state systems can be attributed to an underlying principle of adiabatic continuity[1] and fundamental symmetries. Perturbation theory works particularly well in a wide range of systems, in which elementary “quasi-particle" excitations are assumed as non-interacting, single particles. As the historical development of condensed matter physics gradually shifts attention from semi-classical solid state systems to strongly interacting quantum systems, semi-classical approaches for single-particle non-interacting systems become inadequate. Complication arises at a phase transition in interacting systems, where symmetries and adiabatic continuity are broken. In the symmetry-broken

[1] The principle of adiabatic continuity states that in the absence of an electronic phase transition, a non-interacting ground state evolves smoothly or adiabatically into the interacting ground state if the perturbation acting on the system is slow. A particle that starts from the nth eigenstate remains in the nth eigenstate simply picks up a phase factor [19].

phase, elementary excitations may represent a collective mode, a new kind of excitation involving the collective motion of particles very different from those of the initial non-interacting phase. Modern experimental developments in interacting quantum systems present formidable challenges to theorists. Theoretical approaches to various many-particle problems conceive the realm of quantum field theory in many particle physics, which constitutes the theoretical foundation for explanations of the many-particle, low-energy phenomena. On a truly microscopic level, all forms of quantum matter can be formulated as a many-particle Hamiltonian encoding the fundamental interactions of constituent particles, and quantum field theory successfully decodes all the information embedded in the Hamiltonian by means of the second quantization technique and quantum statistical mechanics. The quantum field theory description provides a vehicle to systematically identify, isolate and develop a set of low-energy theories of the collective field, including perturbation theory, mean-field theory, linear response theory, the renormalization group, topology and more [19, 20].

Quantum many-particle systems can be roughly divided into two subcategories: ordered and disordered systems. Ordered systems show certain types of symmetry, such as translational symmetry or magnetic ordering. Macroscopic ordered systems are commonly known as thermalizing systems, which upon varying the system temperature, break internal symmetries and turn into different phases of matter; for instance, a water droplet breaks the symmetry upon cooling and turns into an ice crystal. A phase transition has occurred during the process of turning gas into liquid or liquid into solid. Magnetic ordering takes place in strongly correlated systems when an internal magnetic field develops, leading to a so-called ferromagnetic order parameter. The concept of order parameter, introduced by

Lev Landau [21], is the central ingredient in understanding how complex systems transform themselves into new states at low temperatures. It has provided fundamental explanations for phase transitions which take place in thermalizing systems and strongly correlated systems near the critical point, including Ising ferromagnet, superfluid, superconductor, Heisenberg ferromagnet and Higgs field [20]. Thermalizing systems are temperature-driven systems which are in contact with external reservoirs. These systems can be described in thermodynamic equilibrium by statistical ensembles (i.e. canonical or grand-canonical ensembles), which are used to derive thermodynamic observable quantities from statistical mechanics, such as entropy, specific heat and free energy. A phase transition in this case corresponds to a discontinuity in derivatives of the free energy at the critical temperature, and the ergodic hypothesis holds. The ergodic hypothesis says that given a sufficiently long time the system can fully explore its own phase space[2] [22]. Strongly correlated systems are interacting many-body quantum systems. Although weakly interacting systems can be treated semi-classically by means of statistical ensembles, complication arises in interacting systems due to interactions among particles. This can lead to the presence of quantum magnetism in low dimension, interaction-induced frustration, superconductivity or topological properties. Studying and classifying physical properties in strongly correlated systems has been a grand enterprise for condensed matter physicists [23–28].

While studying ordered systems has been the mainstream of modern research, in recent years disordered quantum systems have also attracted much attention from researchers much owing to the wave-interference phenomenon known as the

[2] A phase space is a mathematical space where each point corresponds to position and momentum of a state in the system, with all points in the phase space representing all possible states of the system.

Anderson localization, in which the electron states are localized due to strong disorderness present in the system [29]. Disordered systems, in a broad sense, are quantum systems in absence of some symmetry or correlation. We can have a disordered system in a heat bath, and such system can thermalize. In the present context, however, disordered systems are isolated and often non-ergodic, localized systems which never thermalize. The classical Drude model treats electrons as a homogeneous gas of non-interacting, mobile charge carriers capable of delivering electricity upon applying an external field, but it failed to explain why electrons can travel over long relaxation time before being scattered off of lattice ions [30, 31]. In quantum mechanics, the scattering behavior of electrons, as explained with the Bloch's theorem, was due to the periodic potential being disturbed [32]. The sources of disturbance are mainly due to the static or dynamic source, and the resulting scatterings are known as ionized impurity scattering or lattice scattering, respectively. Lattice scattering leads to temperature-dependent electrical resistivities in metals. On the contrary, the ionized impurity scattering leads to temperature-independent resistivities in semiconductors, which can generate free charge carriers by doping exotic atoms known as impurities ([32, 33]). The more heavily a semiconductor is doped, the higher the probability that a charge carrier will collide with an ion in a given time, the smaller the relaxation time between collisions, and hence the lower the conductivity. Semiconductors serve as the controllable medium for electron transportation (and thermal conduction), and electron scattering can easily be envisaged as zigzagging between impurities [34–36].

The development in both condensed matter physics and random matrix theory laid solid foundations for the success of Anderson's localization theory. The linear

combination of atomic orbitals (LCAO) method, which was used to describe the intermolecular bonding of diatomic molecules, was among the first signs of quantum approach in solid-state systems [37–39]. Bloch's theorem set the foundation for the principle of electronic band structure and theories in crystals, in understanding how electrons behave in solids from the quantum level, such as x-ray emission bands of metals [40, 41]. The tight-binding model is an oversimplified model which assumes electrons in the Bloch wavefunction. Not only does the TB model make possible the intermolecular calculations by reinforcing translational symmetry in crystal lattices, but it also works particularly well in cases where the bandwidth is small and the electrons are strongly localized in insulators [42]. It also provides a basis for many-particle problems, where interactions between atomic sites can be treated as perturbations. In the 1950s, an experiment performed by George Feher's group discovered the strange existence of long relaxation time of electron spins–and hence low conductivity–in highly-doped semiconductors. It was strange because by increasing the concentration of impurities the internal structure of the lattice would be randomly disordered, and from classical approaches the diffusive and transfusive motion of electrons was rather expected to increase than to decrease [3]. This experiment contradicts the classical theory that a high concentration of impurities would drastically stop electrical conduction. In 1958 Philip W. Anderson published a famous article about diffusion processes in disordered lattices, and using the TB model combined with a disordered potential distribution, he was able to explain fundamentally how electrons are localized and electrical conduction is absent if the degree of disorder is sufficiently large in the lattice [29].

Disordered systems are a simple application of the random matrix theory, which originates from the concept of a random walk but reaches far beyond the current

context. In 1905 Albert Einstein explained that the Brownian motion of large pollen grains in water is the consequence of countless random collisions from water molecules [43–45]. The process in which each successive step is statistically indepedent and continuous gives rise to the concept of the continuous-time random walk (CTRW). The CTRW provides good background for studying Markovian processes, Tauberian theorems and resistance networks in disciplines such as chemistry, neurology, finance and others [46, 47]. Particle movement in solid-state systems can also be modelled using the CTRW, assuming the presence of intermolecular hoppings between lattice sites and on-site energy potential [48]. Experimental advances of the CTRW include nuclear magnetic resonance (NMR) spectroscopy, which measures atomic and electronic structures in crystals by applying an external magnetic field [49, 50]. Theoretical advances of the CTRW include quantum random walk on graphs, which leads to the random matrix theory (RMT) and quantum statistics in disordered systems [51–53]. The RMT was first introduced by Eugene Wigner in 1955 to model the system of nuclei of heavy atoms, in which the on-site potentials due to heavy atoms could resemble the eigenvalues of a random symmetric matrix [54]. In subsequent theoretical studies for disordered systems, random matrices have often been used to model disordered Hamiltonians in the mean field approximation [55]. Anderson localization can be verified using ultra-cold atoms experiments for disordered systems [17, 56].

The Loschmidt echo is defined as the overlap between quantum states evolved with different Hamiltonians and measures the sensitivity of quantum evolution to perturbations [10]. The concept of the Loschmidt echo comes from the idea of statistical time-reversibility proposed by the Austrian physicist Joseph Loschmidt. He suggested that by reversing velocities of all particles in a system, one would

reverse the entire system from the current state to the previous state, seemingly decreasing the entropy and violating the second law of thermodynamics. Even though reversing velocity is impossible due to the fact that time “moves" in the forward direction, simply reversing the sign of the system Hamiltonian in quantum systems, with few degrees of freedom, provides a quantum implementation of the Loschmidt echo. The Loschmidt echo is more of a tool than a concept, and the main focus of using the Loschmidt echo is to understand many-body localized phases and quantum decoherence in many-particle, non-ergodic problems [57]. Because information is lost from a system into the external reservoir, decoherence is a key feature in thermalizing systems. The dynamics are non-unitary and irreversible [58]. For systems isolated from any environment, typically by sophisticated cooling procedures in ultra-cold atoms experiments, the system's energy is conserved and the dynamics are unitary. No information is lost and the entire dynamics can be reversed by flipping the sign of the system's Hamiltonian, achieving Loschmidt's proposal [59]. Aside from the trivial case just mentioned, it is more interesting to use the Loschmidt echo in systems that experience quantum quenches – a sudden change in the system so that the final Hamiltonian is different from its initial one. While the first Loschmidt echo experiment owes much to the Spin echo experiment in 1955 [60], both theoretical and experimental advances in studying the Loschmidt echo are manifold, including the Bose-Hubbard model, XXZ model, optical lattices and more [61–63]. It has been suggested that decoherence in certain systems sets limitations for quantum computing [64]. Since the Loschmidt echo measures the stability of time-reversal processes, it can potentially contribute to the development of quantum computing [63, 65].

With this introductory background, we will discuss more in detail in subsequent chapters. To prepare for the discussion of the Loschmidt echo in disordered systems, we begin in Chapter 2 by deliberating the notions of thermalization and localization. In Chapter 3 we discuss in detail the two models for the research project – the Su-Schrieffer-Heeger (SSH) model and the XXZ model. The SSH model is a topological model which shows edge states, while the XXZ model is an interacting spin system in which anisotropic spin-spin interactions are present [66]. We will introduce disorderness in the models and investigate the Loschmidt echo. We include a brief introduction to both static and dynamical phase transitions in Chapter 4 because the Loschmidt echo indirectly provides information about dynamical phase transitions. We present a formal and detailed introduction to the Loschmidt echo in Chapter 5. While the generalized Loschmidt echo formula allows to solve many-particle problems, there is another formula which we can use to evaluate single-particle physics in large system size. We provide verification of two Loschmidt echo formulae in single-particle and many-particle problems. Last but not least, we present our research results in Chapter 6, for the purpose of understanding dynamical phase transitions in interacting disordered systems and non-interacting ones.

Chapter 2

Disordered System

In condensed matter physics, an ordered system usually refers to the presence of certain symmetries or correlations in systems. The degree of freedom that is ordered can be translational (crystalline ordering), rotational (ferroelectric ordering), or a spin state (magnetic ordering). Examples of translationally ordered systems include ideal crystals at low temperatures, where the atoms of the material in the ground state show ordered lattice arrangement. In statistical thermodynamics, an ordered quantum statistical system can be either an open or a closed system. An open system is a quantum system that is in contact with its environment. Upon heating the system with an external reservoir, each atom gains kinetic energy and the system becomes disordered. This is the typical example of order-disorder transition commonly used to describe phase transitions among solids, liquids and gases due to the change in temperature. Not only can phase transitions take place in open systems, they can also occur in closed systems.

A closed (isolated) quantum system is a quantum statistical system that is isolated from external reservoirs so that there is no energy fluctuation or particle exchange. If a closed system reacts to an arbitrary local perturbations, under the unitary time evolution, the state of an ergodic system leads to thermalization, and the system becomes thermal and conducting. On the other hand, ergodicity can be simultaneously broken in localized systems due to strong disorder potential, and

the system becomes insulating. Localized systems are of interest for possibilities of storing quantum information for they can retain local details of the initial state, whereas thermalization hides information about the system's initial state, making it inaccessible after long times [1]. Anderson localization is a single-particle localization interference phenomenon for closed quantum systems, and it is in contrast to many-body localization where interactions among particles are taken into consideration.

The historical development of Anderson localization originated from the fact that electron conduction is absent in insulators. Classical theory predicts that the electronic conductivity is proportional to the mean free path, and the electrons are envisaged as zigzagging between impurities. The more impurities, the smaller the mean free path, so the lower the conductivity. The wave character of electrons, therefore, persist and electrons behave diffusively. However, the truth is that beyond a critical amount of impurities in a crystal, or the degree of disorder in the lattice is sufficiently large, the diffusive motion of electrons is completely absent. This phenomenon is known as Anderson localization [29]. This sudden reduction in conduction is associated with the localization of the electronic wavefunction. In 1977, Anderson was jointly awarded the Nobel Prize for the theoretical breakthrough of the electronic structure of disordered systems. For an interacting many-body, ergodic system, one expects a phase transition between an ergodic and a localized phase. In this chapter, we will focus on the discussion of Anderson localization and many-body localization but first briefly discuss thermalization.

2.1 Thermalization

Quantum statistical mechanics relates the thermodynamic quantities of a system to the Hamiltonian H of the single-particle or many-particle assembly. In the general, the grand canonical statistical ensemble describes open systems in contact with external reservoirs at thermodynamic equilibrium. For open systems, particles can enter or exit the system and energy exchange with the reservoir is allowed. The grand canonical ensemble is characterized by both chemical potential μ and temperature $T = 1/k_B\beta$, where k_B is the Boltzmann's constant. The grand canonical partition function Z_G is defined as

$$Z_G \equiv \sum_N \sum_j e^{-\beta(E_j - \mu N)} = \mathrm{Tr}(e^{-\beta(\hat{H} - \mu\hat{N})}),$$

where j denotes the set of all states for a fixed number of particles N, and the sum implies that the trace is over both j and N. $\hat{H}$ is the Hamiltonian operator representing observables in the system, and $\hat{N}$ is the occupation number operator. The partition function is directly related to the thermodynamic potential Ω via $\Omega(T, V, \mu) = -k_B T \ln Z_G$, which allows us to compute all the macroscopic equilibrium thermodynamics, such as entropy, pressure, number of particles, etc. [67]. The corresponding statistical operator $\hat{\rho}_G$ is given by

$$\hat{\rho}_G = e^{\beta(\Omega - \hat{H} - \mu\hat{N})}.$$

For any operator $\hat{O}$, the ensemble average $\langle\hat{O}\rangle$ is given by

$$\langle\hat{O}\rangle = \mathrm{Tr}(\hat{\rho}_G\hat{O}) = \mathrm{Tr}(e^{-\beta(\Omega - \hat{H} - \mu\hat{N})}\hat{O}) = \frac{\mathrm{Tr}(e^{-\beta(\hat{H} - \mu\hat{N})}\hat{O})}{\mathrm{Tr}(e^{-\beta(\hat{H} - \mu\hat{N})})}.$$

Therefore, a quantum system in thermodynamic equilibrium can be fully characterized by a small number of parameters (temperature, chemical potential, etc.). For a closed quantum system, the chemical potential is zero ($\mu = 0$) and energy exchange with the reservoir is absent. The quantities above can be described by canonical ensembles

$$Z_c = \mathrm{Tr}(e^{-\beta\hat{H}}),\ \hat{\rho}_c = e^{\beta(\Omega-\hat{H})},\ \ \langle\hat{O}\rangle_c = \frac{\mathrm{Tr}(e^{-\beta\hat{H}}\hat{O})}{\mathrm{Tr}(e^{-\beta\hat{H}})}.$$

Thermodynamic quantities can be approached by quantum statistics, and the time evolution of a quantum system can be treated using the formalism of probability [68]. To understand how the system evolves, one can define the time evolution operator as

$$U(t) = e^{\frac{-iHt}{\hbar}}.$$

Here we set $\hbar = 1$ from henceforth. If the system is prepared in an initial state $|\psi_0\rangle$ at time $t = 0$, then the system state at an arbitrary later time t can be described by $|\psi(t)\rangle = U(t)\,|\psi_0\rangle$. If the Hamiltonian H is both time-independent and hermitian, $U(t)$ is known as the unitary time operator, meaning that the total probability must remain fixed as the state of the system evolves in time: $U(t)^\dagger U(t) = 1$. The probability operator $\rho(t)$ that describes the time evolution process is defined as

$$\rho(t) = e^{\frac{-iHt}{\hbar}}\rho(t=0)e^{\frac{iHt}{\hbar}},\ \text{with}\ i\hbar\frac{d\rho}{dt} = [H,\rho].$$

Because the probability of the existing quantum system does not change in time, the total probability of all time-evolved states is conserved: $\mathrm{Tr}\{\rho\} = 1$. Since all other operators $\hat{O}$ are assumed to be time-independent, the expectation value at

time t of an observable O with the corresponding operator $\hat{O}$ is $\langle \hat{O} \rangle_t = \mathrm{Tr}\{\hat{O}_\rho(t)\}$. As a side note, the commutation property of the Hamiltonian H is non-trivial in a closed system. Although H is a sum of local operators[1] in a closed system, H only commutes with a complete linearly independent set of operators, which consists of global operators projecting onto the exact many-body eigenstates of H, known as projection operators. That is, H does not commute with global or local operators, but only the linear combination of projection operators. Particle number N, for instance, may not commute with H, but a larger conserved quantity consisting of N may commute with H.

Quantum thermalization is the process of a closed quantum system going into thermal equilibrium after an arbitrarily long time. The problem associated with thermalization is that this process erases the system's memory and all other details about its initial state. The method of unitary time evolution described above, moreover, can hide the memory of the local properties of the system's initial state if the system thermalizes, so that the information about the initial state at a long time is inaccessible. This is the process of decoherence. One way to thermalize a closed system is to split the system into two subsystems A and B. For a closed system characterized by only temperature T, thermalization means that at long times the state of subsystem A is as if it were at thermal equilibrium in contact with a reservoir B, which contains all the degrees of freedom not in A [1]. If we define the degrees of freedom within A by k-local operators with finite k, then the number of degrees of freedom in A goes to zero when we take the thermodynamic limit on the number of degrees of freedom in B (long time and large system size).

[1] A k-local operator is an operator $\hat{O}_k$ in which k of the entries are not identity operators, and a global operator is a k-local operator in which k is of order N [1].

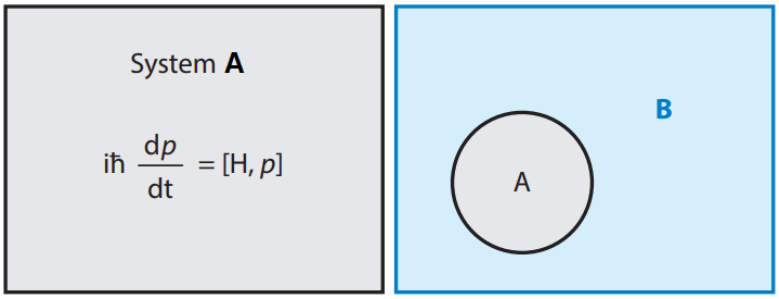

FIGURE 2.1: Left: The closed system that undergoes unitary time evolution. Right: The partition of the closed quantum system into a subsystem A and everything else B. If the system quantum thermalizes, then the region B is able to act as a reservoir for the subsystem A. Republished with permission of [Ye Cheng Chen], from [Many-body localization and thermalization in quantum statistical mechanics, Rahul Nandkishore and David A Huse, Annu. Rev. Condens. Matter Phys., Vol. 6, 2015]; permission conveyed through Copyright Clearance Center, Inc.

Fig. 2.1 shows the partition of a closed system split into a subsystem A and everything else B.

By taking the thermodynamic limit on B, there is a sequence of systems and their Hamiltonians, with the number of degrees of freedom increasing without limit. For a set of initial states of each system in the sequence, $\rho(t=0)$, they thermalize to a given temperature T. At thermal equilibrium, each system has an equilibrium expectation value of the total energy $\langle H \rangle_T$ and a Boltzmann probability operator $\rho^{(eq)}(T)$ at temperature T. Since the probability operator $\rho_A(t)$ of subsystem A at time t is defined as the partial trace over all of the degrees of freedom in B, $\rho_A(t) = \mathrm{Tr}_B\{\rho(t)\}$, the closed system thermalizes for this temperature in the thermodynamic limit so that $\rho_A(t) = \rho_A^{(eq)}(T) = \mathrm{Tr}_B\{\rho^{(eq)}(T)\}$.

There are two immediate consequences for a closed system that thermalizes: the eigenstate thermalization hypothesis (ETH) and the entanglement entropy. Consider an eigenstate $|\Psi_\alpha\rangle$ of the Hamiltonian H with energy $E_\alpha = \langle H \rangle_{T_\alpha}$ at

thermal equilibrium. The ETH states that the expectation value $\langle\Psi_\alpha|\hat{O}|\Psi_\beta\rangle$ of a local operator $\hat{O}$, in an eigenstate $|\Psi_\alpha\rangle$ of the Hamiltonian H with energy E_α, of a large interacting many-body system equals the thermal average $\langle O\rangle(E_\alpha)$ [69–71]:

$$\langle\Psi_\alpha|\hat{O}|\Psi_\beta\rangle = \langle O\rangle(E_\alpha).$$

The ETH has two strong implications. First, it asserts that in the thermodynamic limit the subsystem A is at thermal equilibrium: $\rho_A^{(\alpha)} = \rho_A^{(eq)}(T_\alpha)$. Secondly, because the expectation value of a local operator in eigenstates looks thermal, the ETH implies that every eigenstate implicitly contains a thermal state. That is, since an eigenstate is a pure state and not a mixed state, there is no time evolution of the system: $\rho(t) = \rho(0)$. If the system is initially prepared in an eigenstate, then thermalization of all such initial states implies that all many-body eigenstates of H are thermal.

For a closed system thought to be in its pure state $\rho = |\Psi\rangle\langle\Psi|$, the von-Neumann entropy is defined as $S(\rho) = -\mathrm{Tr}(\rho\ln\rho)$. The entanglement entropy (EE) for the subsystem A is the von-Neumann entropy of the reduced states, given by

$$S(\rho_A) = -\mathrm{Tr}(\rho_A\ln\rho_A),$$

where $|\Psi\rangle$ is an eigenstate of H, and $\rho_A = \mathrm{Tr}_B\{|\Psi\rangle\langle\Psi|\}$ is the reduced density matrix of ρ on subsystem A. Let the volume of the subsystem A denoted by L^d. The subsystem A is said to be maximally entangled when all 2^{L^d} coefficients are of equal weight, leading to volume-law entanglement $S_A \sim L^d$. In the case of thermalization, the entanglement entropy between A and B in this eigenstate of

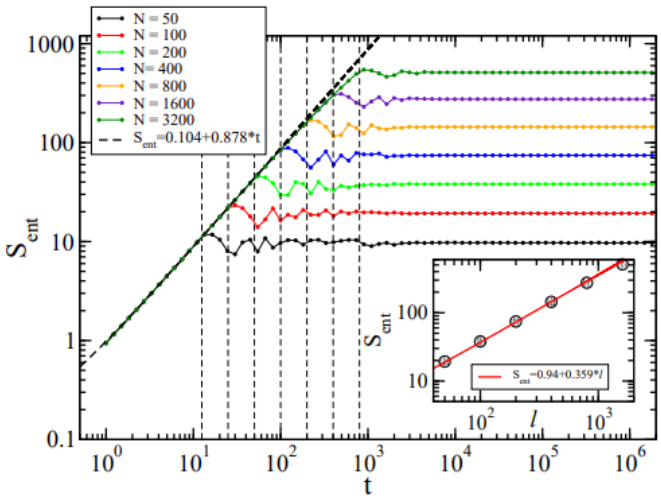

FIGURE 2.2: Entanglement entropy for the open XX chain for different system size N with box potential weak disorder $W = 0.1$. Reprinted (figure) with permission from [2] as follows: [Y. Zhao *et al.*, Entanglement entropy of disordered quantum chains following a global quench, Phys. Rev. B, 93(20):205146, 2016.] Copyright (2019) by the American Physical Society.

the full system is equal to the equilibrium thermal entropy of the subsystem A. Each system in the sequence behaves as a maximally entangled state [72]. The EE in thermalizing systems obeys volume-law scaling (whereas in localized systems it obeys the area-law scaling). For 1D systems, the EE is expected to obey the linear-law scaling in the thermodynamic equilibrium limit, but it is impossible to test numerically the many-body eigenstates of the system's Hamiltonian using exact diagonalization for large system size, not even for systems in the thermodynamic limit. Fig. 2.2 shows that the EE is indeed linear increasing with respect to the system length l in the regime $vt < l$, where v is the velocity of the excitations. For $vt > l$, EE then saturates due to system size being finite. It is nearly impossible to prepare exact eigenstates of H in the laboratory as initial states, but pure state of the system can be prepared by utilizing a Bose-Einstein condensate of ^{87}Rb (rubidium) atoms in optical lattice [73]. The entanglement entropy is minimized

if the system is in a non-degenerate pure ground state.

In short, if a closed system thermalizes, the memory of initial states are hidden in global operators at long times, the ETH is true in both the thermodynamic limit and for small regime in finite systems, and the entanglement entropy is maximized. On the other hand, as we will discuss in the following, for localized systems, some memory of local initial conditions are preserved in local observables at long times, the ETH fails, and the electron conductivity is absent.

2.2 Anderson Localization

In the original tight-binding model formulated by Philip W. Anderson, electrons are able to tunnel between neighbouring lattice sites, and the system is subject to an external random potential modeling the random environment. Consider a three-dimensional periodic lattice of potential wells, the time-dependence of the probability amplitude ψ_j for a particle on site j is described by the Schrödinger equation

$$i\hbar\dot{\psi}_j = H_j\psi_j,$$

where the Hamiltonian H_j is given by

$$H_j = E_j + \sum_{j\neq k} V_{jk}.$$

Here E_j is an independent random potential uniformly distributed in a disorder potential box $[-W, W]$, and V_{jk} the overlap (interaction) matrix element that allows electron hopping from one site to the next. In the second quantization representation, the Hamiltonian H is described by the operator $\hat{H}$ for a tight-binding model

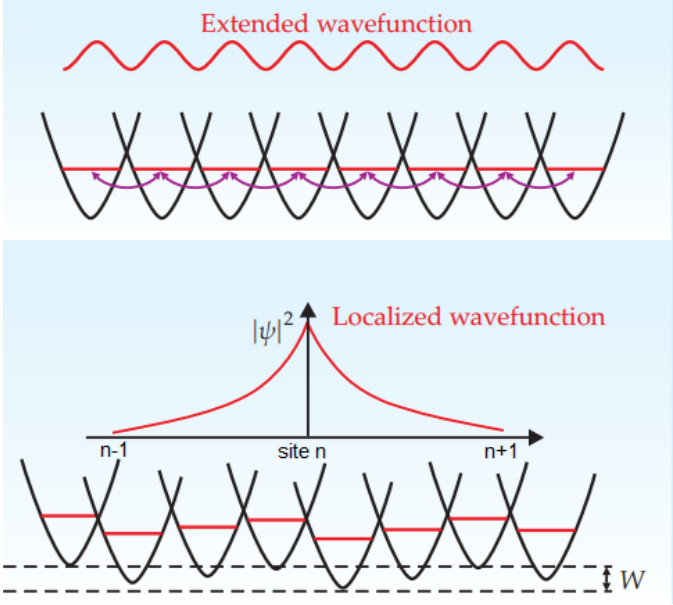

FIGURE 2.3: Hopping electrons or scattered waves. Top: Extended wavefunction of electrons due to quantum tunnelling. Bottom: Random on-site disorder potential results in localization of wavefunction which decays exponentially in space (the horizontal axis). Figure reproduced from [Alain Aspect and Massimo Inguscio, Anderson localization of ultracold atoms, Physics Today, Vol. 62 (8):30-35, 2009], with the permission of the American Institute of Physics.

with nearest-neighbor hopping and random on-site potential

$$\hat{H} = J \sum_{j,k} (\hat{c}_j^\dagger \hat{c}_k + h.c.) + \sum_j \mu_j \hat{c}_j^\dagger \hat{c}_j, \tag{2.1}$$

where μ_j is a static random on-site potential drawn from $[-W, W]$ with W measuring the disorder strength, $J \neq 0$ is the nearest-neighbour hopping amplitude, and $c_j^\dagger$ (c_j) creates (annihilates) a particle on site j. $h.c.$ stands for hermitian conjugate of other terms.

If one neglects the contribution from the disorder potential, $\mu_j = 0$, then the hopping behavior of electrons can have wave characteristics. The Schrödinger

equation yields a stationary-state solution of an extended wave function, which describes electrons as entities propagating freely in a crystal. The extended wave function is also known as the Bloch wave, $\psi_n = \exp(ikn)$, for $k \in [-\pi, \pi]$. The energy spectrum is given by the dispersion relation $E(k) = 2J\cos k$.The electron eigenstates are known as extended states [74]. On the other hand, starting with ψ_0 localized at site n at initial time $t = 0$, Anderson was interested in how fast the probability distribution $|\psi|^2$ spreads by considering the disorder strength W. He found that for three-dimensional lattice systems, "if $V(\mathbf{r}_{jk})$ falls off at large distances faster than $1/\mathbf{r}^3$, and if the average value of V is less than a certain critical V_c of the order of magnitude of W; then there is actually no transport at all, in the sense that even as $t \to \infty$ the amplitude of the wave function around site n falls off rapidly with distance, the amplitude on site n itself remaining finite" [29]. This is the original theorem of the Anderson localization. Fig. 2.3 shows both the extended and localized states of hopping electrons.

The scaling theory of localization generalizes the localization transition in finite, open media. Edwards and Thouless put forward the scaling theory with a dimensionless scale parameter g that defines the average conductance [75]. Later Abrahams *et, al* presented the the scaling function $\beta(g)$ that describes how average conductance g grows with system size L for a disordered system [76],

$$\beta(g) = \frac{d \log g}{d \log L}.$$

For a system in d-dimension, the conductance is given by $G(L) \propto L^{D-2}$, so $\beta(g) \propto d-2$ for large g. The beta function is positive for $d = 3$, zero for $d = 2$ and negative for $d = 1$. Fig. 2.4 shows the schematic diagram of the scaling theory. The sign of

the beta function changes from positive to negative as we transition from extended states to localized states. For $d \leq 2$, electron eigenstates can only appear to be quasi-extended or localized; for $d = 1$, any particle state is localized. For $d = 3$, $\beta(g)$ moves from $\log g > 0$ to $\log g < 0$ either by increasing size L (always positive) or decreasing conductance g, and the electron eigenstates move from extended states to localized states. This is the essential criterion for Anderson localization which asserts that electron eigenstates are localized for the average conductance $\log g < 0$.

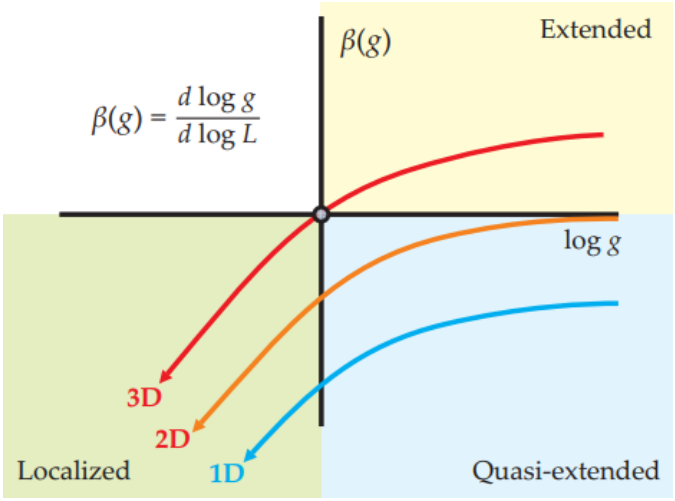

FIGURE 2.4: Scaling theory of localization. Figure taken from Ref. [3]. Figure reproduced from [A. Lagendijk *et al.*, Fifty years of Anderson localization, Physics Today, Vol. 62(8):24-29, 2009], with the permission of the American Institute of Physics.

Localization is possible in 1D, 2D and 3D systems when the average conductance is below certain threshold $\log g < 0$. Anderson localization has the following ramifications:

- For 1D or 2D systems with an arbitrary disorder strength W, and for $D \geq 3$

and sufficiently large W, the electron eigenstates are all exponentially localized. The wave function $\psi_\alpha(\mathbf{r})$ of an eigenstate α corresponding to a given energy is localized and has the following asymptotic form

$$|\psi_\alpha(\mathbf{r})|^2 \propto \exp\left(-\frac{|\mathbf{r}-\mathbf{R}_\alpha|}{\xi_{loc}}\right),$$

where $\mathbf{R}_\alpha$ is the position where state α is localized. ξ_{loc} is the localization length at which an electron is localized, and it depends on the disorder strength and the energy [1, 77]. For 1D system with finite system size L, all electron eigenstates are localized if the system length is longer than the localization length: $L > \xi_{loc}$.

- If $D \geq 3$ and W is small, then

$$|\psi_\alpha(\mathbf{r})|^2 \propto \frac{1}{V},$$

where V is the volume of the system [77].

- Using diagrammatic perturbation theory and transfer matrix techniques, one can show that the 1D localization length is given by [78]

$$\xi_{loc} = \frac{12(4-E^2)}{W^2}, \tag{2.2}$$

where $E(k) = 2J\cos k$ is the dispersion relation of the single-band model (2.1). Fig. 2.5 shows the localization length ξ as a function of disorder parameter W and energy E, where ξ_{loc} is described by the power law $\xi_{loc} \propto W^{-2}$.

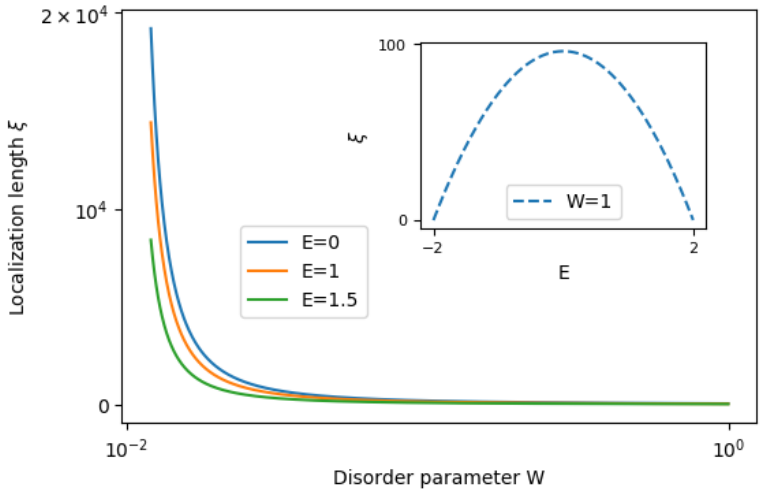

FIGURE 2.5: The plot of localization length ξ in 1D as a function of disorder parameter W and dispersion relation E (inset) using Eq. (2.2).

Because electrons repel each other and are affected by lattice vibrations – a kind of disorder that is not static and cannot produce Anderson localization – experimental observation of Anderson localization was not realized until recent advances in experimental techniques. Localization has been experimentally reported in microwaves [79, 80], sound waves [81], electron gases [82], and matter-waves [83]. Here we look at Anderson localization of ultracold atoms. Ultracold atoms, typically a quantum gas of bosons, can be cooled down to near absolute zero temperature, and interactions among particles can be tuned by using a static magnetic field, known as the Feshbach resonance [4, 84]. Those bosons occupy the ground state where kinetic energy is minimized, and microscopic wavefunction interference can be observed macroscopically: Many independent atoms appear in the same single-atom wavefunction. This is known as the Bose-Einstein condensate (BEC). Fig. 2.6 shows the Anderson localization of ultracold atoms. The Bose-Einstein condensates are confined by a matter waveguide transverse to the z-axis, in which

they are allowed to move freely. When a laser beam creates a disordered intensity pattern that varies rapidly along z, the atoms stop moving after a short time. A stationary density profile with exponentially decaying wings confirms the Anderson localization [4].

In short, Anderson localization is a single-particle localization phenomenon in disordered systems, and it is confirmed using ultracold atoms experiments. Having introduced the concepts of thermalizing systems and localized systems, we can now tell the difference between them. For a closed system to become localized, the ETH fails for the initial state, so it is impossible to thermalize the system. If we transform Eq. (2.1) into a Hamiltonian in the basis of eigenstates which are non-interacting many-particle eigenstates corresponding to product of single-particle eigenstates, then for systems in which at least some of the single-particle states are localized, almost all of the many-particle states violate the eigenstate thermalization hypothesis (ETH).

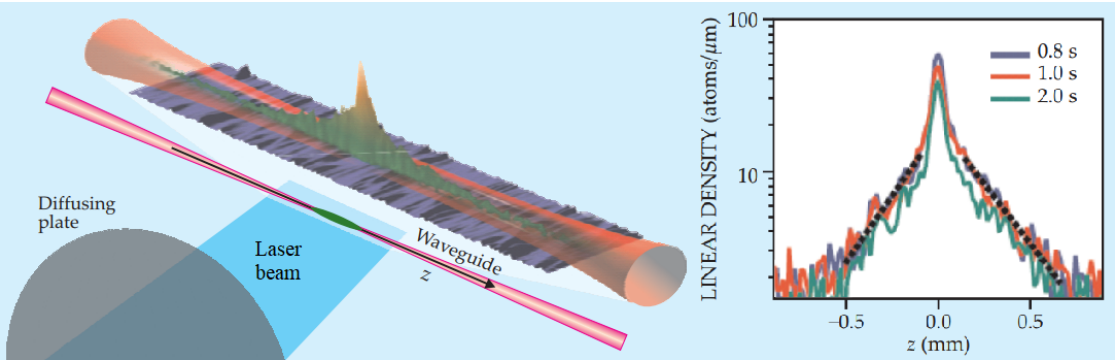

FIGURE 2.6: Anderson localization of ultracold atoms. The semilog plots of the profiles at times 0.8 s, 1 s, and 2 s confirm the localization. Figure reproduced from [4]. Figure reproduced from [Alain Aspect and Massimo Inguscio, Anderson localization of ultracold atoms, Physics Today, Vol. 62 (8):30-35, 2009], with the permission of the American Institute of Physics.

2.3 Many-body Localization

Many-body localization (MBL) is the generalization of Anderson localization to disordered interacting many-particle systems. The physics of the MBL phenomenon is most simply exposed in the context of spin models. A spin-1/2 model of MBL arises in a system governed by the spin Hamiltonian

$$H = \sum_{ij} J_{ij} \boldsymbol{\sigma}_i \cdot \boldsymbol{\sigma}_j + \sum_i \mu_i \sigma_i^z \tag{2.3}$$

The on-site disorder potential μ_i are static random variable drawn from a continuous probability distribution of width $W > 0$, and the spin hoppings and interactions J_{ij} are short range in real space.

At $J = 0$ the system is fully localized. For none-zero J, in the regime $J << W$, the many-body eigenstates of Eq. (2.3) on different sites are weakly characterized by J but subject to strong disorder W. Hence, for strong disorder, DC spin transport and energy transport are absent, quantum thermalization therefore does not occur, and all of the eigenstates violate the ETH [85]. This is the MBL phase. For weak disorder, the high-energy entropy eigenstates of Eq. (2.3) do obey the ETH, and the eigenstates are at the thermal phase. There is a quantum phase transition between the thermal phase and the MBL localized phase by varying the disorder strength. Questions about the nature of this phase transition remain open.

The main difference between the single-particle localization and many-particle localization is dephasing and the spreading of entanglement. The following argument follows from Ref. [1]. One can use Eq. (2.3) to describe a system of N-local, two-state degrees of freedom $\{\boldsymbol{\sigma}_i\}$. These are called p-bits and represent physical

many-particle localized states in real space. For strong disorder, the Hamiltonian can be in the fully many-body-localized (FMBL) regime, where all the many-body eigenstates of the Hamiltonian are localized and can be described by a set of localized two-state degrees of freedom $\{\boldsymbol{\tau}_i\}$. These many-particle localized eigenstates in an eigenbasis are called l-bits. Fig. 2.7 shows dynamical behavior of the l-bits. Localized l-bits exist for FMBL systems, and the overlap between each such l-bit and a distant p-bits is exponentially small [1, 86–88]. Eq. (2.3) written in the new variables takes the form

$$H = E_0 + \sum_i \tau_i^z + \sum_{ij} J_{ij}\tau_i^z\tau_j^z + \sum_{n=1}^{\infty}\sum_{i,j,\{k\}} K^{(n)}_{i\{k\}j}\tau_i^z\tau_k^z,\ldots,\tau_{k_n}^z\tau_j^z, \tag{2.4}$$

where each term in the sum appears only once, E_0 is an offset irrelevant to the system's dynamics, and J_{ij} and $K^{(n)}_{i\{k\}j}$ are magnitudes of interactions [1].

Each l-bit precesses around its z axis at a rate set by its interactions with all other $\{\tau_i^z\}$. Because all the $\{\tau_i\}$ are out of phase in a generic state, this precession produces dephasing. Dephasing is a process of lossing coherence caused by perturbations, upon which the system returns to its state before perturbation. Since $\{\tau_i\}$ has no dissipation, dephasing of $\{\tau_i^z\}$ can be reversed by spin-echo procedures, such

FIGURE 2.7: Dynamical behavior of the l-bits. Figure taken from Ref. [1]. Republished with permission of [Ye Cheng Chen], from [Many-body localization and thermalization in quantum statistical mechanics, Rahul Nandkishore and David A Huse, Vol. 6, 2015]; permission conveyed through Copyright Clearance Center, Inc.

as Loschmidt echo (discussed in Chapter 5). For single-particle localized states, there is only one state with a certain phase, so there is no dephasing or dissipation in p-bits. Reversing the dephasing of a particular l-bit is experimentally challenging, because one can only access the p-bits instead of l-bits; however, it is possible through high-fidelity spin-echo measurements for weakly interacting systems [89].

The spreading of entanglement (SE) for single-particle localized systems is absent because there are no interactions between l-bits. In thermalizing systems, if p-bit A interacts with p-bit B, then they are entangled. When B interacts with C, this interactions produces entanglement not just between B and C but also between A and C. Entanglement spreads ballistically in thermalizing systems, which hence obey power-law spreading of entanglement from non-entangled initial condition. However, this ballistic spreading is absent in the FMBL phase. In localized systems, interactions between two l-bits can only produce entanglement between themselves, and all other interactions have no entanglement effect on these two l-bits, because the l-bit Hamiltonian Eq. (2.4) has no dissipation. One can define an effective interaction $J(L)$ between each l-bits, so that this interaction is not only expected to fall off with the distance L between each l-bits, $J \sim J_0 \exp(-L/\xi)$, but also entangles all of them after time t, $J \cdot t \geq 1$, from the non-entangled initial condition. The result is that all the l-bits are entangled within a distance $L \sim \xi \ln J_0 t$ of each other. Therefore the entanglement for a MBL system obeys the logarithmic law of spreading [1, 90–92].

We conclude this chapter by including a list of properties of the thermal phase, the single-particle localized phase, and the many-body localized phase in Table 2.1. Because localization is wave phenomenon, we are able to investigate phase transitions for both single-particle and many-particle systems, typically the SSH

model and the XXZ model, using the spin-echo technique known as the Loschmidt echo. We will discuss the models in Chapter 3 and the Loschmidt echo in Chapter 5.

Thermal phase	**Single-particle localized**	**Many-particle localized**
Memory of initial conditions hidden in global operators at long times	Some memory of local initial conditions preserved in local observables long times	Some memory of local initial conditions preserved in local observables long times
ETH true	ETH false	ETH false
Possible non-zero DC conductivity	Zero DC conductivity	Zero DC conductivity
Continuous local spectrum	Discrete local spectrum	Discrete local spectrum
Entanglement entropy with volume-law	EE with area-law	EE with area-law
Power-law SE from non-entangled initial condition	No spreading of entanglement	Logarithmic SE from non-entangled initial condition
Dephasing and dissipation	No dephasing, no dissipation	Dephasing but no dissipation

TABLE 2.1: A list of properties for the thermal phase, single-particle localized phase, and the MBL phase. Table taken from Ref. [1]. Republished with permission of [Ye Cheng Chen], from [Many-body localization and thermalization in quantum statistical mechanics, Rahul Nandkishore and David A Huse, Annu. Rev. Condens. Matter Phys., Vol. 6, 2015]; permission conveyed through Copyright Clearance Center, Inc.

Chapter 3

Models

In this section, we will introduce the models used for this research, namely the Su-Shrieffer-Heeger (SSH) model and the XXZ model. The SSH model is of a topological system whereas the XXZ is of a spin system. We will discuss several properties of a topological system, such as the dispersion relation, bulk-boundary correspondence, and edge states. For the XXZ model, we will discuss magnetic phases and the Jordan-Wigner transformation. We also include the discussion of exact diagonalization for these models with disorder.

3.1 The Su-Shrieffer-Heeger Model

Polymers are large molecules formed in long chains, and polyacetylene is a simple isomeric chain of a linear conjugated polymer which consists of bonded CH groups. According to the nearly-free electron theory, one might expect the half-filled conduction band of a polyacetylene chain to be metallic. However, the energy of a half-filled band of a one-dimensional system can always be lowered by imposing a periodic lattice distortion of the correct wavelength to open up an energy gap at the Fermi energy, known as the Peierls instability [19]. That is, polyacetylene is an insulator. Using a simple one-dimensional (1D) tight-binding model, where the hopping matrix elements represent alternating off-diagonal tunnelling strengths,

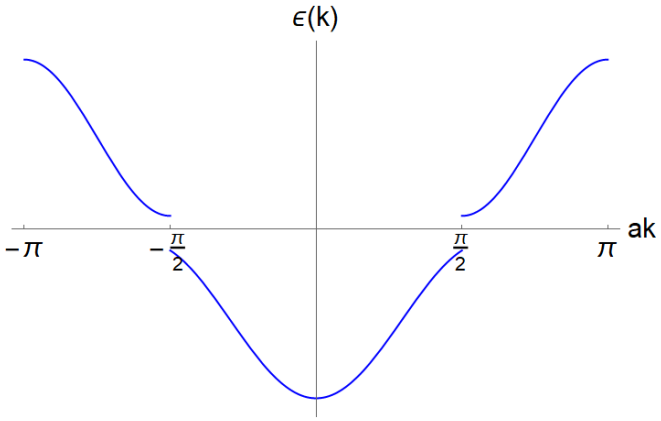

FIGURE 3.1: The lowest Bloch bands of a dimerized one dimensional Polyacetylene lattice. Energy gaps appear in $ka = \pm\pi/2$ as a result of the Peierls instability.

Su, Shrieffer and Heeger were able to explain the unusual electronic conductivity of polyacetylene and the Peierls instability [93]. As shown in Fig. 3.1, the Peierls distortion is inevitably frustrated when the number of lattice sites is odd, and as a consequence the polymer chain must accommodate a topological excitation—topologically protected solitonic defects free to move along the polymer chain. The excitation is said to be topological because the defect cannot be removed by a smooth continuous deformation. Even if the number of sites is even, one can create low energy topological excitations in the system either by doping or by the creation of particle–hole excitations of the system. The Su-Schrieffer-Heeger (SSH) model has served as the standard model of a 1D system characterized by charge fractionalization and topological properties [94, 95]. We will discuss several key features of the model, including the second quantization representation of the Hamiltonian, the dispersion relation, the bulk-boundary correspondence, and most importantly its connection to our research.

3.1.1 The SSH Hamiltonian

The SSH model describes spinless fermions hopping on a one-dimensional lattice with staggered hopping amplitudes. As shown in Fig. 3.2, the chain consist of N unit cells, and each unit cell has two sites: one on sublattice A and another on sublattice B. The lattice structure of the SSH model has only one conduction electron attached to each carbon atom, so each unit cell of the fermionic chain can only have one particle. This situation, called half-filling, can only happen for fermionic systems with zero chemical potential, and all fermions specifying all negative energy eigenstates are singly occupied as the ground state of the Hamiltonian. Such a state is a preferable initiate state of a closed system to investigate localization phenomena.

For a system with N unit cells, there are $L = 2N$ lattice sites and N eigenstates satisfying half-filling. The hopping amplitudes are assumed to be real and nonnegative; $v, w \geq 0$. Due to the absence of interaction and on-site potential, the SSH model can be described by the single-particle Hamiltonian operator,

$$\hat{\mathcal{H}} = v \sum_{n=1}^{N} (|\psi_{n,A}\rangle\langle\psi_{n,B}| + h.c.) + w \sum_{n=1}^{N-1} (|\psi_{n+1,A}\rangle\langle\psi_{n,B}| + h.c.). \tag{3.1}$$

Here $|\psi_{n,A}\rangle$ and $|\psi_{n,B}\rangle$, with $n \in \{1, 2, ..., N\}$, denote the state of the chain where the electron is on unit cell j, in the sublattice site A, and B, respectively; $h.c.$ stands for hermitian conjugate. v is intracell hopping amplitude, and w is the intercell hopping amplitude [5]. Eq. (3.1) is the first quantization representation of the single-particle SSH Hamiltonian.

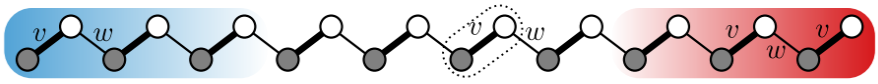

FIGURE 3.2: Geometry of the SSH model. Filled (empty) circles are sites on sublattice $A(B)$, each hosting a single state. Hopping amplitudes are staggered: intracell hopping v (double lines) is different from intercell hopping w (single lines). Figure taken from Ref. [5]. Republished with permission of [Ye Cheng Chen], from [A Short Course on Topological Insulators, János K. Asbóth *et al.*, Vol. 919, 2019]; permission conveyed through Copyright Clearance Center, Inc.

The single-particle operator $\hat{\mathcal{H}}$ is diagonal in the basis $\{|\psi_{n,l}\rangle\}$, where $l = A, B$ is the sublattice index. For $L = 2N$ lattice sites, we can use the indices

$$|\psi_{2j-1}\rangle = |\psi_{n,A}\rangle\,, \;\; |\psi_{2j}\rangle = |\psi_{n,B}\rangle\,.$$

The second quantization representation of Eq. (3.1) acting on $|\psi_j\rangle$ can therefore be expressed as

$$\hat{H} = \sum_{j}^{L} \langle\psi_j|\hat{\mathcal{H}}|\psi_{j+1}\rangle\, c_j^\dagger c_{j+1} + h.c.,$$

where $c_j^\dagger$ and c_j are the fermion creation and annihilation operators on site j. The matrix $\mathcal{H} = \langle\psi_j|\hat{H}|\psi_{j+1}\rangle$ has the following single-particle expression

$$\mathcal{H} = \begin{pmatrix} 0 & v & 0 & 0 & \dots & w \\ v & 0 & w & 0 & \dots & \vdots \\ 0 & w & \ddots & \ddots & \dots & \vdots \\ \vdots & \dots & \ddots & \ddots & w & 0 \\ \vdots & \dots & 0 & w & 0 & v \\ w & \dots & 0 & 0 & v & 0 \end{pmatrix}, \tag{3.2}$$

for periodic boundary conditions (PBC). The matrix $\mathcal{H}$ for the system with open

boundary conditions (OBC) omits the intercell hoppings (w) on the upper-right and lower-left corners in Eq. (3.2).

Let $v = J(1-\delta)$ and $w = J(1+\delta)$, we arrive the second quantization representation of the many-particle Hamiltonian for the SSH model

$$\hat{H} = J\sum_{j=1}^{L}[(1+\delta e^{i\pi j})\hat{c}_j^\dagger \hat{c}_{j+1} + h.c.], \tag{3.3}$$

Here $\delta \in [-1, 1]$ is the dimerization, and J is the hopping amplitude for nearest-neighbor sites and is set to 1 for numerical calculations, but we include J in the formula expressions. For periodic boundary conditions the sum is taken up to site L and $c_{L+1} = c_1$ while the sum is taken up to $L-1$ for open boundary conditions. We will soon discuss the difference between the single-particle and the many-particle Hamiltonians.

3.1.2 The dispersion relation

Similar to any solid state systems, the chain of the SSH model has a bulk and a boundary component. The bulk is the long central part of the chain, and the boundaries are the two ends (edges) of the chain. The bulk chain in the thermodynamic limit $N \to \infty$ is independent of how the edges are defined, and the bulk chain can be closed into a ring by imposing PBC and translational invariance. By including sublattice index A and B, Eq. (3.3) can be written as

$$\hat{H} = J\sum_{j}[(1-\delta)\hat{c}_{j,A}^\dagger \hat{c}_{j,B} + (1+\delta)\hat{c}_{j,B}^\dagger \hat{c}_{j+1,A} + h.c]. \tag{3.4}$$

Using the Fourier transform on the fermionic operators,

$$\hat{c}_{j,A} = \sqrt{\frac{2}{N}} \sum_k e^{i2kj} c_{k,A};\ \hat{c}_{j,B} = \sqrt{\frac{2}{N}} \sum_k e^{i2kj} e^{ik} c_{k,B},$$

we can express the Hamiltonian in the momentum space

$$\begin{aligned}
H =& J \sum_k \Big[(1-\delta) c^\dagger_{k,A} c_{k,B} e^{ik} + (1+\delta) e^{-ik} c_{k,B} e^{i2k} c_{k,A} + h.c \Big] \\
=& J \sum_k \Big[(1-\delta)[e^{ik} c^\dagger_{k,A} c_{k,B} + e^{-ik} c^\dagger_{k,B} c_{k,A}] \\
& + (1+\delta)[e^{ik} c^\dagger_{k,B} c_{k,A} + e^{-ik} c^\dagger_{k,A} c_{k,B}] \Big] \\
=& J \sum_k \Big[2\cos k c^\dagger_{k,A} c_{k,B} + 2i\delta \sin k c^\dagger_{k,A} c_{k,B} + h.c \Big] \\
H =& \sum_k \begin{pmatrix} c^\dagger_{k,A} & c^\dagger_{k,B} \end{pmatrix} \begin{pmatrix} 0 & 2J[\cos k + i\delta \sin k] \\ 2J[\cos k - i\delta \sin k] & 0 \end{pmatrix} \begin{pmatrix} c_{k,A} \\ c_{k,B} \end{pmatrix}.
\end{aligned}$$

Therefore, Eq. (3.3) defines the bulk-Hamiltonian $\mathcal{H}(k)$ in the momentum space k via [11]

$$H = \sum_k \Psi^\dagger_k \mathcal{H}(k) \Psi_k \text{ with } \mathcal{H}(k) = \mathbf{d}_k \cdot \boldsymbol{\sigma}. \tag{3.5}$$

Here $\boldsymbol{\sigma}$ is the vector of Pauli matrices $(\sigma_x, \sigma_y, \sigma_z)$, and after Fourier transform and a convenient rotation, $\Psi^\dagger_k$ takes the following form

$$\Psi^\dagger_k = \sqrt{\frac{2}{L}} \sum_{j=1}^{L/2} e^{i2kj} \begin{pmatrix} 1 & 0 \\ 0 & e^{i2k} \end{pmatrix} \underbrace{\begin{pmatrix} c_{2j-1} \\ c_{2j} \end{pmatrix}}_{=\Psi_j}.$$

From the above derivations, we have $\mathcal{H}(k)$ written as

$$\mathcal{H}(k) = \begin{pmatrix} 0 & 2J[\cos k + i\delta \sin k] \\ 2J[\cos k - i\delta \sin k] & 0 \end{pmatrix}, \tag{3.6}$$

so that

$$\mathbf{d}_k = (-2J\cos(k), 2J\delta \sin(k), 0).$$

The momenta are $k = 2\pi n/L$ with $n = 1, 2, \ldots, L/2$.

The dispersion relation $E(k)$ can be obtained by diagonalizing Eq. (3.6) via $\det(\mathcal{H}(k) - E(k) \cdot \mathbb{1}) = 0$,

$$E(k) = \pm 2J\sqrt{\cos^2 k + \delta^2 \sin^2 k}, \tag{3.7}$$

where $k \in [-\pi/2, \pi/2]$ is defined as the first Brillouin zone. Setting $J = 1$ with $\delta = (w - v)/2$, we briefly illustrate below the notion of bulk-boundary correspondence by varying v and w.

3.1.3 The bulk-boundary correspondence

For the system in the thermodynamic limit we look at three cases qualitatively and diagrammatically using Fig. 3.3. The first case is for $v = w$ and so $\delta = 0$. The dispersion relation $E(k) = \pm 2\cos k$. For $k = -\pi/2$ or $\pi/2$, $E(k) = 0$, so there is no energy gap at the two ends of the first Brillouin zone. The SSH model describes a conducting phase without staggering[1], and there are plane wave eigenstates of

[1] Staggering refers to sign changes under translation by one lattice spacing; in our case, $v \neq w$[19].

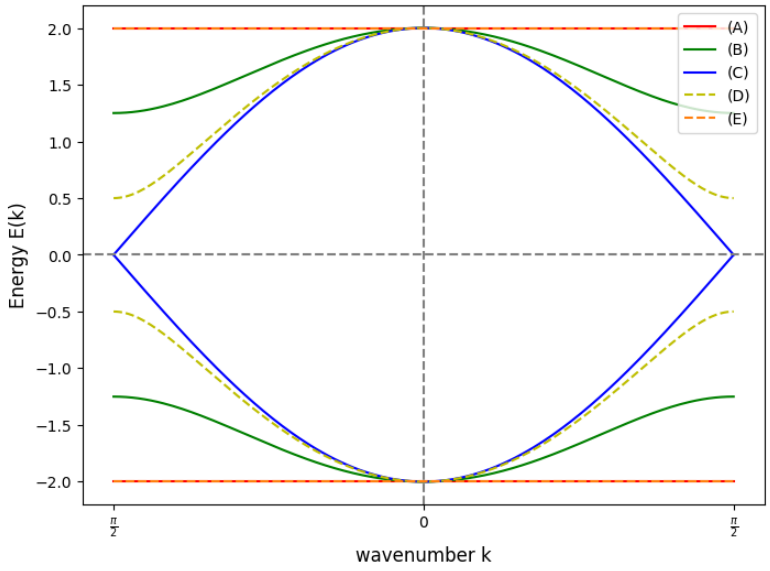

FIGURE 3.3: Dispersion relations of the SSH model in first Brillouin zone for five settings of the hopping amplitudes: (A): $v = 1, w = 0$; (B): $v = 1, w = 0.5$; (C): $v = w = 1$; (D): $v = 0.75, w = 1$; (E): $v = 0, w = 1$. The energy gap closes up in the direction v: $1 \to 0$ as w: $0 \to 1$, or vice versa.

the bulk available with arbitrarily small energy permitting the transportation of electrons within the bulk (see case (C) in Fig. 3.3).

The second case is when $w = 2$ and $v = 0$ so that $\delta = 1$. Then the dispersion relation $E(k) = \pm 2J$ describes an energy gap E_{gap} between the conduction and the valence band for all $k \in [-\pi/2, \pi/2]$,

$$E_{gap} = 4J.$$

The bulk Hamiltonian is said to be fully dimerized, and the system describes a trivial or insulating phase, where conduction is prohibited (see (A) and (E) in Fig. 3.3).

The third case takes place upon varying v and w, where $v > w$ or $v < w$. The

energy gap becomes smaller at the two ends of the Brillouin zone $k = -\pi/2$ and $\pi/2$, and it is $E_{gap} = 4J\delta$ for $\delta > 0$ (see (B) and (D) in Fig. 3.3). Even though the energy gap seems equivalent in the particular cases being considered, there is an intrinsic, topological difference between $v > w$ and $v < w$. The case $v > w$ refers to the trivial phase, whereas the case $v < w$ is known as the topologically non-trivial phase, where there exists eigenstates connecting the valence band to the conduction band at the two ends. These eigenstates which move along the boundary of the bulk are known as edge states, which show up numerically for systems with open boundary conditions. Fig. 3.4 shows the energy eigenvalues of the SSH model for $L = 20$ system sites. The two edge states emerge from $\delta < 0$ ($v < w$) to $\delta > 0$ ($w > v$). For $\delta < 0$, the energy eigenvalues of these two states are non-zero and have opposite signs; this is the trivial phase. For $\delta > 0$, the eigen-energies of the two edge states are slightly above and below zero, known as the zero edge states; this is the topological non-trivial phase.

In short, we have discussed the SSH model and its relevant properties, such as edge states and the notion of bulk-boundary correspondence, where phase transitions can take place in the system from the trivial phase to the topological non-trivial phase.

3.2 The XXZ Model

For an interacting many-body system, the Hamiltonian can be expressed in terms of kinetic energy of electrons, potential energy of electrons, electron-electron interaction, kinetic energy for nuclei and nucleus-nucleus interaction. In such complex systems, the high-energy degrees of freedom can be "integrated out" to reveal an

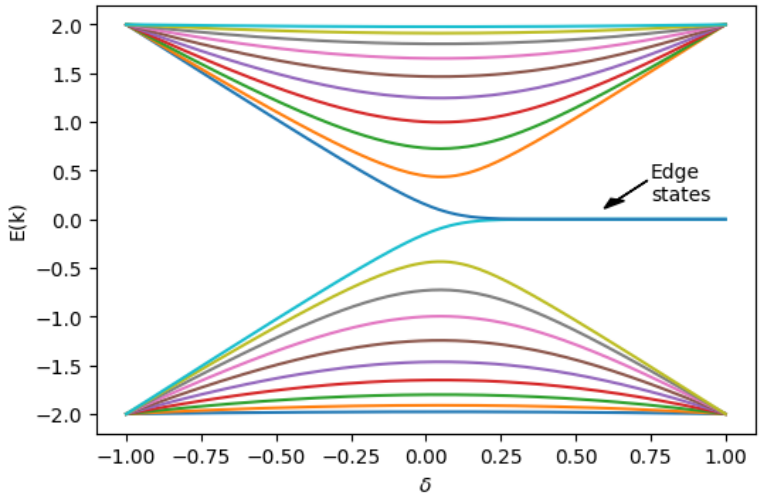

FIGURE 3.4: Energy eigenvalues of the SSH model revealing the two edge states.

effective Hamiltonian, which can describe a certain subset of the electronic degrees of freedom at low-energy. This is the fundamental idea of renormalization, and the Hubbard model was the one introduced by J. Hubbard etc. to study such complex system [96–99]. From the Hubbard model one can derive the Heisenberg model, which describes the spin degrees of freedom in a Mott insulating phase, where the electronic charge degrees of freedom are neglected or “frozen out". The Heisenberg model is a statistical mechanical model for which one can study critical points and phase transitions of magnetic systems [100]. The XXZ model is an interacting Heisenberg model, which consists of a one-dimensional spin-1/2 chain and whose interactions show an anisotropy along a specific direction. The anisotropic coupling constant J induces different ordering in the system, so that three phases can be characterised; namely, an antiferromagnetic one, an entirely critical paramagnetic and a ferromagnetic region. In this section, we will discuss the XXZ Hamiltonian, the Jordan-Wigner transformation, and the three magnetic phases.

3.2.1 The Heisenberg Model

The Heisenberg model describes the nearest-neighbour spin interaction of many-body particles ([19, 100, 101]). The most general Hamiltonian of the Heisenberg model with nearest-neighbour interaction for N lattice sites is given by

$$\hat{H} = -\sum_{j=1}^{N} \left[J_x S_j^x S_{j+1}^x + J_y S_j^y S_{j+1}^y + J_z S_j^z S_{j+1}^z \right]. \tag{3.8}$$

Here J_{ij} is expressed in terms of three spatial components J_x, J_y, J_z. The spin operators $\hat{\mathbf{S}}_j$ live on the lattice sites. Spin components on the same lattice site obey the standard angular momentum commutation relations

$$[S_j^\alpha, S_j^\beta] = i\hbar \sum_\gamma \epsilon_{\alpha\beta\gamma} S_j^\gamma \ (\alpha, \beta, \gamma = x, y, z)$$

and spins on different site commute with each other. The operators $\mathbf{S}_j^2$ have eigenvalues $S(S+1)$ where S is an integer or half-integer. The spin interaction in Eq. (3.8) is called exchange interaction, and J_{ij} is called a coupling/exchange constant.

The values of J_x, J_y, and J_z gives rise to different cases to consider for the general Heisenberg model. If $J_x = J_y = J_z = J > 0$, it is called the isotropic ferromagnetic Heisenberg XXX model, and Bethe was the first to provide analytical solution to the model [102]. If $J_x = J_y = J_z = J < 0$, the model is the isotropic antiferromagnetic XXZ Heisenberg model, and des Cloizeaux and Pearson obtained the elementary excitations in 1962 [103]. If $J_x = J_y = J \neq J_z$, it is known as the XXZ Heisenberg model, analytically solved by Yang and Yang in 1966 [104–106]. The fully anisotropic Heisenberg model is for $J_x \neq J_y \neq J_z$, and it was solved by Baxter in 1972 [107, 108]. These are exactly solvable models, and details of

solutions can be found in many textbooks. We will focus on the spin-1/2 XXZ model on a one dimensional lattice chain.

3.2.2 The XXZ Hamiltonian

The spin-1/2 one-dimensional Heisenberg XXZ model for N lattice sites is given by the following Hamiltonian

$$\hat{H} = -J \sum_{j=1}^{N} \left[S_j^x S_{j+1}^x + S_j^y S_{j+1}^y + \triangle S_j^z S_{j+1}^z \right]. \tag{3.9}$$

Here $S_j^\alpha = \frac{1}{2}\sigma_j^\alpha$ and σ^α are the Pauli matrices obeying canonical $SU(2)$ commutation relations

$$\sigma^x = \begin{pmatrix} 0 & 1 \\ 1 & 0 \end{pmatrix} \quad \sigma^y = \begin{pmatrix} 0 & -i \\ i & 0 \end{pmatrix} \quad \sigma^z = \begin{pmatrix} 1 & 0 \\ 0 & -1 \end{pmatrix}.$$

The parameter J sets the energy scales, and the parameter $\triangle$ denotes the strength of the uniaxial anisotropy along the $\hat{z}$ direction. If we let $J = 1$, the parameter $\triangle$ can distinguish a planar regime ($|\triangle| < 1$) from the axial regime ($|\triangle| > 1$). There is no long-range order for $|\triangle| < 1$, a regime also known as the gapless Luttinger liquid phase. In the axial regime, we have a ferromagnetic phase along the $\hat{z}$ direction for $\triangle > 1$ and an antiferromagnetic phase when $\triangle < -1$. Fig. 3.5 shows the phase diagram consisting of a ferromagnetic (FM), a Luttinger liquid (LL), and an antiferromagnetic (AFM) phase. Therefore, $\triangle = 1$ and $\triangle = -1$ correspond to the ferromagnetic and antiferromagnetic Heisenberg chains, respectively.

There are some symmetries that relates these different phases. In order to evaluate its ground state and low energy excitations, one can transform $\hat{H}$ using a

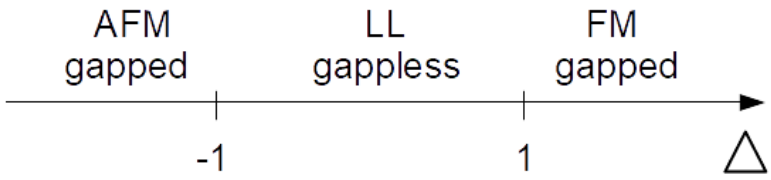

FIGURE 3.5: Schematic phase diagram for the Hamiltonian (3.9). The phase diagram consist of gapped ferromagnetic (FM) and antiferromagnetic (AFM) phases as well as a gapless Luttinger liquid (LL) phase.

unitary operator U =exp$(i\pi \sum_{j=1}^{N} jS_j^z)$

$$U\hat{H}(\triangle)U^{\dagger} = -\hat{H}(-\triangle).$$

This means that the energy spectrum of $\hat{H}(\triangle)$ can be reflected upon changing of sign to obtain the energy spectrum for $\hat{H}(-\triangle)$, but the eigenstates of the Hamiltonian are independent from the sign of J. Moreover, the magnetization along the $\hat{z}$ axis, i.e.

$$S^z = \sum_{j=1}^{N} S_j^z$$

is conserved. In the state $|0\rangle = |\uparrow\uparrow\uparrow \ldots\rangle$ with all spins up, the the configuration reaches its maximum value $S^z = N/2$. A rotation along the $\hat{x}$ axis leaves the Hamiltonian unchanged. Morever,

$$[\hat{H}, S^z] = 0,$$

which can be verified directly using the fundamental commutation relations

$$[S_x, S_y] = i\hbar S_z, \quad [S_y, S_z] = i\hbar S_z, \quad [S_z, S_x] = i\hbar S_z.$$

The ground state of the Heisenberg ferromagnet is different from that of the Heisenberg antiferromagnet. In the case $J\triangle \to \infty$, the ground state can be chosen to be the completely ferromagnetic state $|0\rangle = |\uparrow\uparrow\uparrow \ldots\rangle$. Low-energy excitations can be constructed in terms of magnons. On the other hand, for $J\triangle \to -\infty$, the ground states of the Heisenberg AFM can be expressed as a staggered spin configuration, known as the Neél state, where all neighbouring spins are antiparallel. The low-energy excitations are called spinons. The important feature of the spinons is that the AFM Hamiltonian $\hat{H}$ can now be described by the bipartite lattice, in which there are two sublattices A and B and each site on lattice A has its nearest neighbors on sublattice B. The 1D bipartite lattice looks similar to Fig. 3.2. The Néel state is defined as

$$|\Psi_N\rangle = \prod_{|k|<\pi/2a} d_k^\dagger |0\rangle ,$$

where $|0\rangle$ is the vacuum state and $d_k^\dagger$ is the particle-hole transformation operator. The Néel state is two-fold degenerate, $|N_1\rangle \equiv |\uparrow\downarrow\uparrow\downarrow\uparrow \ldots\rangle$ and $|N_2\rangle \equiv |\downarrow\uparrow\downarrow\uparrow\downarrow \ldots\rangle$. It can be seen as semi-classical representation of the ground state also for $\triangle < 1$, but it is not the true ground state in the gapless phase.

We introduce the spin-flip operators,

$$S_j^+ = S_j^x + iS_j^y, \quad S_j^- = S_j^x - iS_j^y$$

which raises or lowers spin states $|\downarrow\rangle$ and $|\uparrow\rangle$ in the following manner,

$$S^+ |\downarrow\rangle = |\uparrow\rangle , \; S^+ |\uparrow\rangle = 0, \; S^- |\uparrow\rangle = |\downarrow\rangle , \; S^- |\downarrow\rangle = 0.$$

The corresponding commutation relations are

$$[S_j^z, S_j^{\pm}] = \pm S_{j'}^{\pm}\delta_{jj'} \quad [S_j^+, S_{j'}^-] = 2S_j^z\delta_{jj'}.$$

Using the the spin operators, one can express the Hamiltonian in Eq. (3.9),

$$\hat{H} = -J\sum_{j=1}^{N}\left\{\frac{1}{2}\left[S_j^+S_{j+1}^- + S_{j+1}^+S_j^-\right] + \triangle S_j^zS_{j+1}^z\right\}. \tag{3.10}$$

The benefit of Eq. (3.10) is that it allows us to make calculations more conveniently via the Jordan-Wigner transformation, as we will discuss in the following. In 1931, Hans A. Bethe provided the exact solution for this model using the powerful analytical technique known as Bethe Ansatz [102, 109]. The difficulty of the technique is beyond the scope of this thesis, and interested readers can find comprehensive analyses in the article [110].

3.2.3 Jordan-Wigner Transformation

We can map the Hamiltonian (3.10) to a free fermion Hamiltonian using the Jordan-Wigner transformation

$$S_j^+ = (-1)^j\hat{c}_j^\dagger e^{i\pi\phi_j}, \quad S_j^- = (-1)^j\hat{c}_j e^{-i\pi\phi_j}, \quad S_j^z = \hat{c}_j - \frac{1}{2}$$

where $n_j = c_j^\dagger c_j = S_j^+S_j^-$ is the occupation number operator, ϕ_j is the phase factor which contains the sum over all fermion occupations at site to the left of j, $\phi_j = \sum_{l=1}^{j-1} n_l$, and $c_j(c_j^\dagger)$ are annihilation (creation) operators of spinless fermions

at site j. The operator $e^{i\phi_j}$ is known as a string operator. The JWT really means

$$\text{spin} = \text{fermion} \times \text{ string}.$$

This transformation solves a major problem in the Hamiltonian (3.10), where spins on different sites commute whereas fermion operators anticommute, i.e., $S_i^+ S_j^+ = S_j^+ S_i^+$, but $c_i^\dagger c_j^\dagger = -c_j^\dagger c_i^\dagger$. The string operator $e^{i\phi_j}$ anticommutes with all fermions at all sites l to the left of j, i.e., $l < j$: $\{e^{i\phi_j}, c_l^\dagger\} = 0$, while commuting with fermions at all sites to the right $l \geq j$: $[e^{i\phi_j}, c_l^\dagger] = 0 \quad (l \geq j)$. Using the JWT, the spin operators for sites $j < k$ commutes in the following way,

$$[S_j^\pm, S_k^\pm] = [\hat{c}_j^\dagger e^{i\phi_j}, \hat{c}_k^\dagger e^{i\phi_k}] = e^{i\phi_j}[\hat{c}_j^\dagger, \hat{c}_k^\dagger \hat{c}^{i\phi_k}].$$

Since $c_j^\dagger$ anticommutes with both $f_k^\dagger$ and $e^{i\phi_k}$, it commutes with their product $f_k^\dagger e^{i\phi_k}$. Hence, the correct commutation relation is

$$[S_j^\pm, S_k^\pm] \propto [\hat{c}_j^\dagger, \hat{c}_k^\dagger e^{i\phi}] = 0.$$

Using the JWT, we can express Eq. (3.10) in the following fermionic Hamiltonian

$$\hat{H}_{JWT} = -\left[\sum_{j=1}^{N} \frac{J}{2}(\hat{c}_j^\dagger \hat{c}_{j+1} + \hat{c}_{j+1}^\dagger \hat{c}_j) + J\triangle(\hat{c}_j^\dagger \hat{c}_j c_{j+1}^\dagger \hat{c}_{j+1} - \hat{c}_j^\dagger \hat{c}_j + \frac{1}{4})\right]$$

$$\hat{H}_{JWT} = -\frac{J}{2}\sum_{j=1}^{N}(\hat{c}_j^\dagger \hat{c}_{j+1} + \hat{c}_{j+1}^\dagger \hat{c}_j) + J\triangle\sum_{j=1}^{N}\hat{n}_j - J\triangle\sum_{j=1}^{N}\hat{n}_j\hat{n}_{j+1} \tag{3.11}$$

Here we omit the term $\sum_j^N 1/4 = N/4$ because it doesn't change the energy spectrum [111]. Eq. (3.11) allows us investigate quantum behaviours of spin particles.

3.2.4 The XXZ Model with Fourier Transform

We can perform a Fourier transform of the Hamiltonian into momentum space. It is convenient to impose periodic boundary conditions: $S_{j+N} = S_j$ and $c_{j+N} = c_j$. We can define a Fourier transform via the following

$$\hat{c}_j = \frac{1}{\sqrt{N}} \sum_k^{2\pi} \hat{s}_k e^{ikR_j}, \;\; \hat{s}_k = \frac{1}{\sqrt{N}} \sum_j^N \hat{c}_j e^{-ikR_j}, \;\; [\hat{s}_k, \hat{s}_{k'}^\dagger] = \delta_{kk'},$$

where $k = 2\pi m/N, \;\; m = 0, \ldots, N-1$ is the wave vector, and $\hat{s}_k^\dagger$ creates a spin excitation in momentum space. Hence we have the following transformations

$$J\triangle \sum_{j=1}^N \hat{n}_j = J\triangle \sum_{j=1}^N \hat{c}_j^\dagger \hat{c}_j = J\triangle \sum_k^N \hat{s}_k^\dagger \hat{s}_k$$

$$\begin{aligned} -\frac{J}{2} \sum_{j=1}^N (\hat{c}_{j+1}^\dagger \hat{c}_j + h.c.) &= -\frac{J}{2N} \sum_k^N (e^{-ika} + e^{ika}) \hat{s}_k^\dagger \hat{s}_{k'} \sum_j e^{-i(k-k')R_j} \\ &= -J \sum_k \cos(ka) \hat{s}_k^\dagger \hat{s}_k. \end{aligned}$$

Here $\sum_j e^{-i(k-k')R_j} = N\delta_{kk'}$, and a denotes the lattice spacing. The anisotropic XXZ Hamiltonian via the Fourier transform can be written as

$$\hat{H} = \sum_k \epsilon_k \hat{s}_k^\dagger \hat{s}_k - J\triangle \sum_j \hat{n}_j \hat{n}_{j+1}, \tag{3.12}$$

where $\epsilon_k = (J\triangle - J\cos ka)$ is known as the magnon excitation energy. The 1D ferromagnetic and 1D antiferromagnetic phases can been described by this transformation. In the ferromagnet, the fermionic spin excitations are magnons which have spin $S = 1$. In the antiferromagnetic, on the other hand, the fermonic spin excitations are spinons which have spin $S = 1/2$. We will look at two cases in the following, namely the Heisenberg ferromagnet, the XX model and the Heisenberg antiferromagnet.

(I) In the case of the 1D Heisenberg ferromagnet, $J\triangle = J$, which implies that $\triangle = 1$. The energy spectrum becomes

$$\epsilon_k = 2J\sin^2(ka/2),$$

which is positive for $J > 0$. This means that spin excitations are absent in the ground state, so the ground state can be written as

$$|0\rangle = |\downarrow\downarrow\downarrow\ldots\rangle,$$

which corresponds to a state with spontaneous magnetization $M = -N_s/2$. N_s means the number of spin excitations. The idea of spontaneous magnetization is that when a system is subject to external magnetic field h, M takes positive value. By decreasing h to zero, M will not decrease to zero but instead have a certain value above zero. If we add a magnon at $k = 0$, since $\epsilon_{k=0} = 0$, this action of adding a magnon rotates the magnetization infinitesimally upwards but with no energy. The $k = 0$ magnon is a zero-energy excitation, known as the *Goldstone* mode, see Fig. 3.6.

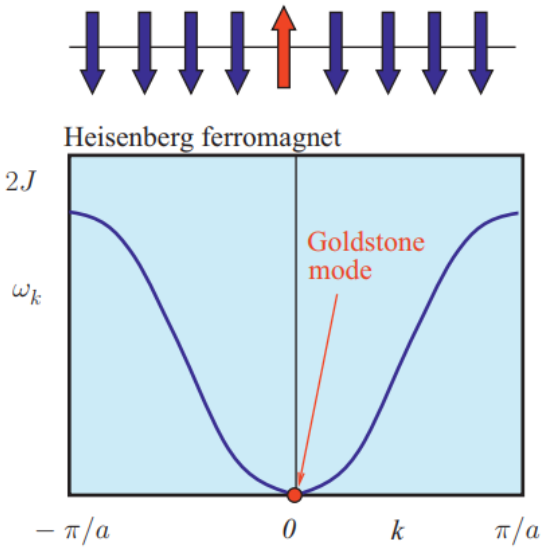

FIGURE 3.6: Excitation spectrum of the one-dimensional Heisenberg ferromagnet. Figure reproduced from [6] as [Introduction to many-body physics, Piers Coleman, Cambridge University Press, 2015]. Reproduced with permission of The Licensor through PLSclear.

(II) In the case of the XX model for $\triangle = 0$, the energy spectrum becomes

$$\epsilon_k = -J \cos ka.$$

As shown in Fig. 3.7, the energy spectrum has a negative part, and all the negative energy states are occupied in the region for $|k| < \pi/2a$. To create an excitation on the occupied state, one can add a magnon at wave vectors $|k| > \pi/2a$, and annihilate a magnon to form a hole at wavevectors $|k| < \pi/2a$ [6]. For free fermions the particle-hole transformation operator which exchanges the role of creation and annihilation is defined as

$$\hat{d}_k^\dagger = (-1)^k \hat{s}_k.$$

The $(-1)^k$ factor takes the value -1 on one sublattice and $+1$ on the other. Because

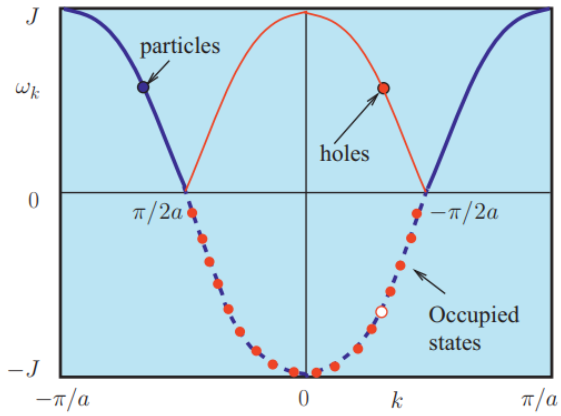

FIGURE 3.7: Excitation spectrum of the one-dimensional XX model. Figure reproduced from [6] as [Introduction to many-body physics, Piers Coleman, Cambridge University Press, 2015]. Reproduced with permission of The Licensor through PLSclear.

of the particle-hole symmetry $\hat{s}_k^\dagger \hat{s}_k = 1 - \hat{s}_k^\dagger \hat{s}_k$, the fermionic excitation states are exchanged, and the Hamiltonian (3.12) for the XX model can be written as,

$$\hat{H}_{XX} = \sum_k J|\cos ka|(\hat{d}_k^\dagger \hat{d}_k - \frac{1}{2}),$$

where the dispersion relation takes the form $\epsilon_k = J|\cos ka|$ [6], see the schematic diagram in Fig. 3.7. In the region for $|k| > \pi/2a$, there are actual particles. For $|k| < \pi/2a$, the magnon states are occupied for the negative energy spectrum, but the corresponding holes are "reflected" for the positive energy spectrum. The energy to form a hole is $-\epsilon_k$. The physically observable excitations are actually the holes rather than the occupied states. Fig. 3.8 shows the experimental evidence of the antiferromagnet in the high-T_c coumpound $LaCuO_4$.

(III) The Heisenberg antiferromagnet refers to $J\triangle \to -\infty$, or $\triangle \to -\infty$ with J fixed. For a system of N sites in the AFM, the situation where there are $N/2$ holes and $N/2$ particles is known as half-filling. Mapping backward from free fermions to

spin operators, holes denote downward spins $\downarrow$ and particles upward spins $\uparrow$. Due to the fact that spins are represented by JTW spin-1/2 operators, the energy levels are split into two degenerate configurations, see Fig. 3.7. The ground state in the AFM are the Néel states occupying the Fermi sea for $|k| < k_F$, and the energy spectrum can be governed by an operation which adds or removes particles from the Fermi sea. A threshold momentum is associated with this operation. When we perform a particle-hole transformation, it leaves the threshold momentum unchanged, so this fermionic excitation is interpreted as a pair of spinons with opposite spin orientations $\uparrow$ and $\downarrow$ [112]. These states which fill up the first Brillouin zone for $k \in [-\pi/a, \pi/a]$ are collectively known as spinons, which describe the spin-wave excitations of the antiferromagnet. To create one of the spinons in the Néel state, one needs to perform a global rotation of all spins, but the energy costs of this interaction only lies at the boundary and does not depend on the number of flipped spins; hence spinons are collective excitations. In contrast to the ferromagnet, the AFM spin-wave dispersion displays a linear spectrum in the limit $k \to 0$. As shown in Fig. 3.8, the integrity of the linear dispersion is maintained.

3.3 Disordered Matrices

To study dynamical phase transitions for disordered systems, we need to evaluate the mean value of the Loschmidt echo averaged from many calculations with different disordered configurations, the so-called disorder-averaged Loschmidt echo. Each configuration corresponds to a set of eigenvalues and eigenvectors obtained by exact diagonalization for a disordered system. To realize a disordered system, we first define the total on-site disorder potential according to Eq. (2.1) in this

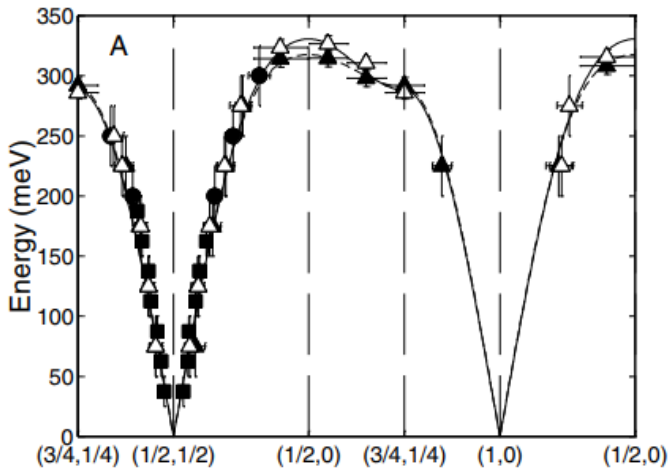

FIGURE 3.8: Spin-wave dispersion of the high-T_c compound $LaCuO_4$ - an experimental evidence for the spin-1/2 antiferromagnet. Figure taken from Ref. [7]. Reprinted with permission from [7] as follows: [R. Coldea *et al.*, Spin waves and electronic interactions in La_2CuO_4, Phys. Rev. Lett., Vol. 86, 5377-5380, 2001]. Copyright (2019) by the American Physical Society.

way,

$$\sum_{j=1}^{L} \mu_j \hat{c}_j \hat{c}_j = \sum_{j=1}^{L} \mu_j \hat{n}_j, \tag{3.13}$$

where $\mu_j \in [-W, W]$ is the box disorder potential, $\hat{n}_j = \hat{c}_j^\dagger \hat{c}_j$ is the occupation number operator on site j, and the sum is over the number of lattice sites $L = 2N$. Each value of μ_j for a given j is randomly generated and independently distinguished from any other values μ_{j+1} for $j + 1$.

The SSH Hamiltonian with disorder potential then takes the form

$$\hat{H}_{SSH} = J \sum_{j=1}^{L} [(1 + \delta e^{i\pi j}) \hat{c}_j^\dagger \hat{c}_{j+1} + h.c.] + \sum_{j=1}^{L} \mu_j \hat{n}_j. \tag{3.14}$$

The the nearest-neighbor interaction for free fermions can be derived from the fermionic interacting XXZ model

$$
\begin{aligned}
V &= \triangle \sum_{j}^{L} S_j^z S_{j+1}^z \\
&= \triangle \sum_{j}^{L} (\hat{c}_j^\dagger \hat{c}_j \hat{c}_{j+1}^\dagger \hat{c}_{j+1} - \hat{c}_j^\dagger \hat{c}_j + \frac{1}{4}) \\
&= \triangle \sum_{j=1}^{L} \left(\hat{n}_j \hat{n}_{j+1} - \frac{1}{4} \right),
\end{aligned}
$$

where $-\sum \hat{c}_j^\dagger \hat{c}_j + 1/4 = -L/4$ and $\triangle L/4$ enters the many-particle Hamiltonian for numerical calculation. The disordered SSH Hamiltonian with nearest-neighbour interaction can then be expressed as

$$
\hat{H}_{SSH_\triangle} = J \sum_{j=1}^{L} [(1+\delta e^{i\pi j}) \hat{c}_j^\dagger \hat{c}_{j+1} + h.c.] + \sum_{j=1}^{L} \mu_j \hat{c}_j^\dagger \hat{c}_j + \triangle \sum_{j=1}^{L} \left(\hat{n}_j \hat{n}_{j+1} - \frac{1}{4} \right). \quad (3.15)
$$

Neglecting the nearest-neighbour interactions, the free fermionic XXZ model (3.11) becomes the non-interacting XX model. The disordered XX model with has the form

$$
\hat{H}_{XX} = \frac{J}{2} \sum_{j=1}^{L} (\hat{c}_j^\dagger \hat{c}_{j+1} + \hat{c}_{j+1}^\dagger \hat{c}_j) + \sum_{j=1}^{L} \mu_j \hat{n}_j. \quad (3.16)
$$

The full XXZ model with disorder potential then has the following form

$$
\hat{H}_{XXZ} = \frac{J}{2} \sum_{j=1}^{L} (\hat{c}_j^\dagger \hat{c}_{j+1} + \hat{c}_{j+1}^\dagger \hat{c}_j) + \sum_{j=1}^{L} \mu_j \hat{c}_j^\dagger \hat{c}_j + \triangle \sum_{j=1}^{L} \left(\hat{n}_j \hat{n}_{j+1} - \frac{1}{4} \right). \quad (3.17)
$$

Here we reverse the signs of J and $\triangle$. A rotation around the z axis of every-other spin followed by the transformation $\triangle \to -\triangle$ maps the $J > 0$ ferromagnetic case into the $J < 0$ antiferromagnet and vice versa: $(J, -\triangle) = (-J, +\triangle)$. Hence

the AFM phase after the rotation corresponds to $\triangle = 1$ instead of $\triangle = -1$, and we are interested in quenching from the Néel state either into the Luttinger-liquid phase ($\triangle = 0$) or across various interaction strengths $\triangle$ in the AFM phase.

While these equations take forms of many-particle Hamiltonians, many-particle problems can be reduced to single-particle problems by neglecting interactions among particles. For a single-particle problem, a single-particle state is represented by a single particle occupying a latice site in real space, but a many-particle state is usually a linear superposition of an orthogonal set of product states in eigenbasis of the Hilbert space. The matrix structure of the single-particle Hamiltonian (SPH) is different from the that of the many-particle Hamiltonian (MPH), and the matrix element of the disordered matrix Eq. (3.13) varies from SPH to MPH.

The particular way we used to diagonalize both the single-particle and many-particle Hamiltonians is called the *exact diagonalization technique*, a computational technique that constructs the many-particle Hamiltonians by exploiting symmetries and iterations [113]. A standard Hubbard or Heisenberg model has four states for single site, so the full Hilbert space has dimension 4^L with L being system sites. Without symmetrization it is practically impossible to go beyond $L = 16$ system sites even on the biggest supercomputers. For our fermionic spinless systems, each site is either empty or occupied, so the dimension of the Hilbert space is reduced to 2^L. An occupied site can be represented using the number "1" and an empty site with "0". For a system with sites $L = 4$, a single-particle state with one particle at site 1 but empty everywhere else can be expressed as $|1000\rangle$. If the same system satisfies the half-filling condition, then a many-particle state can have the form $|1010\rangle$ for two particles at site 1 and 3 at the same time. Here we demonstrate the difference using the non-interacting disordered SSH Hamiltonian (3.14) as an

example, where the Hamiltonian matrix is $\mathcal{H} = \langle\psi_j|\hat{H}|\psi_{j+1}\rangle$ and $J = 1$.

For the SPH with system sites $L = 4$, the single-particle states are $|1000\rangle$, $|0100\rangle$, $|0010\rangle$ and $|0001\rangle$. We perform creation and annihilation operators $\hat{c}_j^\dagger \hat{c}_{j+1}$ on all these states, but we use $|0100\rangle$ for demonstration below.

$$
\begin{array}{ll}
\hat{c}_1^\dagger \hat{c}_2 \,|0100\rangle \Rightarrow |1000\rangle, & \hat{c}_1 \hat{c}_2^\dagger \,|0100\rangle \Rightarrow 0; \\
\hat{c}_1^\dagger \hat{c}_3 \,|0100\rangle \Rightarrow 0, & \hat{c}_1 \hat{c}_3^\dagger \,|0100\rangle \Rightarrow 0; \\
\hat{c}_1^\dagger \hat{c}_4 \,|0100\rangle \Rightarrow 0, & \hat{c}_1 \hat{c}_4^\dagger \,|0100\rangle \Rightarrow 0; \\
\hat{c}_2^\dagger \hat{c}_3 \,|0100\rangle \Rightarrow 0, & \hat{c}_2 \hat{c}_3^\dagger \,|0100\rangle \Rightarrow |0010\rangle\,; \\
\hat{c}_2^\dagger \hat{c}_4 \,|0100\rangle \Rightarrow 0. & \hat{c}_2 \hat{c}_4^\dagger \,|0100\rangle \Rightarrow 0; \\
\hat{c}_3^\dagger \hat{c}_4 \,|0100\rangle \Rightarrow 0, & \hat{c}_3 \hat{c}_4^\dagger \,|0100\rangle \Rightarrow 0.
\end{array}
$$

That is, $\langle 1000|\hat{H}|0100\rangle = 1 - \delta$ for $j = 1$, and $\langle 0010|\hat{H}|0100\rangle = 1 + \delta$ for $j = 2$. The occupation number operator acting on a single-particle state $\hat{n}_j \,|\psi_j\rangle$ gives back the state $|\psi_j\rangle$ at site j with a random number $\mu_j \in [-W, W]$. Having performed the operations on all the states, we have the following form for the matrix $\mathcal{H}$ of the single-particle disordered SSH model with open boundary conditions

$$
\mathcal{H}_{SSH}^{sp} = \langle\psi_j|\hat{H}|\psi_{j+1}\rangle = \begin{pmatrix}
\mu_1 & 1-\delta & 0 & 0 \\
1-\delta & \mu_2 & 1+\delta & 0 \\
0 & 1+\delta & \mu_3 & 1-\delta \\
0 & 0 & 1-\delta & \mu_4
\end{pmatrix}.
$$

In the many-particle problem, on the other hand, the many-particle states for fermionic systems with half-filling requires that each particle state consists of two particles from different sites. For a MPH with system sites $L = 4$, the number of distinct many-particle states is the permutation that 2 particles can be selected from 4 sites: $4!/(2! \cdot 2!) = 6$. The size of the Hamiltonian matrix is the square of 6:

6×6. To construct the matrix element of the many-particle Hamiltonian, we perform the creation annihilation operations on the many-particle eigenstates: $|1100\rangle$, $|1010\rangle$, $|1001\rangle$, $|0110\rangle$, $|0101\rangle$ and $|0011\rangle$. We demonstrate the many-particle operations with the state $|1010\rangle$ as an example

$$
\begin{array}{ll}
\hat{c}_1^\dagger \hat{c}_2 \,|1010\rangle \Rightarrow 0, & \hat{c}_1 \hat{c}_2^\dagger \,|1010\rangle \Rightarrow |0110\rangle\,; \\
\hat{c}_1^\dagger \hat{c}_3 \,|1010\rangle \Rightarrow 0, & \hat{c}_1 \hat{c}_3^\dagger \,|1010\rangle \Rightarrow 0; \\
\hat{c}_1^\dagger \hat{c}_4 \,|1010\rangle \Rightarrow 0, & \hat{c}_1 \hat{c}_4^\dagger \,|1010\rangle \Rightarrow 0; \\
\hat{c}_2^\dagger \hat{c}_3 \,|1010\rangle \Rightarrow |1100\rangle, & \hat{c}_2 \hat{c}_3^\dagger \,|1010\rangle \Rightarrow 0; \\
\hat{c}_2^\dagger \hat{c}_4 \,|1010\rangle \Rightarrow 0. & \hat{c}_2 \hat{c}_4^\dagger \,|1010\rangle \Rightarrow 0; \\
\hat{c}_3^\dagger \hat{c}_4 \,|1010\rangle \Rightarrow 0, & \hat{c}_3 \hat{c}_4^\dagger \,|1010\rangle \Rightarrow |1001\rangle\,.
\end{array}
$$

The disorder potential for each many-particle state takes the accumulative disordered effect from particles on corresponding sites. The many-particle state $|1100\rangle$, for instance, has particles at sites 1 and 2. The disorder potential for $|1100\rangle$ is the sum of μ_1 and μ_2. In short, the MPH, $\hat{H}_{SSH}^{mp}$, with disorder has the following form

$$
\begin{array}{c}
 \\
\langle 1100| \\
\langle 1010| \\
\langle 1001| \\
\langle 0110| \\
\langle 0101| \\
\langle 0011|
\end{array}
\begin{array}{c}
\begin{array}{cccccc}
|1100\rangle & |1010\rangle & |1001\rangle & |0110\rangle & |0101\rangle & |0011\rangle
\end{array} \\
\left(\begin{array}{cccccc}
\mu_1+\mu_2 & 1+\delta & 0 & 0 & 0 & 0 \\
1+\delta & \mu_1+\mu_3 & 1-\delta & 1-\delta & 0 & 0 \\
0 & 1-\delta & \mu_1+\mu_4 & 0 & 1-\delta & 0 \\
0 & 1-\delta & 0 & \mu_2+\mu_3 & 1-\delta & 0 \\
0 & 0 & 1-\delta & 1-\delta & \mu_2+\mu_4 & 1+\delta \\
0 & 0 & 0 & 0 & 1+\delta & \mu_3+\mu_4
\end{array}\right)
\end{array}.
$$

Once the Hamiltonian matrix is constructed, solving for the eigenvalues and

eigenvectors immediately follows. One may notice that the dimension of a single-particle Hamiltonian is much smaller than the dimension of a many-particle Hamiltonian. In numerical calculations, the difference becomes significant in evaluating many-particle systems for large system size. The dimension of a SPH can be as large as allowed by large portion of the computer memory, such as $L = 3200$, but it is impossible to evaluate a MPH with this size. Details will be discussed in Chapter 6. We have demonstrated the exact diagonalization technique for the non-interacting SSH model (3.14), and the same can be said for the XX model. For interacting models, (3.15) and (3.17), Hamiltonians with nearest-neighbour interactions can be constructed in similar way using exact diagonalization, see Ref. [113] and Appendix (C).

3.4 Summary

In this chapter, we have discussed the models of our interest: the SSH model and the XXZ model. The SSH model is a non-interacting model, whereas the XXZ model has the nearest-neighbour interaction in the many-particle ferminonic Hamiltonian. There are many studies about the dynamical phase transitions (DPTs) about these models [114, 115]. We are interested in understanding DPTs for both models, where disorder and nearest-neighbour interaction are taken into consideration.

We also discussed the exact diagonalization technique used in disordered systems. For non-interacting systems, the problem reduces to a single-particle problem, and the Hamiltonian matrix without disorder can take the bipartite form, see Section (3.3). More importantly, evaluating the Loschmidt echo for single-particle

Hamiltonians with large system size becomes easily accessible. The inclusion of the on-site disorder potential turns the bidiagonal matrix into the tridiagonal matrix, in which $\sum_j \mu_j$ spams the diagonal elements of the matrix. The disordered systems whose Hamiltonian matrices can take tridiagonal forms are $\hat{H}_{SSH}$ (3.14) and $\hat{H}_{XX}$ (3.16), and evaluating the LE for these systems is called the single-particle Hamiltonian approach (SPHA). For critical disordered systems with nearest-neighbour interactions, $\hat{H}_{SSH_{\triangle}}$ (3.15) and $\hat{H}_{XXZ}$ (3.17), evaluating the LE for many-particle Hamiltonians in small system size is called the many-particle Hamiltonian approach (MPHA). The two approaches refer to two Loschmidt echo formulae, and we will discuss them in Chapter 5.

Chapter 4

Dynamical Phase Transition

Phase transition is the change of state of a substance from a solid, liquid, or gas state to a different state. Phase transitions which appear in solid-to-liquid or liquid-to-gas phases are known as the equilibrium phase transition for systems in thermal equilibrium with their environment. During an equilibrium phase transition (EPT) of a given system, certain properties of the system change, often discontinuously, as a result of the change of some external condition, such as temperature or pressure. The description and understanding of EPTs remains one of the major studies of thermodynamics and statistical mechanics, which are concerned with the average properties of a quantum statistical system. In 1952, Yang and Lee provided fundamental explanation of phase transitions using theories of statistical mechanics for the first time. They showed that phase transitions are discontinuities or non-analyticities of the free energy density function upon varying the temperature, and these discontinuities are commonly called *Yang-Lee zeros*. Michael Fisher later extended the real temperature parameter to the plane of complex temperature through the study of the distribution of the zeros of the canonical partition function, where the zeros are called *Fisher zeros*. Fisher's work established the foundation to the notion of dynamical phase transitions (DPT). In this section, we will briefly discuss the concepts of Yang-Lee zeros, Fisher zeros and dynamical phase transitions.

4.1 Yang-Lee Zeros

From a mathematical definition, a *zero* of a function f is a point z_0 where f is continuous in some neighborhood of z_0 and $f(z_0) = 0$. A point z_i where f is not continuous or differentiable in some neighborhood of z_i is known as a point of discontinuity or non-analyticity. In thermal statistical physics, the first-order phase transitions correspond to points of discontinuity z_i where the thermodynamic free energy function is non-analytic. Yang and Lee showed the existence of this function by means of grand canonical statistical mechanics [116].

Consider a monatomic gas with interactions in given a volume V and a fixed temperature T. Each particle is given a finite impenetrable core, so that interaction strength among particles is a finite non-zero value. In the grand canonical ensemble at chemical potential μ and temperature $T = 1/k_B\beta$, the fugacity of system z is defined as

$$z = e^{(\mu/k_B T)}.$$

The grand canonical partition function of the system is given by

$$\mathcal{Z}_V(T, z) = \sum_{n=0}^{N} Z_n(T) z^n,$$

where $Z_n(T)$ is the canonical partition function for n particles, and N is the maximum number of particles that can be put in the volume V. $Z_V(T, z)$ is therefore a polynomial of N-th order in the fugacity z.

According to the fundamental theorem of algebra, there are N roots $z_i = z_i(T)$ so that $Z_V(T, z_i) = 0$ with $i = 1, \ldots, N$. The fact that individual particle has solid

volume allows one to express $Z_V(T,z)$ in an infinite convergent product,

$$Z_V(T,z) = e^{g(z)} \prod_{i=1}^{N} \left[1 - \frac{z}{z_i}\right],$$

where $e^{g(z)}$ is some function to be ignored for now. The thermodynamic potential for $Z_V(T,z)$ is defined as $\Omega = -k_B T \ln Z_V(T,z) = -PV$. In the thermodynamic limit $V \to \infty$, the finite-sized pressure $P(z)$ and the local density function $\rho(z)$ can be expressed as

$$\begin{aligned} P(z) =& k_B T \lim_{V\to\infty} \left(\frac{1}{V}\sum_{i=1}^{N} \ln\left[1 - \frac{z}{z_i}\right]\right), \\ \rho(z) =& \lim_{V\to\infty} \left(\frac{\partial}{\partial \ln z}\right)\left(\frac{1}{V}\sum_{i=1}^{N} \ln\left[1 - \frac{z}{z_i}\right]\right). \end{aligned}$$

According to Weierstrass theorem, because the coefficients of all the powers of z in the expression of $Z_V(T,z)$ are real and positive, none of these roots z_i can be real and positive—they appear in complex-conjugate pairs in the complex-fugacity plane [117]. That is, these roots z_i can move about a region R in the complex plane, but there is a segment of the positive real axis where the roots z_i are not defined. Yang and Lee showed that as $V \to \infty$ both $P(z)$ and $\rho(z)$ are analytic functions with respect to z in the region R. $P(z)$ is a continuous, monotonically increasing function of positive values of z and independent of the shape of V. However, as $V \to \infty$, when the roots z_i approach the segment of the positive real axis where the they are not defined, $\rho(z)$ has discontinuities at these roots z_i. Hence $\rho(z)$ is discontinuous for all z_i approaching the positive real axis in the region R, and these z_i are the zeros of $Z_V(T,z_i)$.

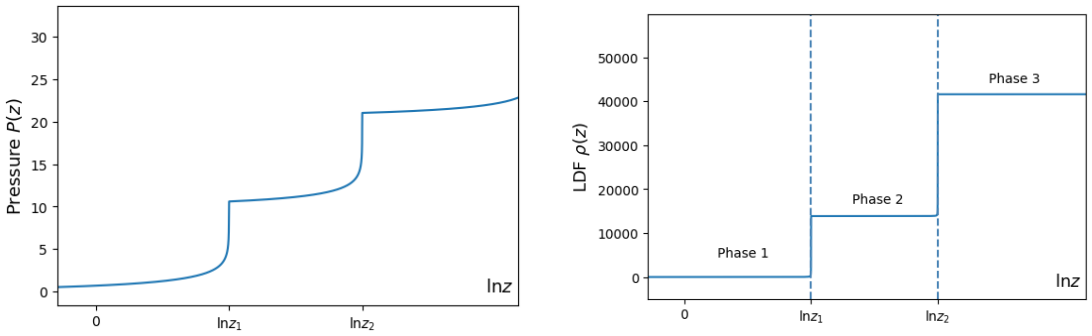

(A) (B)

FIGURE 4.1: Schematic diagram for the analytical behavior at a given temperature T of the pressure function $P(z)$ in (A) and the local density function (LDF) $\rho(z)$ in (B) for a system that undergoes two phase transitions. The transition points z_1 and z_2 are zeros which approaches the positive real z axis.

4.2 Fisher Zeros

In a review article written in 1967, Michael Fisher suggested the analysis of the phase trasitions in the frame of the canonical ensemble, through the study of the distribution of the zeros of the canonical partition function in the plane of the complex temperature [118]. In view of the equivalence of the various statistical ensembles in the thermodynamic limit, one should be able to equally characterize a phase transition in any of these ensembles [119]. As in the grand-canonical ensemble, the Fisher zeros lie in the complex-temperature region free of the positive real temperature semi-axis for a finite system. As these zeros approach the positive semi-axis in the thermodynamic limit, a limiting line of zeros will cut the semi-axis at a point known as the critical point of temperature T_c. Fisher illustrated this idea on the two-dimensional square lattice Ising model, with isotropic nearest-neighbor interactions, in the absence of an external magnetic field [118].

The Fisher zeros are much more sensitive than the Yang-Lee zeros to the details of the interactions (type of lattice, dimensionality), and also to boundary conditions. Following closely that of the Yang–Lee zeros studies, the concept of Fisher zeros was rapidly set-up in its general frame, including the relevance of the thermodynamic limit, the location of the critical point, [120, 121], and the characterization of the transition [122–126]. The underlying assumption of these abstract studies on the characteristics of the transition is that in the thermodynamic limit the Fisher zeros fall on smooth, complex-conjugate curves, at least in some vicinity of the critical point. While these complex zeros have been originally introduced as a purely theoretical concept, it is worthwhile to emphasize that recently it became possible to measure them experimentally [127, 128]. Fig. 4.2 shows the Fisher zeros of noninteracting trapped bosons in a complex plane of inverse temperature.

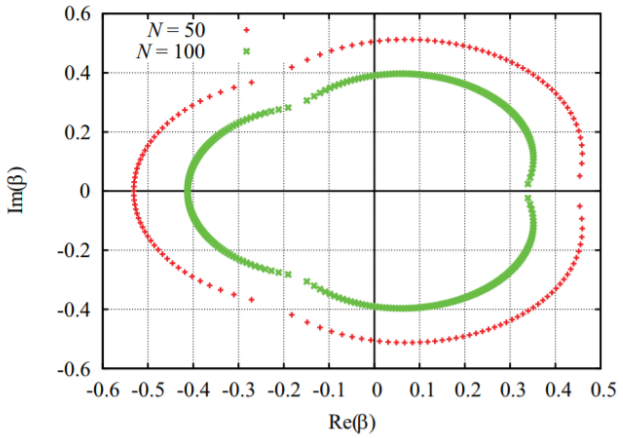

FIGURE 4.2: The Fisher zeros for systems of 50 or 100 noninteracting trapped bosons with a continuous density of states. $\beta = 1/k_B T$ is the inverse temperature. Figure taken from Ref. [8]. Republished with permission of [Ye Cheng Chen], from [Fisher zeros of a unitary bose gas, Wytse van Dijk *et al.*, Canadian Journal of Physics, Vol. 93, 2014]; permission conveyed through Copyright Clearance Center, Inc..

4.3 Dynamical Phase Transition

Dynamical phase transition (DPT) means the phase transitions within a system as a function of time. The notion of DPT rises from a recent idea to study Fisher zeros and thus critical points for localizing systems evolving dynamically in time under a small perturbation due to disorder (see Chapter 1). While the parameter time t describes the time evolution of a localized system, a thermalizing system can be parametrized by temperature T. For a closed system, the canonical partition function of a system at thermal equilibrium is defined as

$$Z(\beta) = \text{Tr } e^{-\beta H},$$

where $Z(\beta)$ provides indirect description to temperature-driven (β) phase transitions via the thermodynamic potential, as shown in Yang-Lee Zeros 4.1. Since the breakdown of the high-temperature expansion indicates a β-driven phase transition, it is possible to propose the term *dynamical phase transition* for non-analytical behavior in time t, which corresponds to "the breakdown of short time expansion in the thermodynamic limit in a critical time" [129]. LeClair *et al.* showed that Z can be defined as the partition function with boundary states $|\Psi_i\rangle$ separated by z [130],

$$Z(z) = \langle \Psi_1 | e^{-zH} | \Psi_2 \rangle \,, \tag{4.1}$$

where $|\Psi_1\rangle$ and $|\Psi_2\rangle$ represent the states at the boundaries, H denotes the bulk-Hamiltonian of the closed system, and $z \in \mathcal{C}$ is a complex parameter. For real $z = R$, $Z(R)$ is known as the boundary partition function. When z represents the

imaginary time $z = it$, the partition function describes the overlap amplitude

$$Z(z = it) = \langle \Psi_1 | e^{-itH} | \Psi_2 \rangle \,, \tag{4.2}$$

where e^{-itH} is defined as the unitary time-evolution operator, and $|\Psi_1(t)\rangle = e^{-itH} |\Psi_2\rangle$. The partition function contains the full information about the system's thermodynamic properties, and in the thermodynamic limit one defines the free energy density

$$f = -\lim_{N\to\infty} \frac{1}{N} \ln Z. \tag{4.3}$$

where N is the number of degrees of freedom. Here Eq. (4.3) indicates the existence of non-analyticities of the system in the evolution of time – namely, dynamical phase transitions (DPTs). DPTs can be described using Fisher zeros in the complex time plane, see Fig. 4.3. For finite size systems, Fisher zeros appear as points. For systems in the thermodynamic limit, Fisher zeros can coalesce onto lines often on low-dimensional systems, or they can accumulate to form areas on higher-dimensional systems. DPTs occur whenever such a line or boundary of an area hits the real-time axis indicated by the **dots** along the real-time axis, see Fig. 4.3b. Equations (4.2) and (4.3) therefore serve as the paradigmatic equations for the study of dynamical phase transitions in localizing systems.

4.4 Quantum Quench

As the complex parameter z transitions from a real-valued temperature β to an imaginary time it, we transition from thermalizing systems to localizing systems. To understand how a localizing system evolves in time, we introduce the notion of

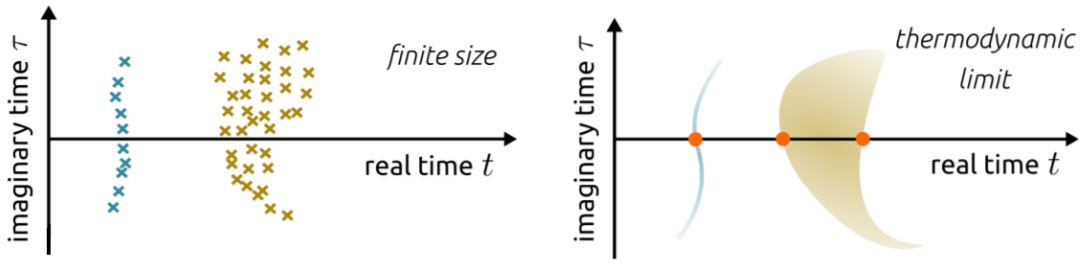

(A) (B)

FIGURE 4.3: Schematic illustration of Fisher zeros in the complex time plane. (A) For systems of finite size, the zeros appear as points in the complex parameter plane. (B) Upon increasing system size, Fisher zeros start to accumulate and form structures which can either lines or areas. Figures taken from Ref. [9]. Republished with permission of [Ye Cheng Chen], from [Dynamical phase transitions: a review, Reports on Progress in Physics, Vol. 8, 2018]; permission conveyed through Copyright Clearance Center, Inc..

quantum quench. A quantum quench is a parametric switch where, for a closed quantum system, the initial Hamiltonian H_0 evolves dynamically in time under a new Hamiltonian H_1 with a different parametric setting. We will only consider the so-called *global quenches*, which will lead to a macroscopic change in the Hamiltonian of a system. It is different from the *local quenches* where the energy change is not extensive. Consider a system initially prepared in the many-body ground state $|\Psi_0\rangle$ of an initial Hamiltonian H_0,

$$H_0 = H(g = g_0),$$

where g is some tunable parameter of a more general Hamiltonian $H(g)$, and the value g_0 parametrizes the initial Hamiltonian H_0. At time $t = 0$, the parameter g is suddenly changed to a new value g_1, and the final Hamiltonian is now

$$H_1 = H(g = g_1).$$

Let the final state $|\Phi_1\rangle$ be the many-body eigenstate of the Hamiltonian H_1. The overlap between the initial state $|\Psi_0\rangle$ and the final state $|\Psi_1\rangle$ after a global quench $g : g_0 \to g_1$ is known as the fidelity $\mathcal{F}$, defined as

$$\mathcal{F} = |\langle\Psi_0|\Psi_1\rangle|^2.$$

If $g_1 = g_0$ and $|\Psi_1\rangle = |\Psi_0\rangle$, then this is trivial and $\mathcal{F} = 1$, which it is possible in finite size systems. For large size systems reacting to a small perturbation, the initial state $|\Psi_0\rangle$ is almost always orthogonal to the final state $|\Psi_1\rangle$, and the overlap is exponentially small in system size L:

$$\mathcal{F} \propto e^{-L}.$$

This is known as the Anderson orthogonal catastrophe. The fidelity $\mathcal{F}$ is expected to vanish in the thermodynamic limit $L \to \infty$.

The quantum time-evolution of the initial ground state $|\Psi_0\rangle$ is defined as

$$|\Psi(t)\rangle = e^{-iH_1 t}\,|\Psi_0\rangle\,.$$

For a system that reacts to a global quench $g : \ g_0 \to g_1$, the dynamic overlap between the initial state $|\Psi_0\rangle$ and the time-evolved state $|\Psi(t)\rangle$ is defined as

$$\mathcal{L}(t) = |\langle\Psi_0|\Psi(t)\rangle|^2 = \left|\,\langle\Psi_0|e^{-iH_1 t}|\Psi_0\rangle\right|^2.$$

This is known as the Loschmidt echo. Heyl *et al.* showed that $\mathcal{L}(t)$ is a functional dependence on the number of degrees of freedom N in the large N limit,

$$\mathcal{L}(t) = e^{-Nl(t)},$$

where $l(t)$ is called the return rate function [129, 131], and it is defined as

$$l(t) = -\lim_{N\to\infty} \frac{1}{N} \ln \mathcal{L}(t).$$

Similar to non-analyticities which take place as Fisher zeros closing onto the real time axis, the non-analyticities of the return rate are determined by the zeros of the Loschmidt echo. Fig. 4.4 shows the schematic illustration for the Loschmidt echo $\mathcal{L}(t)$ and return rate $l(t)$. The rapid decay of the Loschmidt echo shows that $|\Psi_1\rangle$ and $|\Psi_0\rangle$ are orthogonal to each other. The cusps on the return rate function $l(t)$ are dynamical phase transitions at critical times t_c.

In conclusion, we have shown the development of phase transitions from thermalizing systems to dynamical localizing systems. Thermal phase transitions occur as non-analyticities provided by the free energy function, while the dynamical phase transitions are non-analyticities from the return rate function.

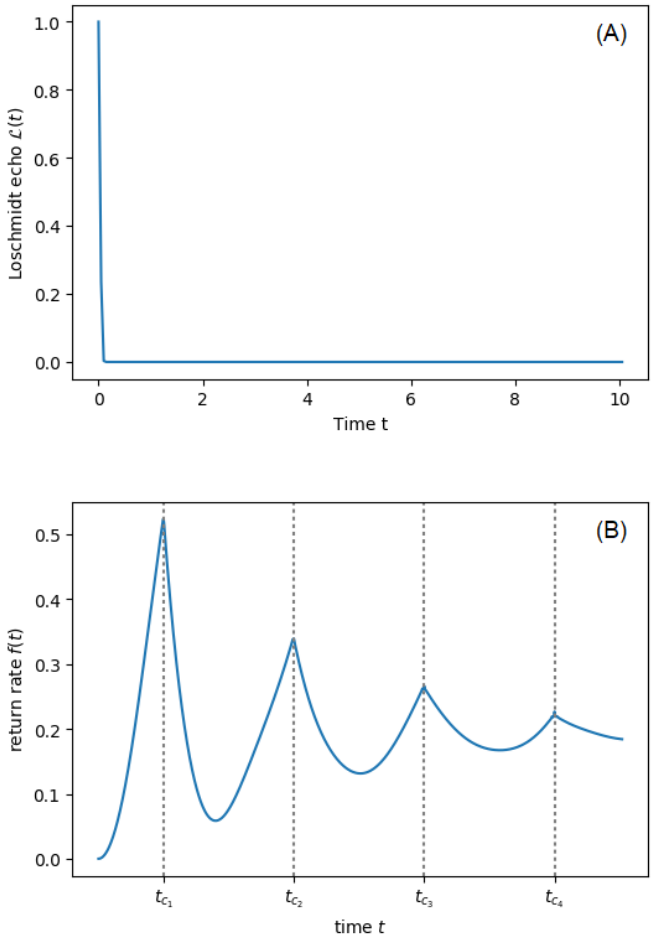

FIGURE 4.4: Schematic illustration of a dynamical quantum phase transition. (A) The Loschmidt echo decays exponentially and gives no further information. (B) The return rate $l(t)$ shows non-analyticities as cusps at several critical times $t = t_c$.

Chapter 5

The Loschmidt Echo

In the early days of statistical mechanics, Joseph Loschmidt in a discussion with Ludwig Boltzmann suggested the notion of time-reversal such that molecules could return to their initial positions after some time. This is quite impossible in classical mechanics for two reasons. First, according to the second law of thermodynamics, the entropy of an isolated system can never decrease over time; hence, the fact that entropy never decreases accounts for the irreversibility of molecules returning to initial positions. As seen from Anderson's orthogonality catastrophe, moreover, systems of many-particles, in the thermodynamic limit, possess exponential sensitivity on the variation of initial condition; hence, the initial state of a system reacting to an arbitrarily small perturbation would shift away and never return to its initial state. The fact that classical systems show exponential instability can be attributed to the concept of chaos, which is an intrinsic property in both classical and quantum systems. The field of quantum chaos mainly deals with stationary properties of classically chaotic systems, but recent studies pay attention to dynamical aspects of quantum evolution in chaotic systems, such as reversibility of quantum evolution and dynamical localization [132–135]. For systems with very few degrees of freedom, e.g., ideally a few non-interacting particles reacting to a weak perturbation, it is then possible to observe signs of time-reversal, where the time-evolved state returns to its initial state after an arbitrarily long time. This

is possible for closed systems because quantum evolution is unitary and preserves the short distance between two states; moreover, there is no significant exponential sensitivity due to the small variation of the initial state. For quantum systems reacting to strong perturbations or in contact with external reservoirs, the decoherence of the many-particle states is so strong that both quantum information is completely lost and time-reversal of system states is impossible. The question how stable such a time reversal is with respect to small perturbations is of fundamental importance to understand decoherence, which sets limits for quantum computation ([115, 136–138]). The measurement of sensitivity to perturbations is known as the Loschmidt echo, and understanding how sensitive dynamical phase transitions are due to disorder potential in localizing systems is our primary interest.

5.1 Definition of the Loschmidt Echo

For a closed quantum system, the time evolution of a quantum system is governed by a unitary operator $U(t) = e^{-iHt}$. Applying the unitary operator $U(t)$ on an initial quantum state $|\Psi_0\rangle$, the time evolution of the quantum state is $|\Psi(t)\rangle = U(t)|\Psi_0\rangle$. As a consequence, the initial quantum state can be recovered by applying the inverse of $U(t)$ on $|\Psi(t)\rangle$ such that $|\Psi_0\rangle = U^\dagger(t)|\Psi(t)\rangle$.

The Loschmidt echo is defined as the measure of the stability of time reversal,

$$\mathcal{L}(t) = |\langle\Psi_0|e^{iH(g_2)t}e^{-iH(g_1)t}|\Psi_0\rangle|^2. \tag{5.1}$$

Here, $H(g)$ is the time-independent Hamiltonian of the system which is a function of a microscopic parameter g. Eq. (5.1) states that the system is prepared in an

initial state $|\Psi_0\rangle$ which is allowed to time evolve during the forward time evolution for $g = g_1$. Then applying the backward time evolution $g = g_2$ would bring the quantum state back to the initial state and $\mathcal{L}(t) = 1$ if $g_1 = g_2$. In general, one wants to have g_2 different from g_1 to see how sensitive the state is from small perturbations. For $g_1 \neq g_2$, the system is time-evolved with $H(g_1)$ during the forward evolution and with $H(g_2)$ during the backward evolution. $\mathcal{L}(t)$ thus is nothing but the overlap of two quantum states between the time evolution state with $H(g_1)$ and the state with $H(g_2)$. Fig 5.1 shows the schematic flow of the time evolution for the Loschmidt echo.

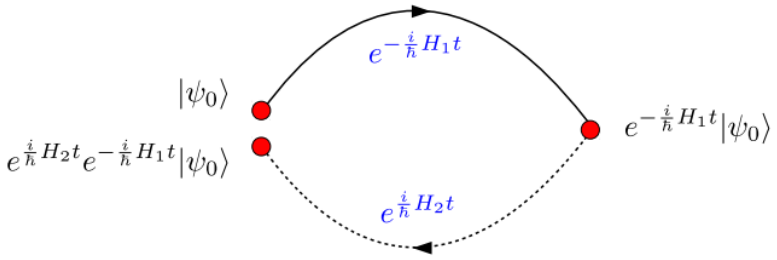

FIGURE 5.1: Schematic flow of the time evolution for the Loschmidt echo. Figure taken from Ref. [10] (arXiv License).

To study and classify quenches in closed quantum systems by means of the Loschmidt echo (LE), we concentrate on the case where $|\Psi_0\rangle$ is the ground state of $H(g_2)$. In this case, the Loschmidt echo takes the same form as in Sec. (4.4),

$$\mathcal{L}(t) = |\langle\Psi_0|e^{-iHt}|\Psi_0\rangle^2, \tag{5.2}$$

where we have set $H \equiv H(g_1)$.

Here we provide a short derivation of Eq. (5.2). Consider a closed system of N particles. Let $|\Psi_0\rangle$ be the ground state of $H(g_2)$. The hermitian operator $\hat{H}(g_2)$ satisfies the eigenvalue equation $\hat{H}(g_2)|\Psi_i\rangle = E|\Psi_i\rangle$, so that $\hat{H}(g_2)$ can be written

in terms its complete set of energy eigenvalues and eigenstates

$$\hat{H}(g_2) = \sum_m^N E_m \left|\Psi_m\right\rangle \left\langle\Psi_m\right|, \ m = 1 \ldots N.$$

It follows that $e^{i\hat{H}(g_2)t}$ written in terms of its energy eigenvalues and eigenstates is

$$e^{i\hat{H}(g_2)t} = e^{i\hat{H}(g_2)t} \cdot \mathbb{1} = e^{i\hat{H}(g_2)t} \sum_m \left|\Psi_m\right\rangle\!\left\langle\Psi_m\right| = \sum_m^N e^{iE_m t} \left|\Psi_m\right\rangle\!\left\langle\Psi_m\right|, \tag{5.3}$$

where $\sum_m^N e^{iE_m t} \left|\Psi_m\right\rangle \left\langle\Psi_m\right|$ is the complete set of energy eigenvalues on the diagonal axis and has the matrix form

$$\sum_m^N e^{iE_m t} \left|\Psi_m\right\rangle \left\langle\Psi_m\right| = \begin{pmatrix} e^{iE_1 t} & 0 & \ldots & 0 & 0 \\ 0 & e^{iE_2 t} & \ldots & 0 & 0 \\ \vdots & \vdots & \ddots & \vdots & \vdots \\ 0 & 0 & \ldots & e^{iE_{N-1} t} & 0 \\ 0 & 0 & \ldots & 0 & e^{iE_N t} \end{pmatrix}.$$

Substituting Eq. (5.3) into Eq. (5.1) , we have

$$\begin{aligned}
\mathcal{L}(t) &= \left| \langle\Psi_0|e^{iH(g_2)t}e^{-iH(g_1)t}|\Psi_0\rangle \right|^2 \\
&= \left| \langle\Psi_0|\sum_m^N e^{iE_m t}|\Psi_m\rangle \ \langle\Psi_m|e^{-iH(g_1)t}|\Psi_0\rangle \right|^2 \\
&= \left| \sum_m^N e^{iE_m t} \langle\Psi_0|\Psi_m\rangle \ \langle\Psi_m|e^{-iH(g_1)t}|\Psi_0\rangle \right|^2 \\
&= \left| e^{iE_0 t} \underbrace{\langle\Psi_0|\Psi_0\rangle}_{=1} \langle\Psi_0|e^{-iH(g_1)t}|\Psi_0\rangle \right|^2 \\
&= \underbrace{\left|e^{iE_0 t}\right|^2}_{=1} \left| \langle\Psi_0|e^{-iH(g_1)t}|\Psi_0\rangle \right|^2 \\
\therefore\ \mathcal{L}(t) &= \left| \langle\Psi_0|e^{-iH(g_1)t}|\Psi_0\rangle \right|^2.
\end{aligned}$$

Here the orthogonality relation of the eigenbasis is obeyed

$$\sum_m \langle\Psi_m|\Psi_0\rangle = \delta_{m,0}.$$

By setting $H \equiv H(g_1)$, we have arrived the desired Eq. (5.2)

$$\mathcal{L}(t) = |\ \langle\Psi_0|\ e^{-iHt}\ |\Psi_0\rangle\ |^2.$$

The return rate is defined as

$$l(t) = -\lim_{N\to\infty} \frac{1}{N} \ln \mathcal{L}(t). \tag{5.4}$$

For theoretical calculation purposes, it is important to emphasize the basis on which the calculation for Eq. (5.2) is performed. That is, the choice of the basis

matters. If $|\Psi_0\rangle$ is in the general basis, then e^{-iHt} must also be calculated in the general basis. In contrast to experimental techniques, where one can access the physical many-particle states in real space, having numerical calculations on the general basis is very challenging. Instead, once the Hamiltonian matrix is provided, one can immediately find the eigenvalues and eigenstates and calculate the Loschmidt echo in the eigenbasis. To set the initial state as the ground state of the system, one can numerically find the eigenstate from the Hamiltonian by matching the eigenvector to the smallest eigenvalue. Calculating the LE in the eigenbasis, therefore, imposes much convenience. Since $|\Psi_0\rangle$ is chosen in the eigenbasis, it is mandatory to transform the unitary time operator e^{-iHt} in the eigenbasis. We can rewrite the Loschmidt echo (5.2) in the eigenbasis for both the initial Hamiltonian $H(g_2)$ and the final Hamiltonian H,

$$\begin{aligned}\mathcal{L}(t) &= |\langle\Psi_0| e^{-iHt} |\Psi_0\rangle|^2 \\ &= |\langle\Psi_0| \mathbf{U}^\dagger e^{-i\mathbf{D}t}\mathbf{U} |\Psi_0\rangle|^2\end{aligned}$$

Therefore,

$$\mathcal{L}(t) = |\langle\Psi_0|\mathbf{U}^\dagger e^{-i\mathbf{D}t}\mathbf{U}|\Psi_0\rangle|^2. \tag{5.5}$$

Here $\mathbf{D}$ and $\mathbf{U}$ are the eigenvalues and eigenvectors of H obtained by exact diagonalization, respectively. The unitary time operator $e^{-iHt} = \mathbf{U}^\dagger e^{-i\mathbf{D}t}\mathbf{U}$ is now in the eigenbasis of H. If $|\Psi_0\rangle$ is not the eigenstate of the initial Hamiltonian $H(g_2)$, it is mandatory to project $|\Psi_0\rangle$ onto the eigenbasis $\mathbf{V}$ of $H(g_2)$. We can set $|\Psi_0\rangle$ as the ground state by numerically referring to the smallest eigenvalue of $H(g_2)$. Eq. (5.5) allows us to calculate the LE for both the SSH and the XXZ models at ease.

The Loschmidt echo equation (5.2) serves as the general formula both single-particle many-particle problems. As mentioned in Chapter 3, the many-particle Hamiltonian can consume much memory for large size systems, making calculations only feasible for small size systems. Because of the non-interacting character of initial state of a localized system, the system is non-interacting and the Hamiltonian is bilinear and hermitian [139]. Generally, a bilinear Hamiltonian following Jordan-Wigner transformation (JWT) can be described by the quadratic form in the free-fermion model. The bilinear Hamiltonian following Jordan-Wigner transformation (JWT) can be described by the quadratic form in the free-fermion model

$$\hat{H} = \sum_{i,j} \left[\hat{c}_i^\dagger A_{i,j} \hat{c}_j + \frac{1}{2} (\hat{c}_i^\dagger B_{i,j} \hat{c}_j^\dagger + h.c) \right], \tag{5.6}$$

where $\mathbf{A} = A_{i,j}$ is a real symmetric matrix due to hermiticity of H and $\mathbf{B} = B_{i,j}$ is a real antisymmetric matrix which follows from the anticommutation rules of the the annihilation and creation operators, c_i and $c_i^\dagger$, respectively [111]. An example of such system is the non-interacting SSH model, whose Hamiltonian is given by Eq. (3.5)

$$\hat{H} = J \sum_j \left[(1-\delta) \hat{c}_{j,A}^\dagger \hat{c}_{j,B} + (1+\delta) \hat{c}_{j,B}^\dagger \hat{c}_{j+1,A} + h.c) \right]. \tag{5.7}$$

To evaluate the time evolution of the LE, we can rewrite both Hamiltonians in Equations (5.6) or (5.7) in the following generic quadratic form

$$H = \mathbf{\Psi}^\dagger \mathcal{H} \mathbf{\Psi}, \tag{5.8}$$

where $\mathbf{\Psi}^\dagger = \left(c_1^\dagger \dots c_N^\dagger, c_1 \dots c_N \right)$, with c_k being the spinless Jordan-Wigner Fermion operators. $\mathcal{H} = \hat{\sigma}^z \otimes \mathbf{A} + i\hat{\sigma}^y \otimes \mathbf{B}$ is the matrix of the single-particle Hamiltonian.

The matrix elements of both the non-interacting SSH model (3.14) and the XX model (3.16) can be expressed in $\mathcal{H}$. The technique was developed by Elliott Lieb et al. for a 1D Heisenberg XY model , and the complete discussion can be found in Ref. [111].

The evaluation of LE for single-particle Hamiltonians can then have the following formula [140–142]

$$\mathcal{L}(t) = |\det(\mathbb{1} - \mathbf{C} + \mathbf{C}e^{-i\mathcal{H}t})|^2. \tag{5.9}$$

Here $\mathcal{H}$ is the matrix of the final Hamiltonian $H(g_1)$ after the quench during the forward evolution g_1. $\mathbf{C}$ is the $2N \times 2N$ correlation matrix whose matrix elements are simply the two-point correlation functions of the fermionic operators: $C_{ij} = \langle\Psi_0|\, \Psi_i^\dagger \Psi_j \,|\Psi_0\rangle$. $|\Psi_0\rangle$ is the ground state of the initial Hamiltonian $H(g_2)$. The symbol $\mathbb{1}$ is an $2N \times 2N$ identity matrix. The formula is a function of three ingredients: the two-point correlation matrix $\mathbf{C}$, the exponential matrix $e^{-i\mathcal{H}t}$, and the determinant form. We will provide an series of robust but comprehensive derivations to verify that Eq. (5.9) is indeed equivalent to Eq. (5.2) in Appendix (A); that is,

$$\mathcal{L}(t) = |\det(\mathbb{1} - \mathbf{C} + \mathbf{C}e^{-i\mathcal{H}t})|^2 = |\,\langle\Psi_0|\, e^{-iHt} \,|\Psi_0\rangle\,|^2. \tag{5.10}$$

5.2 The Loschmidt Echo for the Two Models

In this section, we will look at the analytical solution of the LE for both the SSH model and the XX model. In doing so, we provide analytical solution for the critical

times t_c for systems subject to periodic boundary conditions (PBC). Solutions for these models have been studied extensively [11, 115, 143].

5.2.1 The SSH Model

The method we use here follows closely the article [115]. We have shown in Chapter 3, the SSH Hamiltonian of N particles after a Fourier transform on a periodic lattice takes the form (3.5)

$$H = \sum_k \Psi_k^\dagger \mathcal{H}(k) \Psi_k \text{ with } \mathcal{H}(k) = \mathbf{d}_k \cdot \boldsymbol{\sigma},$$

where the vector $\mathbf{d}_k$ which parametrizes the system has the following form

$$\mathbf{d}_k = (-2J\cos(k), 2J\delta\sin(k), 0).$$

The dispersion relation in Eq. (3.7) is obtained by diagonalizing the Hamiltonian,

$$E(k) = \pm 2J\sqrt{\cos^2 k + \delta^2 \sin^2 k},$$

where the momenta $k = 2\pi n/N$ with $n = 1, 2, \ldots, L/2$ and $L = 2N$ is the total number of sites. If we quench $\mathbf{d}_k(\delta) = \mathbf{d}_k^0$ for $\delta > 0$ and $\mathbf{d}_k^1(\delta) = \mathbf{d}_k^1$ for $\delta < 0$, the Loschmidt echo amplitude, in a translationally invariant system of the form H, takes the following form [11, 144],

$$\mathcal{L}(t) = \prod_k \left[\cos(\epsilon_k^1) + i\mathbf{d}_k^0 \cdot \mathbf{d}_k^1 \sin(\epsilon_k^1 t)\right],$$

where $\mathbf{d}_k^{0,1} = \mathbf{d}_k^{0,1}/\sqrt{\mathbf{d}^{0,1} \cdot \mathbf{d}_k^{0,1}}$, $\epsilon_k^1 = |\mathbf{d}_k^i| = |E(k)|$ for the SSH model.

The Fisher zeros occur for $Z(z) = 0$ in Eq. (4.1), and the solution is given by

$$t_n(k) = \frac{\pi}{\epsilon_k^1}\left(n + \frac{1}{2}\right) + \frac{i}{\epsilon_k^1}\tanh^{-1}(\mathbf{d}_k^0 \cdot \mathbf{d}_k^1) \tag{5.11}$$

with n being an integer. In order to observe DPTs, Fisher zeros must be approaching the imaginary axis, which occurs when $\mathbf{d}_{k^*}^0 \cdot \mathbf{d}_{k^*}^1 = 0$ for a given k^*. Hence the imaginary part in Eq. (5.11) vanishes. These zeros lie on the real axis and therefore give rise to non-analytic behavior for the return rate at critical times [11],

$$t_n = \frac{\pi}{2\epsilon_{k^*}^1}(2n-1), \text{ where } n \in \mathbb{Z} \tag{5.12}$$

If multiple critical time exist, the critical time scale is defined as the smallest critical time t_{c_1}; in this case, $t_{c_1} = \pi/(2\epsilon_{k^*}^1)$.

For the system subject to open boundary conditions, the return rate in the large limit N can be expanded in the following form[11]

$$l(t) \sim l_0(t) + \frac{l_B(t)}{N}. \tag{5.13}$$

Here l_0 is the return rate from bulk contribution for PBC. l_B is the boundary contribution which contains information about the topologically protected edge states. A symmetric quench $\delta \to -\delta$ does not affect the direction of the quench for the the bulk contribution $l_0(t)$, see Fig. 5.2a. A quench from the trivial phase ($\delta < 0$) into the topological phase ($\delta > 0$) does strongly affect the boundary contribution $l_B(t)$, which shows large jumps at the critical times, see Fig. 5.2b. Fig. 5.2a shows multiple critical times, and the time scale is $t/t_c = 1$.

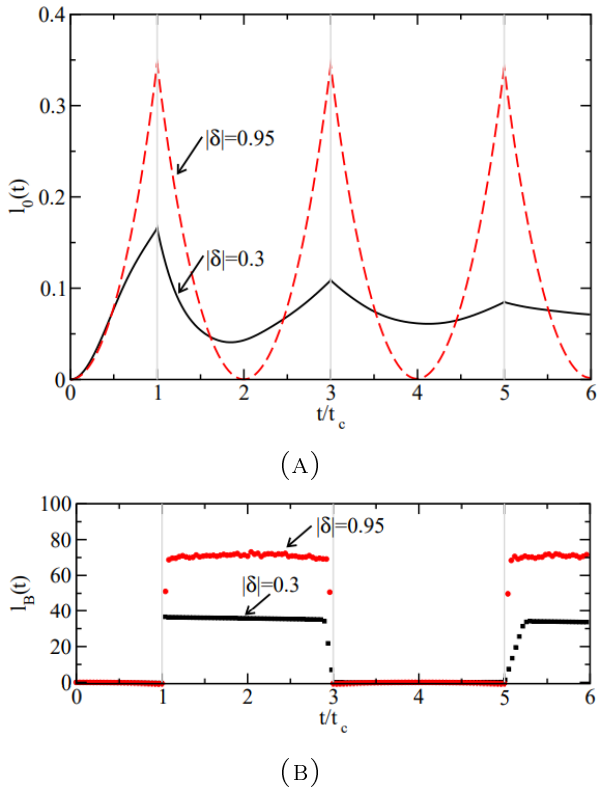

FIGURE 5.2: Return rates for the bulk contribution $l_0(t)$ and the boundary contribution $l_B(t)$ for the SSH Hamiltonian. (A) $l_0(t)$ for the bulk contributions for symmetric quenches $\delta \to -\delta$ for $\delta = 0.3$ and $\delta = 0.95$. (B) $l_B(t)$ for the boundary contribution for symmetric quenches from the trivial phase $\delta < 0$ into the topological phase $\delta > 0$. Reprinted with permission from [11] as follows: [N. Sedlmayr *et al.*, Bulk-boundary correspondence for dynamical phase transitions in one-dimensional topological insulators and superconductors. Phys. Rev. B, 97:064304, 2018.] Copyright (2019) by the American Physical Society.

5.2.2 The XX Model

Assume the 1D XX spin chain has an even number of lattice sites N and periodic boundary conditions. For $\triangle = 0$ and $h = 0$, the free fermionic Hamiltonian using the Jordan-Wigner transformation has the following form [115],

$$\hat{H}_0 = -\frac{J}{2}\left[\sum_{j=1}^{N-1}(\hat{c}_j^\dagger \hat{c}_{j+1} + h.c.) - e^{i\pi M}(\hat{c}_N^\dagger \hat{c}_1 + h.c.)\right]$$

As shown in Chapter 3, we can diagonalize H_0 via a Fourier transformation to

$$\hat{c}_j = \frac{1}{\sqrt{N}} \sum_{n=1}^{N} \hat{s}_{k_n} e^{ik_n R_j},$$

where $k_n = 2\pi n/N$, with $m = 0, \ldots, N-1$, is the wave vector. The Hamiltonian H_0 can be diagonalized as

$$\begin{aligned} H_0 &= \sum_{n=1}^{N} (\epsilon_k - h) \hat{s}^{\dagger}_{k_n} \hat{s}_{k_n} \\ &= \sum_{n=1}^{N/2} \left[(\epsilon_k - h) \hat{s}^{\dagger}_{k_n} \hat{s}_{k_n} - (\epsilon_{k_n} + h) \hat{d}^{\dagger}_{k_n} \hat{d}_{k_n} \right] \end{aligned}$$

Here $\epsilon_{k_n} = -J \cos(k_n + a)$ is the dispersion relation, and a is the lattice constant. The operator $\hat{d}_{k_n}$ is introduced here by folding the band into a reduced Brillouin zone. We consider the Néel state $|\uparrow\downarrow\uparrow\downarrow \ldots\rangle$ as the initial state $|\Psi_0\rangle$ of H_0 and quench from $|\Psi_0\rangle$ under the time evolution e^{-zH}. The time evolution of the initial state $e^{-zH} |\Psi_0\rangle$ is given by

$$e^{-zH} |\Psi_0\rangle = \frac{1}{\sqrt{2}} \prod_{n=1}^{N/2} \left[\left(e^{-z\epsilon_{k_n}} \hat{s}^{\dagger}_{k_n} - e^{z\epsilon_{k_n}} \hat{d}^{\dagger}_{k_n} \right) \right].$$

The Loschmidt echo amplitude becomes

$$\mathcal{Z}(z) = \prod_{n} \cosh(z\epsilon_{k_n}). \tag{5.14}$$

The return rate $l(t) = -1/N \ln |\mathcal{L}(t)|^2$ now has the form

$$l(t) = -\frac{1}{N}\sum_{n=1}^{N/2} \ln\left[\cos^2\left(t\epsilon_{k_n}\right)\right] \overset{N\to\infty}{\longrightarrow} -\frac{1}{2\pi}\int_{-\pi/2}^{\pi/2} dk \ln\left[\cos^2\left(t\epsilon_k\right)\right]. \tag{5.15}$$

The Fisher zeros happens for the zeros of the LE. The time evolved state has become orthogonal to the initial state. In the thermodynamic limit $N \to \infty$, non-analyticities are cusps in the return rate $l(t)$, and this happens when $\cos\left(t\cos\left(k=0\right)\right) = 0$. For systems of finite size N, the critical times are

$$t_c = \frac{\pi}{2\epsilon_{k_n}}(2m+1), \text{ where } m \in \mathbb{Z},\ n = 0, \ldots, N-1. \tag{5.16}$$

For systems in the thermodynamic limit $N \to \infty$, the critical times are

$$t_c = \frac{\pi}{2}(2m+1). \tag{5.17}$$

The *time scale* is $t_{c_1} = \pi/2$. Fig. 5.3 shows the return rate $l(t)$ in the thermodynamic limit. The cusps of $l(t)$ correspond to multiple critical time $t = t_c$ in Eq. (5.17).

In short, we have discussed the analytical solutions for the Loschmidt echo for systems with periodic boundary conditions. By diagonalizing Hamiltonians via Fourier transformations, the critical time scales for both the non-interacting SSH model and the XX model are found analytically. For systems with open boundary conditions (OBC), finding analytic solutions is very difficult, so we numerically investigate critical times for both models. We will discuss dynamical phase transitions and critical times for both disordered models with OBC in Chapter 6.

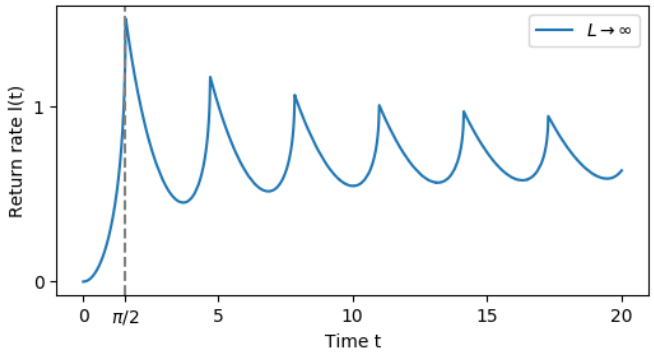

FIGURE 5.3: The return rate $l(t)$ in the thermodynamic limit obtained using Eq. (5.15). The time scale occurs at $t_c = \pi/2$, and subsequent critical times at $t_{c_1} = \pi/2(2m+1)$ for $m \geq 1$.

5.3 Comparison of the Formulas

In this section, we validate that the two Loschmidt echo equations (5.2) and (5.9) are indeed equivalent via an exact diagonalization technique for the disordered XX model with open boundary conditions. The same process also works for the SSH model. The disordered XX model is given by Eq. (3.16),

$$\hat{H}_{XX} = \frac{J}{2}\sum_{j=1}^{L}(\hat{c}_j^\dagger \hat{c}_{j+1} + \hat{c}_{j+1}^\dagger \hat{c}_j) + \sum_{j=1}^{L}\mu_j \hat{n}_j.$$

We show first numerical solutions for the clean (ordered) system with small system size $L = 2$ and $L = 4$. Since any mathematical derivation involving any larger system would be too lengthy, we will omit them here. We then verify the equations for the disordered system with system sites $L = 14$. We choose the many-body ground state of the initial Hamiltonian $H(g_2)$ to be the Néel state $|\uparrow\downarrow \ldots \uparrow\downarrow\rangle$. There are two implications. First, because the ground state is the Néel state, it implies that the $H(g_2)$ is in the antiferromagnetic phase. Secondly, because the XX model is in the Luttinger liquid (LL) phase, we quench the system from the

AFM phase into the LL phase. All that matters, however, is that we know the Néel state, which enters the equations for calculations. Because we work on the eigenbasis, we will use Eq. (5.5) for evaluating the many-particle Hamiltonian and Eq. (5.9) for the single-particle Hamiltonian. We denote the approaches using two separate equations for the single-particle and the many-particle problems as the singe-particle Hamiltonian approach (SPHA) and the many-particle Hamiltonian approach (MPHA), respectively.

5.3.1 The MPHA for $L = 2$

The final MPH H_f^{mp} of the clean XX model is

$$H_f^{mp} = \begin{pmatrix} 0 & 0.5 \\ 0.5 & 0 \end{pmatrix}.$$

The eigenvalues of H_f^{mp} are

$$E_1 = -0.5, \; E_2 = 0.5. \tag{5.18}$$

The eigenstates of H_f^{mp} are

$$|\Phi_1\rangle = \begin{pmatrix} -1/\sqrt{2} \\ 1/\sqrt{2} \end{pmatrix}, \; |\Phi_2\rangle = \begin{pmatrix} 1/\sqrt{2} \\ 1/\sqrt{2} \end{pmatrix}. \tag{5.19}$$

We use Eq. (5.5) to evaluate the Loschmidt echo,

$$\mathcal{L}(t) = |\, \langle \Psi_0 | \mathbf{U}^\dagger e^{-i\mathbf{D}t} \mathbf{U} | \Psi_0 \rangle \,|^2.$$

For $L = 2$, the Néel state in the eigenbasis of is

$$|\Psi_0\rangle = \begin{pmatrix} 1 \\ 0 \end{pmatrix}. \tag{5.20}$$

Using the eigenvalues from Eq. (5.18) and $\mathbf{D} = \{-0.5, 0.5\}$, we can write the exponential term $e^{-i\mathbf{D}t}$ as

$$e^{-i\mathbf{D}t} = \begin{pmatrix} e^{0.5it} & 0 \\ 0 & e^{-0.5it} \end{pmatrix}. \tag{5.21}$$

Using the eigenstates from Eq. (5.19), we can write the eigenbasis as

$$\mathbf{U} = \begin{pmatrix} -1/\sqrt{2} & 1/\sqrt{2} \\ 1/\sqrt{2} & 1/\sqrt{2} \end{pmatrix}. \tag{5.22}$$

Projecting the Néel state $|\Psi_0\rangle$ Eq. (5.20) onto the eigenbasis of H_f^{mp} gives

$$|\tilde{\Psi}\rangle = \mathbf{U}\,|\Psi_0\rangle = \begin{pmatrix} -1/\sqrt{2} & 1/\sqrt{2} \\ 1/\sqrt{2} & 1/\sqrt{2} \end{pmatrix} \begin{pmatrix} 1 \\ 0 \end{pmatrix} = \begin{pmatrix} -1/\sqrt{2} \\ 1/\sqrt{2} \end{pmatrix}.$$

From Eq. (5.5), we can evaluate the Loschmidt echo in following way

$$\begin{aligned}
\mathcal{L}(t) &= \left| \begin{pmatrix} -\frac{1}{\sqrt{2}} & \frac{1}{\sqrt{2}} \end{pmatrix} \begin{pmatrix} e^{0.5it} & 0 \\ 0 & e^{-0.5it} \end{pmatrix} \begin{pmatrix} -1/\sqrt{2} \\ 1/\sqrt{2} \end{pmatrix} \right|^2 \\
&= \left| \frac{1}{2} e^{0.5it} + \frac{1}{2} e^{-0.5it} \right|^2 \\
&= \left| \frac{1}{2} (\cos(0.5t) + i \sin(0.5t) + \cos(0.5t) - i \sin(0.5t)) \right|^2 \\
&= \left| \frac{1}{2} \cdot 2 \cos(0.5t) \right|^2 \\
&= |\cos(0.5t)|^2
\end{aligned}$$

Therefore,

$$\mathcal{L}(t) = |\cos(0.5t)|^2. \tag{5.23}$$

5.3.2 The SPHA for $L = 2$

The final SPH H_f^{sp} is the same as the final MPH for $L = 2$,

$$H_f^{sp} = \begin{pmatrix} 0 & 0.5 \\ 0.5 & 0 \end{pmatrix}.$$

The energy eigenvalues and eigenstates of the final Hamiltonian H_f^{sp} are the same as in Equations (5.18) and (5.19). The initial state is the Néel state in Eq. (5.20). From Eq. (5.9), $\mathcal{L}(t) = |\det(\mathbb{1} - \mathbf{C} + \mathbf{C}e^{-i\mathcal{H}t})|^2$, we need the correlation matrix $\mathbf{C}$ and the exponential term $e^{-i\mathcal{H}t}$. First, since the Néel state is now in the eigenbasis, the correlation matrix $\mathbf{C} = \langle \Psi_i^\dagger \Psi_j \rangle$ in the corresponding basis takes the matrix form in Eq. (A.9). For the Néel state (5.20), the two-point correlation matrix

becomes

$$\mathbf{C} = |\Psi_0\rangle\langle\Psi_0| = \begin{pmatrix} 1 \\ 0 \end{pmatrix} \begin{pmatrix} 1 & 0 \end{pmatrix} = \begin{pmatrix} 1 & 0 \\ 0 & 0 \end{pmatrix}.$$

Using the diagonal matrix of the energy eigenvalues in Eq. (5.21) and the eigenbasis in Eq. (5.22), we can evaluate $e^{-i\mathcal{H}t}$ in the eigenbasis

$$\begin{aligned}
\mathbf{U}^\dagger e^{-i\mathbf{D}t}\mathbf{U} &= \begin{pmatrix} -\frac{1}{\sqrt{2}} & \frac{1}{\sqrt{2}} \\ \frac{1}{\sqrt{2}} & \frac{1}{\sqrt{2}} \end{pmatrix} \begin{pmatrix} -\frac{e^{0.5it}}{\sqrt{2}} & \frac{e^{0.5it}}{\sqrt{2}} \\ \frac{e^{-0.5it}}{\sqrt{2}} & \frac{e^{-0.5it}}{\sqrt{2}} \end{pmatrix} \begin{pmatrix} -\frac{1}{\sqrt{2}} & \frac{1}{\sqrt{2}} \\ \frac{1}{\sqrt{2}} & \frac{1}{\sqrt{2}} \end{pmatrix} \\
&= \begin{pmatrix} \frac{e^{0.5it}}{2} + \frac{e^{-0.5it}}{2} & -\frac{e^{0.5it}}{2} + \frac{e^{-0.5it}}{2} \\ -\frac{e^{0.5it}}{2} + \frac{e^{-0.5it}}{2} & \frac{e^{0.5it}}{2} + \frac{e^{-0.5it}}{2} \end{pmatrix} \\
&= \frac{1}{2} \begin{pmatrix} e^{0.5it} + e^{-0.5it} & -e^{0.5it} + e^{-0.5it} \\ -e^{0.5it} + e^{-0.5it} & e^{0.5it} + e^{-0.5it} \end{pmatrix} \\
&= \frac{1}{2} \begin{pmatrix} 2\cos(0.5t) & -2i\sin(0.5t) \\ -2i\sin(0.5t) & 2\cos(0.5t) \end{pmatrix}.
\end{aligned}$$

Therefore,

$$e^{-i\mathcal{H}t} = \begin{pmatrix} \cos(0.5t) & -i\sin(0.5t) \\ -i\sin(0.5t) & \cos(0.5t) \end{pmatrix}.$$

Using Eq. (5.9), we can evaluate the Loschmidt echo

$$
\begin{aligned}
\mathcal{L}(t) =& |\det(\mathbb{1} - \mathbf{C} + \mathbf{C}e^{-i\mathcal{H}t})|^2 \\
=& \left| \det \left[\begin{pmatrix} 1 & 0 \\ 0 & 1 \end{pmatrix} - \begin{pmatrix} 1 & 0 \\ 0 & 0 \end{pmatrix} + \begin{pmatrix} 1 & 0 \\ 0 & 0 \end{pmatrix} \begin{pmatrix} \cos(0.5t) & -i\sin(0.5t) \\ -i\sin(0.5t) & \cos(0.5t) \end{pmatrix} \right] \right|^2 \\
=& \left| \det \left[\begin{pmatrix} 0 & 0 \\ 0 & 1 \end{pmatrix} + \begin{pmatrix} \cos(0.5t) & -i\sin(0.5t) \\ 0 & 0 \end{pmatrix} \right] \right|^2 \\
=& \left| \det \left[\begin{pmatrix} \cos(0.5t) & -i\sin(0.5t) \\ 0 & 1 \end{pmatrix} \right] \right|^2 \\
=& |\cos(0.5t)|^2.
\end{aligned}
$$

Therefore,

$$\mathcal{L}(t) = |\cos(0.5t)|^2. \tag{5.24}$$

In short, we have shown that Equations (5.23) and (5.24) give the same explicit solution for the clean XX model with system size $L = 2$. Fig. 5.4 shows the numerical solutions via exact diagonalization and the explicit solution $|\cos(0.5t)|^2$, and they agree with one another.

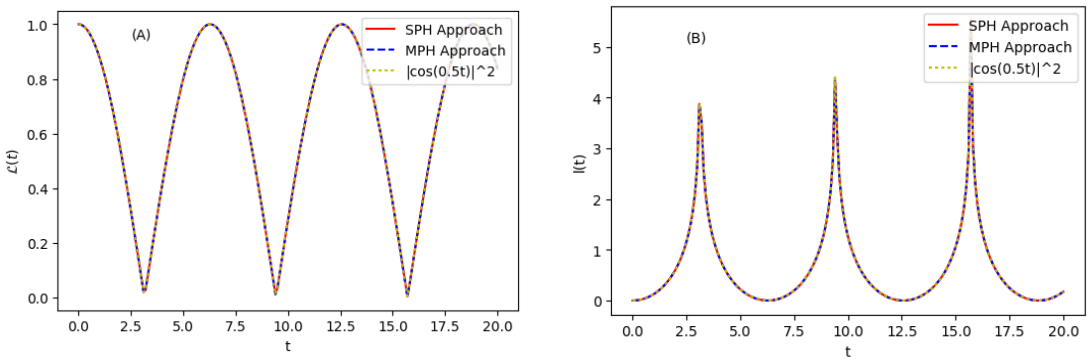

FIGURE 5.4: Numerical solutions obtained by exact diagonalization for (A) the Loschmidt echo $\mathcal{L}(t)$ and (B) the return rate $l(t)$ for the clean XX model with $L = 2$ system sites. The red (blue) line refers to numerical solutions using the SPHA (MPHA), while the yellow line refers to the explicit solution.

5.3.3 The MPHA for L=4

The system size is $L = 4$ with half-filling has $N = 2$ particles , so the size of the many-particle Hamiltonian is

$$\begin{pmatrix} 4 \\ 2 \end{pmatrix} = \frac{4!}{2!\ 2!} = 6,$$

which obeys the rule of the binomial coefficient. The clean MPH is obtained by performing fermionic operators $c_j^\dagger c_{j+1}$ on the XX Hamiltonian,

$$H^{mp} = \begin{pmatrix} 0 & 0.5 & 0 & 0 & 0 & 0 \\ 0.5 & 0 & 0.5 & 0.5 & 0 & 0 \\ 0 & 0.5 & 0 & 0 & 0.5 & 0 \\ 0 & 0.5 & 0 & 0 & 0.5 & 0 \\ 0 & 0 & 0.5 & 0.5 & 0 & 0.5 \\ 0 & 0 & 0 & 0 & 0.5 & 0 \end{pmatrix}.$$

The following calculations were performed using Mathematica, and the complete programming steps can be found in Appendix (B). The set of eigenvalues of H is

$$D = \{1.11803, 0.5, 0, 0, -0.5, -1.11803\}.$$

The ground state is the many-body Néel state in the eigenbasis

$$|\Psi_0\rangle = \begin{pmatrix} 1 \\ 0 \\ 1 \\ 0 \\ 1 \\ 0 \end{pmatrix},$$

Using Eq. (5.5) and follow the steps in Sec. (5.3.1) for $L = 4$, we obtain the following numerical solution

$$\mathcal{L}(t) = \frac{1}{16}\left|e^{-1.11803it} + e^{-0.5it} + e^{-0.5it} + e^{1.11803it}\right|^2. \tag{5.25}$$

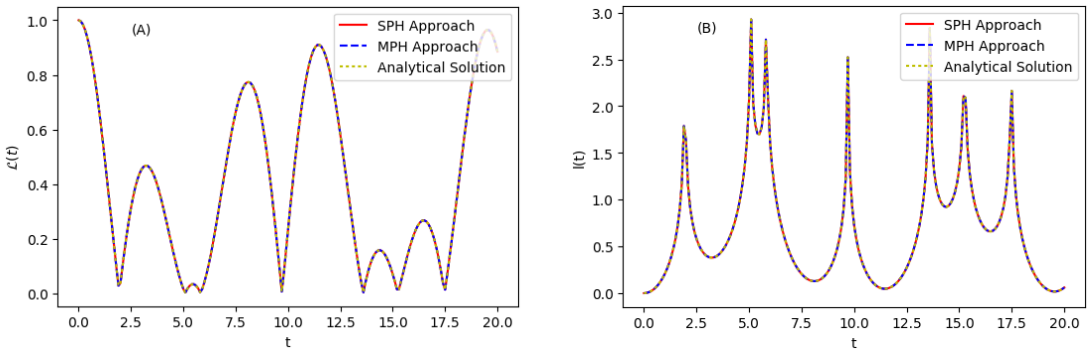

(A) (B)

FIGURE 5.5: Numerical solutions obtained by exact diagonalization for (A) the Loschmidt echo $\mathcal{L}(t)$ and (B) the return rate $l(t)$ for the clean XX model with $L = 4$ system sites. The red (blue) line refers to numerical solutions using the SPHA (MPHA), while the yellow line refers to the explicit solution.

5.3.4 The SPHA for $L = 4$

The single-particle Hamiltonian is different from the MPH for $L = 4$,

$$H^{sp} = \begin{pmatrix} 0 & 0.5 & 0 & 0 \\ 0.5 & 0 & 0.5 & 0 \\ 0 & 0.5 & 0 & 0.5 \\ 0 & 0 & 0.5 & 0 \end{pmatrix}.$$

The following calculations were obtained using Mathematica (see Appendix B) for the complete programming procedure. The set of eigenvalues of H is

$$D = \{0.809017, 0.309017, -0.309017, -0.809017\}.$$

The single-particle Néel state for system length $L = 4$ in the eigenbasis is

$$|\Psi_0\rangle = \begin{pmatrix} 1 \\ 0 \\ 1 \\ 0 \end{pmatrix}.$$

The correlation matrix in the eigenbasis basis $\mathbf{C}$ is

$$\mathbf{C} = |\Psi_0\rangle \langle\Psi_0| = \begin{pmatrix} 1 \\ 0 \\ 1 \\ 0 \end{pmatrix} \begin{pmatrix} 1 & 0 & 1 & 0 \end{pmatrix} = \begin{pmatrix} 1 & 0 & 0 & 0 \\ 0 & 0 & 0 & 0 \\ 0 & 0 & 1 & 0 \\ 0 & 0 & 0 & 0 \end{pmatrix}.$$

Using Eq. (5.9), we can evaluate the LE using the correlation matrix $\mathbf{C}$ and the exponential term $e^{-i\mathcal{H}t}$. The explicit solution obtained using Mathematica is

$$\mathcal{L}(t) = \frac{1}{16} \left| e^{-1.11803it} + e^{-0.5it} + e^{-0.5it} + e^{1.11803it} \right|^2. \tag{5.26}$$

As shown from Equations (5.25) and (5.26), the two approaches provide the same explicit solution for the clean XX model with $L = 4$. Fig. 5.5 shows both the numerical solutions and the explicit solution, and they agree with one another.

5.3.5 Comparison for $L = 14$ with Disorder

Now we verify numerically the Loschmidt echo equations (5.9) and (5.5) are equivalent for both disordered systems with system sites $L = 14$. Fig. 5.6 shows numerical solutions for the disordered XX model. Fig. 5.7 shows numerical solutions for

the disordered non-interacting SSH model. Both single-particle Hamiltonian and many-particle Hamiltonian approaches give the same disorder-averaged solution, which is averaged over 2000 samples. Therefore, the two Loschmidt echo equations are indeed equivalent in evaluating the disordered XX systems.

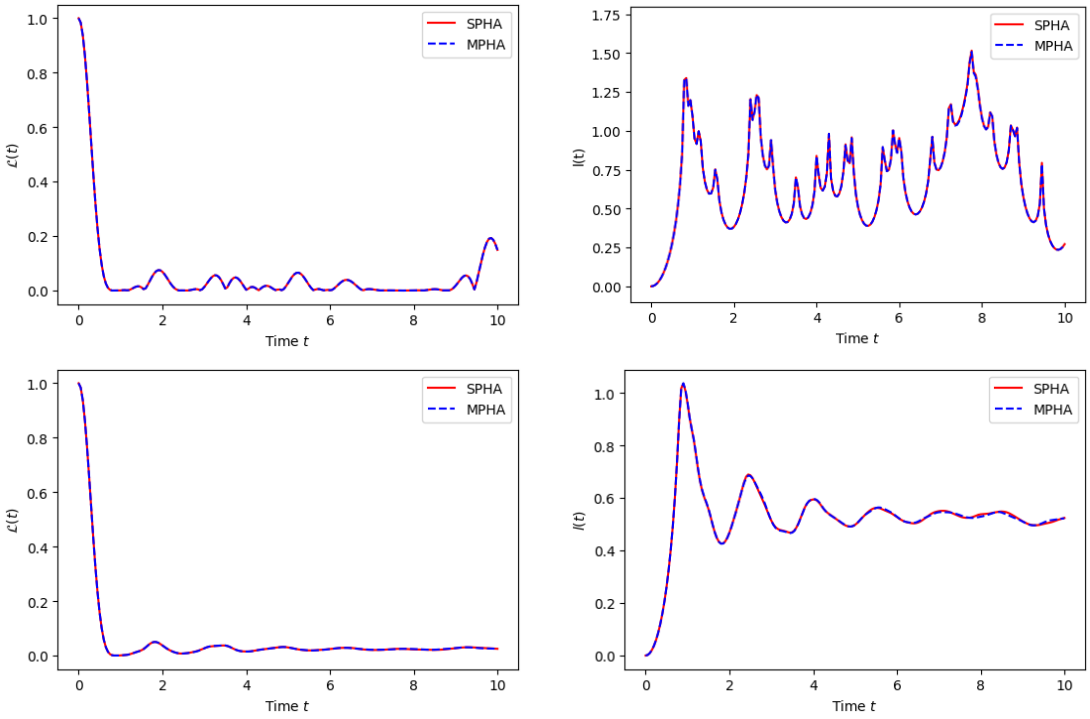

FIGURE 5.6: Numerical solutions for the evaluation of the disorder-averaged Loschmidt echo $\mathcal{L}(t)$ (left) and the corresponding return rate $l(t)$ (right) for the XX model with $L = 14$ system sites. Each result is averaged over 2000 samples. Top: $\mu \in [-W, W]$, with $W = 0.05$. Bottom: $\mu \in [-W, W]$, with $W = 0.5$.

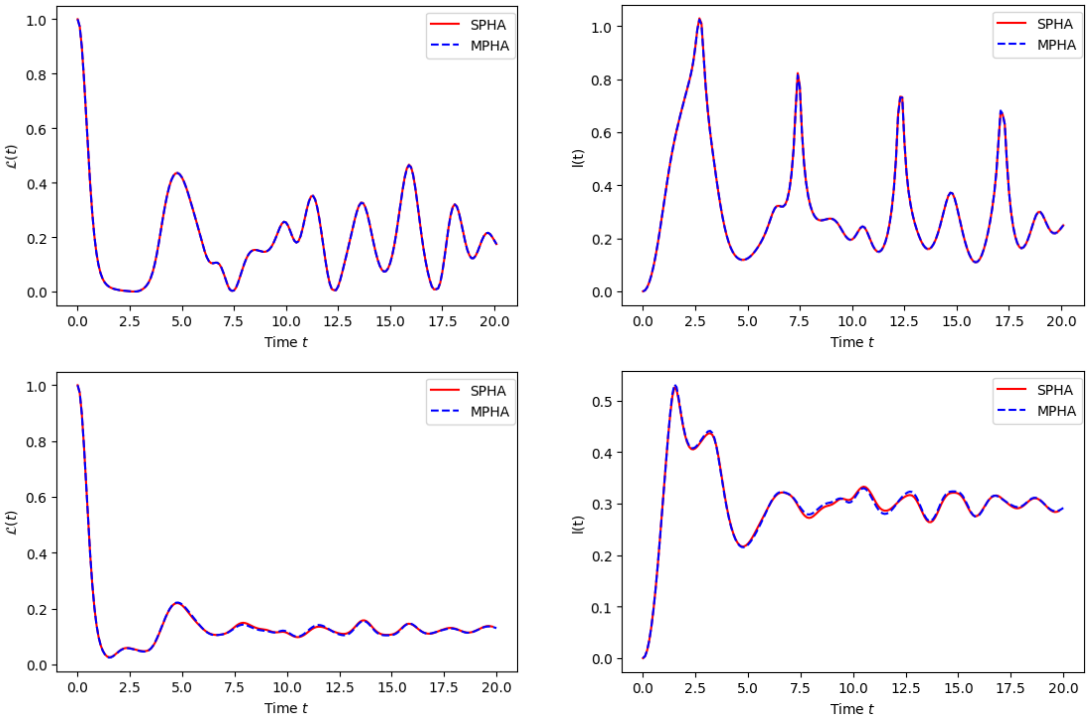

FIGURE 5.7: Numerical solutions for the evaluation of the disorder-averaged LE $\mathcal{L}(t)$ (left) and the corresponding RR $l(t)$ (right) for the disordered non-interacting SSH model quenching from the trivial phase $\delta = -0.5$ to the topological phase $\delta = +0.5$ with $L = 14$ system sites. Each result is averaged over 2000 samples. Top: $\mu \in [-W, W]$, with $W = 0.05$. Bottom: $\mu \in [-W, W]$, with $W = 0.5$.

5.4 Summary

In conclusion, we have discussed the concept of the Loschmidt echo. The general equation (5.2) can be used to approach both single-particle and many-particle problems. Alternatively, due to the non-interacting character of the single-particle problem, Eq. (5.9) can be used to approach non-interacting systems with large system size in eigenbasis. We show the analytical solutions in the thermodynamic limit for the non-interacting SSH model and the XX model with periodic boundary conditions. We have also provided comparisons for the two Loschmidt echo equations via exact diagonalization. We conclude that the equations provide equivalent solutions in evaluating non-interacting systems with finite system size. We also provide Mathematica algorithms for the XX model with system sizes $L = 2$ and $L = 4$ in Appendix (B). We will look at the disorder-averaged Loschmidt echo and investigate dynamical phase transitions for both disordered systems in the next chapter (6).

Chapter 6

Results

In this chapter, we will invesitgate the dynamical phase transitions for both the SSH model and the XXZ model with disorder. To do so, we will evaluate the disorder-averaged Loschmidt echo $\mathcal{L}(t)$ and the disorder-averaged return rate (DARR) $l(t)$. We will use the single-particle Hamiltonian approach (SPHA) for the disordered non-interacting models since these Hamiltonians have a bilinear form, and we will use the many-particle Hamiltonian approach (MPHA) for the disordered interacting models. For the SPHA, we evaluate the Loschmidt echo using Eq. (5.9),

$$\mathcal{L}(t) = |\det(\mathbb{1} - \mathbf{C} + \mathbf{C}e^{-i\mathcal{H}t})|^2. \tag{6.1}$$

For the MPHA, we evaluate the LE in the eigenbasis

$$\mathcal{L}(t) = |\,\langle\Psi_0|\mathbf{U}^\dagger e^{-i\mathbf{D}t}\mathbf{U}|\Psi_0\rangle\,|^2, \tag{6.2}$$

where $|\Psi_0\rangle$ is the many-body initial eigenstate of the initial Hamiltonian H_i. $\mathbf{U}^\dagger e^{-i\mathbf{D}t}\mathbf{U}$ is e^{-iHt} in the eigenbasis. The return rate is given by

$$l(t) = -\lim_{N\to\infty}\frac{1}{N}\ln\mathcal{L}(t). \tag{6.3}$$

According to Anderson localization, all one-particle states are localized in one

dimensional disordered systems for an arbitrary amount of disorder, parametrized by W. This is true for systems in the thermodynamic limit; however, one-particle states are not completely localized in finite size systems, especially in small size systems. As mentioned in Chapter 2, the localization length of the system is inversely proportional the disorder strength W^2; the larger the disorder strength W, the shorter the localization length. For 1D systems in the thermodynamic limit $N \to \infty$, the slightest disorder can perturb the system, so that the localization length is always shorter than the system length. For finite size systems, where the localization length is sometimes longer than the system size, only for large enough disorder can we see localization phenomenon. It is expected that dynamical phase transitions disappear for the presence of a certain amount of disorder for finite systems. Having this in mind, we are interested in the following questions for disordered systems.

1. Does the disorder-averaged return rate show dynamical phase transitions?
2. What is the time scale t_{c_1} at which dynamical phase transitions occur?
3. Because the one-particle states are all localized, is it true that the Loschmidt echo cannot decay completely?
4. What is the difference between interacting and non-interacting disordered systems?

6.1 The SSH Model

In this section, we will investigate the dynamical phase transitions for the non-interacting (NI) disordered SSH model and the interacting one. The non-interacting

disordered SSH model has the following many-particle Hamiltonian

$$\hat{H}_{SSH} = J\sum_{j=1}^{L}[(1+\delta e^{i\pi j})\hat{c}_j^{\dagger}\hat{c}_{j+1} + h.c.] + \sum_j \mu_j \hat{n}_j, \tag{6.4}$$

Here J is the hopping amplitude, δ is the dimerization parameter, L is the number of system sites, and $\mu_j \in [-W, W]$ with W being the disorder parameter. We use $J = 1$ throughout the calculations. The interacting disordered SSH model has the following form

$$\hat{H}_{SSH_{\triangle}} = J\sum_{j=1}^{L}[(1+\delta e^{i\pi j})\hat{c}_j^{\dagger}\hat{c}_{j+1} + h.c.] + \sum_j \mu_j \hat{c}_j^{\dagger}\hat{c}_j + \triangle\sum_{j=1}^{L}\left(\hat{n}_j\hat{n}_{j+1} - \frac{1}{4}\right), \tag{6.5}$$

where $\triangle$ is the nearest-neighbour interaction. Because Hamiltonian $\hat{H}_{SSH}$ (6.4) can take the bilinear (bipartite) form, we can evaluate the Lochmidt echo using the single-particle Hamiltonian approach (SPHA). However, due to the presence of edge states, there is numerical precision problem in the eigenvalues of the edge states when we evaluate large systems. We will first investigate the eigenvalue issue in the non-critical SSH model, followed by thourough investigations of the DPTs for the SSH model described above.

6.1.1 Numerical Precision Problem

The problem of the eigenvalues persists in the SSH model with open boundary conditions. The presence of the edge states is a natural phenomenon in topological materials, but it limits researchers from obtaining precise numerical results for large size systems. If we consider the clean SSH model without disorder ($W = 0$), the edge states are absent for systems with periodic boundary conditions and

in the trivial phase for systems with OBC. For the systems with OBC in the topological phase, the eigenvalues of the edge states (EES) are ideally zero in the thermodynamic limit. For finite system size, however, the eigenvalues are expected to decay exponentially as a function of the system size. The larger the system size, the smaller the EES. Due to computational limits in double-precision, the smallest value that Python can handle without much error is 1×10^{-15}. In other words, the EES cannot exceed this numerical limit, even though calculating the LE for large system size still possible.[1].

Fig. 6.1 shows the return rates for the SSH model with several system sizes. First, for systems with OBC, where we quench from topological phase $\delta = +0.5$ into the trivial phase $\delta = -0.5$, the return rates have the same shape as that for systems with PBC because there is no edge state in the final Hamiltonian (see both dashed and dotted lines). The edge states are absent in systems with PBC, regardless if we quench from or to the topological phase; hence, such quench direction is called the symmetric quench. We denote the symmetric quench using the absolute value of the dimerization $|\delta|$. Secondly, we quench the system from $\delta = -0.5$ into $\delta = +0.5$ for systems with OBC; two edge states are present, see insect of Fig. 6.1. For system size $L = 60$, the first sharp cusp indicates a genuine DPT, which correspond to the first genuine critical time or time scale. As we increase the system size, the return rates and DPTs for larger systems theoretically are expected to be comparable to those for $L = 60$. However, we see that, for larger systems, the first and second cusps split apart. The splitting of the these dynamical phase transitions for large systems is because of the numerical precision problem,

[1]Handling very small digits is possible with a multiprecision library in Python, such as mpmath.

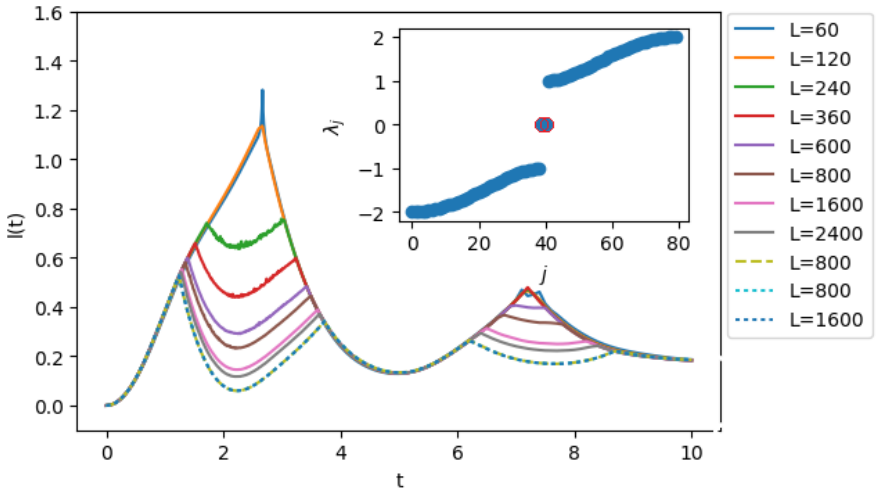

FIGURE 6.1: Return rates for the non-interacting SSH model with different system sites L. The splitting of the dynamical phase transitions for systems in OBC are due to numerical precision limits. Solid lines: quench from $\delta = -0.5$ into $\delta = +0.5$ for OBC. Dashed line: quench from $\delta = +0.5$ into $\delta = -0.5$. Dotted lines: systems with PBC. Insert: eigenvalues λ_j versus sites j showing two edge states near zero for system sites $L = 60$.

for which EES are not resolved numerically.

How fast the eigenvalues of the edge states decay exponentially depends on the chosen dimerization parameter δ. We look at the absolute eigenvalue of one of the edge states, $|\lambda_j|$ with $j = L/2$, versus system sites L for systems with OBC, where we quench systems from the trivial phase $\delta < 0$ to the topological phase $\delta > 0$. We consider three dimerizations, $\delta = 0.95$, 0.5 and 0.15. Fig. 6.2 shows the linear log-plots of $|\lambda_j|$ versus L for eigenvalues resolved properly within the numerical precision limit. For $\delta = 0.95$, $|\lambda_j|$ quickly reaches the numerical precision limit for system size $L = 20$, and eigenvalues on any larger system sizes would not go below the limit. For $\delta = 0.5$, accurate $|\lambda_j|$ survives for up to $L = 60$, whereas $|\lambda_j|$ is still accurate for $L = 200$ in the case $\delta = 0.15$. Fig. (D) of (6.2) shows the return rates for clean systems with various system sizes where EES are resolved properly.

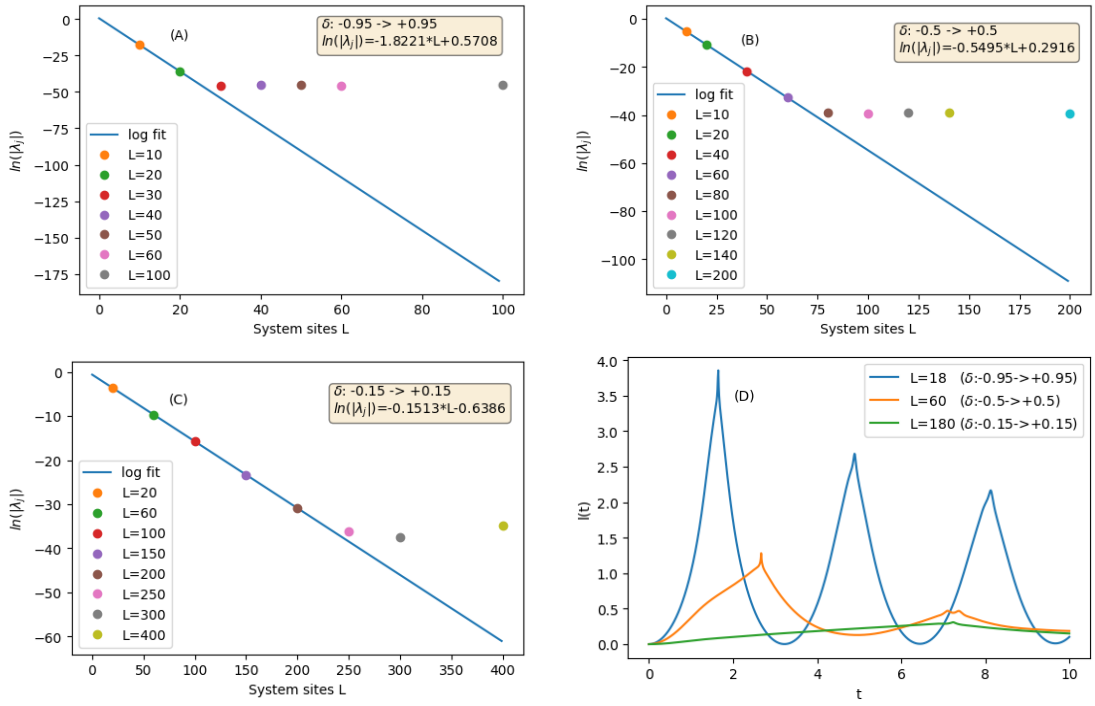

FIGURE 6.2: Plots of the log of absolute value of one of the eigenvalues of edge states $\ln(|\lambda_j|)$ versus system sites L for systems with OBC quenching from $\delta < 0$ into $\delta > 0$. (A) $\delta = 0.95$. (B) $\delta = 0.5$. (C) $\delta = 0.15$. Eigenvalues within the numerical precision limit decay exponentially with system sites. (D) Return rates for different system sizes quenching with specific dimerization.

For $L = 18$ and $\delta = 0.95$, the return rate shows three periodic dynamical phase transitions in the short times. For $L = 200$ and $\delta = 0.15$, the amplitude of return rate is much smaller, and there is only one DTPs which can barely be identified. For $L = 60$ and $\delta = 0.5$, there are two DPTs. For small systems with OBC, we will consider these system sizes with corresponding dimerizations so that the EES are resolved numerically.

The main purpose to highlight the numerical problem is to find an alternative route to verify the Anderson localization. Since the EES problem presists in the SSH model, we are forced to use small size systems, but it is not helpful in verifying

the Anderson localization for this model. The alternative route we found is to exploit the fact that the eigenvalue of edge states is not proportional to the system length L for disordered systems, but it is proportional to the disorder parameter W for a given system length. For the SSH model with sites $L = 60$, we can compare the results where EES are resolved properly. According to the equation in Fig. 6.2B,

$$\ln |\lambda_j| = -0.5495 \cdot L + 0.2916, \tag{6.6}$$

for the system with $L = 800$ and $|\delta| = 0.5$, the EES is around 6.1×10^{-192}. No computer in the world can resolve numerically this eigenvalue at this point. However, due to the on-site disorder potential defined in Eq. (6.4), we found that the disorder-averaged EES $|\lambda_j^*|$ is a log-log function of the disorder parameter W, see Fig. 6.3. Here is an example. We look at the system with OBC, where we quench from $\delta = -0.5$ into $\delta = +0.5$, and the system length is $L = 800$. For the clean system, the EES cannot be resolved properly and the LE gives wrong results, see Fig. 6.1. As we turn on the disorder W for the disordered system, however, we found that the absolute value of EES $\ln |\lambda_j^*|$ versus the disorder parameter W obeys a linear log-log function, as shown in Fig. 6.2 C,

$$\ln |\lambda_j^*| = 1.0041 \cdot \ln W - 0.7314. \tag{6.7}$$

Fig. 6.3 shows the log-log plots of the $|\lambda_j^*|$ versus W for all three dimerizations. This means that we can still verify the Anderson localization for the large size SSH model with OBC; that is, we can use equations (6.6) and (6.7) to show whether or not there is a disorder regime, corresponds to both the EES and, hopefully, a very small value of W. At this point the conjecture is still a hypothesis, but we

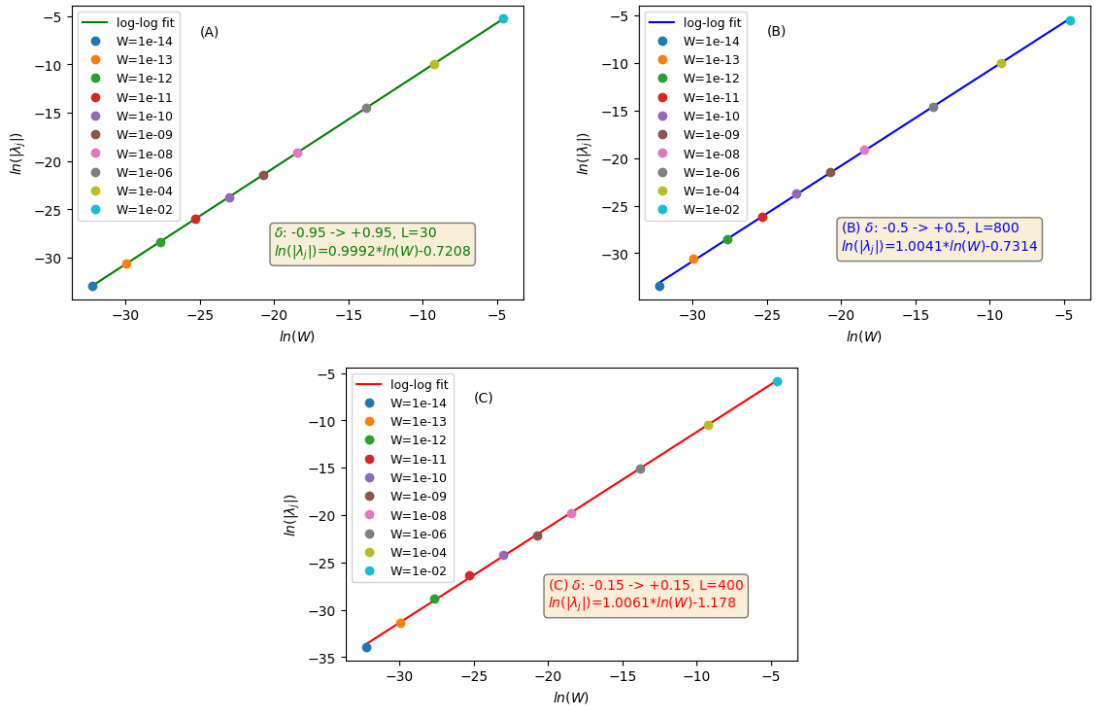

FIGURE 6.3: Log-log fit for the absolute value of EES $|\lambda_j|$ versus the disorder parameter W for large systems with different quenches. Eigenvalues are averaged over 30 disordered samples.

will soon show that there is a disorder regime for the non-critical disordered SSH model with system sites $L = 800$.

6.1.2 The Non-interacting Disordered SSH Model

Following the previous discussion, we would like to invesitigate dynamical phase transitions and verify the Anderson localization. For finite systems that are weakly disordered, not all single-particle states are localized. The localization length is longer than the system length, and the strong localization phenomena cannot be

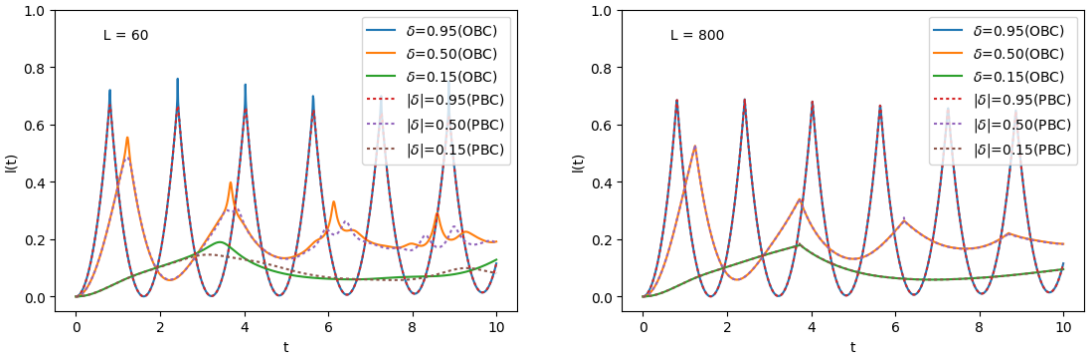

FIGURE 6.4: Comparisons of return rates between clean non-interacting SSH models with PBC and those with OBC where the system is quenched from the topological phase $\delta > 0$ into the trivial phase $\delta < 0$. Left: System sites $L = 60$. Right: System sites $L = 800$.

observed due the disorder strength W being weak. The static localization phenomon is shown in the ultra-cold laser experiment, see Fig. 2.6, and the dynamical localization phenomena can be seen from the disorder-averaged return rates (DARRs), which are obtained by evaluating the disorder-averaged Loschmidt echo. For the non-critical disordered SSH model, the problem reduces to the single-particle problem and the Hamiltonian has the bilinear form; we can evaluate the LE can using Eq. (6.1). As mentioned before, we will consider the disordered system with both open and periodic boundary conditions. A set of three dimerizations will be used; namely $\delta = 0.95$, 0.5 and 0.15. For systems with OBC, we quench the system from the trivial phase into the topological phase and consider both small and large systems. For small systems where the EES are numerically resolved, we use system sites $L = 18$ with $\delta = 0.95$, $L = 60$ with $\delta = 0.5$ and $L = 180$ with $\delta = 0.15$. We then consider large system size with sites $L = 800$ and dimerization $\delta = 0.5$. For systems with PBC in small system size, return rates do not show DPTs for some dimerizations, because the system size is too small to

simulate systems with periodic boundary conditions, see Fig. 6.4. We then consider large systems with PBC and small systems with OBC quenching from $\delta > 0$ into $\delta < 0$. Therefore, we consider the following cases:

A.I. small systems with OBC, quenching from $\delta < 0$ into $\delta > 0$;

A.II. large systems with OBC, quenching from $\delta < 0$ into $\delta > 0$;

A.III. small systems with OBC, quenching from $\delta > 0$ into $\delta < 0$;

A.IV. large systems with PBC, symmetric quench $|\delta|$.

To begin with, we consider the first case A.I. for three system sizes and dimerizations. The first disordered system (A) we consider has sites $L = 60$ and dimerization $\delta = 0.5$. We compare the DARRs $l^*(t)$ and their derivatives in time dl^*/dt with those for the clean system, see top figures of 6.5. For a range of disorder strengths W, such as $1 \times 10^{-14} \leq W \leq 1 \times 10^{-7}$, the DARRs and the return rate of the clean system overlap with one another, and dl^*/dt show sharp dicontinuities across the first critical time t_{c_1}, the time scale. For $W \geq 1 \times 10^{-6}$, the plots of DARRs show obvious splittings at the first cusps, but dl^*/dt is no longer sharp across the time scale t_{c_1}. The smoothness of dl^*/dt across the time scale is the indication of the disappearance of the first dynamical phase transition. By observing dl^*/dt, we can, therefore, define the weak disorder potential box as the weak disorder regime (WDR), where DPTs are as sharp across critical times as those for the clean system. The strong disorder regime (SDR) is anywhere outside the weak disorder regime. For single-particle systems, the first DPT suffices to show the difference, and the time scale can be numerically determined. For the system (i), the weak disorder regime is within the disorder potential box $[-W, W]$ with

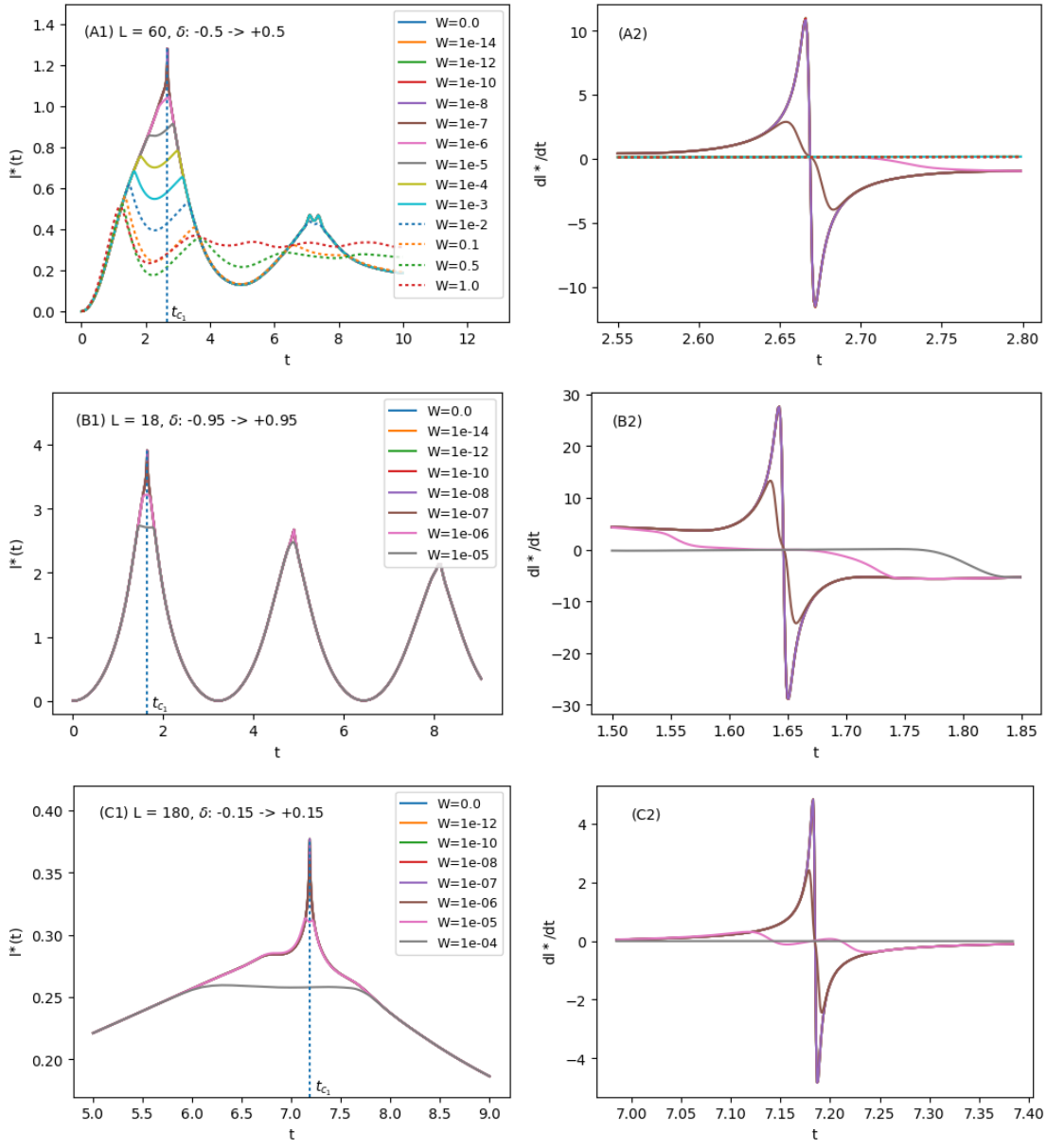

FIGURE 6.5: Disorder-averaged return rates $l^*(t)$ (left), and the derivatives dl^*/dt in the vicinity of the first cusp (right), for the non-interacting disordered SSH model with OBC. The systems are quenched from the trivial phase $\delta < 0$ into the toplogical phase $\delta > 0$. Top: System sites $L = 60$ and dimerization $\delta = 0.5$. Middle: $L = 18$ and $\delta = 0.95$. Bottom: $L = 180$ and $\delta = 0.15$ for $t \in [5.0, 9.0]$. Each result is averaged over 2500 random samples.

$W = 1 \times 10^{-7}$, and the regime for $W > 1 \times 10^{-7}$ is strongly disordered. The time scale t_{c_1} is 1.647. The DARRs for system sites (B) $L = 18$ with $\delta = 0.95$ and (C) $L = 180$ with $\delta = 0.15$ are also shown in Fig. 6.5. The weak disorder regimes correspond to $W = 1 \times 10^{-8}$ for both cases (B) and (C), and the time scales are 2.669 and 7.186, respectively.

We now turn to the second case A.II. for large system size $L = 800$. We quench the system with OBC from the trivial phase $\delta = -0.5$ into the topological phase $\delta = +0.5$. Since eigenvalues of edge states cannot be numerically resolved for large system size due to numerical precision limit, we are unable to directly compare DARRs to the return rate of clean system. To find the weak disorder regime, we need four equations. The first equation is Eq. (6.6), which gives the EES as a function of system size. The second equation is Eq. (6.6), which gives the ESS as a function of disorder strength W for $L = 800$ and δ: $-0.5 \rightarrow +0.5$. The third equation comes from the observation that the time scale of the DARRs, $t_{c_1^*}$, decrease as we increase the disorder strengths $W \leq 0.05$. Fig. 6.6 shows the log-log linear fit for $t_{c_1^*}$ and W, and the equation is determined by interpolation to be

$$\ln(t_{c^*}) = -0.0026 \cdot \ln(W) + 0.2134. \tag{6.8}$$

The localization length is expected to be comparable to or longer than the system length in the weak disorder regime for large size systems. That is, the disorder strengths for large size systems are expected to be a very small value, according to $\xi_{loc} \propto W^{-2}$ in Eq. (2.2). Moreover, the first dynamical phase transition for the disordered system is expected to be the same as that for the clean system, see Fig. 6.1. To find the weak disorder regime, we assume that the time scales of the first

DPT occur at the same time $t_{c_1} = 2.669$ for both system sizes $L = 60$ and $L = 800$. First, we locate t_{c_1} by referring to system sites $L = 60$: $t_{c_1} = 2.669$. Using Eq. (6.8), we found that $\ln(W) = [\ln(2.669) - 0.2134]/(-0.0026) = -294.2169$ and $W = 1.67 \times 10^{-128}$. Substitute $\ln(W)$ into Eq. (6.7), we get the disorder-averaged $|\lambda_j^*|$ =exp$[1.0041 \cdot \ln(-294.2169) - 0.7314] = 2.48 \times 10^{-129}$. This is the absolute value of an EES for this case, and the DARR for $W \leq 1.67 \times 10^{-128}$ overlaps hypthetically with the clean system.

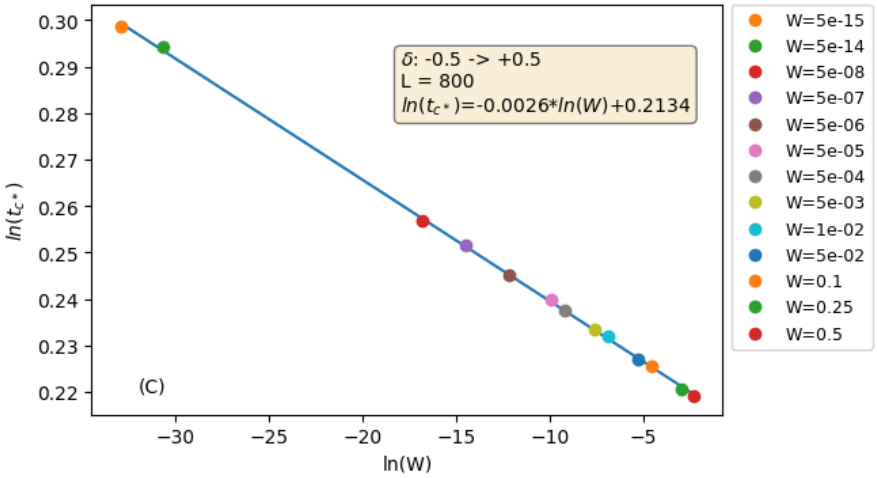

FIGURE 6.6: The log-log plot of time scales t_{c^*} versus disorder parameters W for system sites $L = 800$.

Because the system is subject to open boundary conditions, we can not find the localization length by means of constructing an analytical solution. To see if this W is a reasonable value, we resort to comparison of numerical solutions and graphical observations. We first notice that for the system with $L = 60$, the weak disorder regime is $W \leq 1 \times 10^{-8}$. Using Eq. (6.7), the disorder-averaged EES is found as $|\lambda_j^*| = 4.46 \times 10^{-9}$, and the clean EES $|\lambda_j|$ is 6.42×10^{-15}. The ratio of $|\lambda_j^*|/|\lambda_j|$ is about 6.94×10^5. Turning back to the system with $L = 800$, we find the ESS of

the clean system as $|\lambda_j|$ =exp$(-0.55 \cdot 800 + 0.29) = 1.62 \times 10^{-191}$. The disorder-averaged EES is $|\lambda_j^*| = 2.48 \times 10^{-129}$. The ratio in $|\lambda_j^*|/|\lambda_j| = 1.53 \times 10^{62}$. To understand this ratio, we look deeper into the validity of this solution by resorting to graphical observations.

To see whether this W makes sense, we can locate hypothetically the first DPT for the disordered system with $L = 800$ and $W = 1.67 \times 10^{-128}$. We notice that the tipping points on the DARRs follow a hypothetical straight line, which eventually converges to the first DPT, see Fig. 6.7 A. We found the following equation of this hypothetical line as

$$y(t_{c^*}) = 0.5221 \cdot t_{c^*} - 0.1229, \tag{6.9}$$

where $y(t_{c^*})$ is the tipping point of the on the return rate for a given W. Using Eq. (6.9) and assuming $t_{c_1} = t_{c^*} = 2.669$, we find that $y(t_{c^*}) = 1.271$. The tipping point on the return rate for $L = 60$ is found numerically as $y(t_{c_1}) = 1.283$. The ratio is $y(t_{c^*})/y(t_{c_1}) = 0.991$. Since this ratio is very small, and given the assumption that $t_{c_1} = t_{c^*}$, it is reasonable to believe that the first DPT for the disordered system with $W \leq 1.67 \times 10^{-128}$ would be as sharp across the time scale as the clean system, by means of graphical observations. The DARR is expected to overlap with the return rate of the clean system. For the disordered SSH model with OBC and finite size, we have seen that the weak disorder regime reduces as we increase the system size. In the weak disorder regimes, not all single-particle states are localized, and the Loschmidt echo can decay completely. For such system in the thermodynamic limit, however, we are expected to see that the single-particle states must be localized for an infinitesimally small degree of disorder strength. The LE cannot decay completely because there is no longer a weak disorder regime.

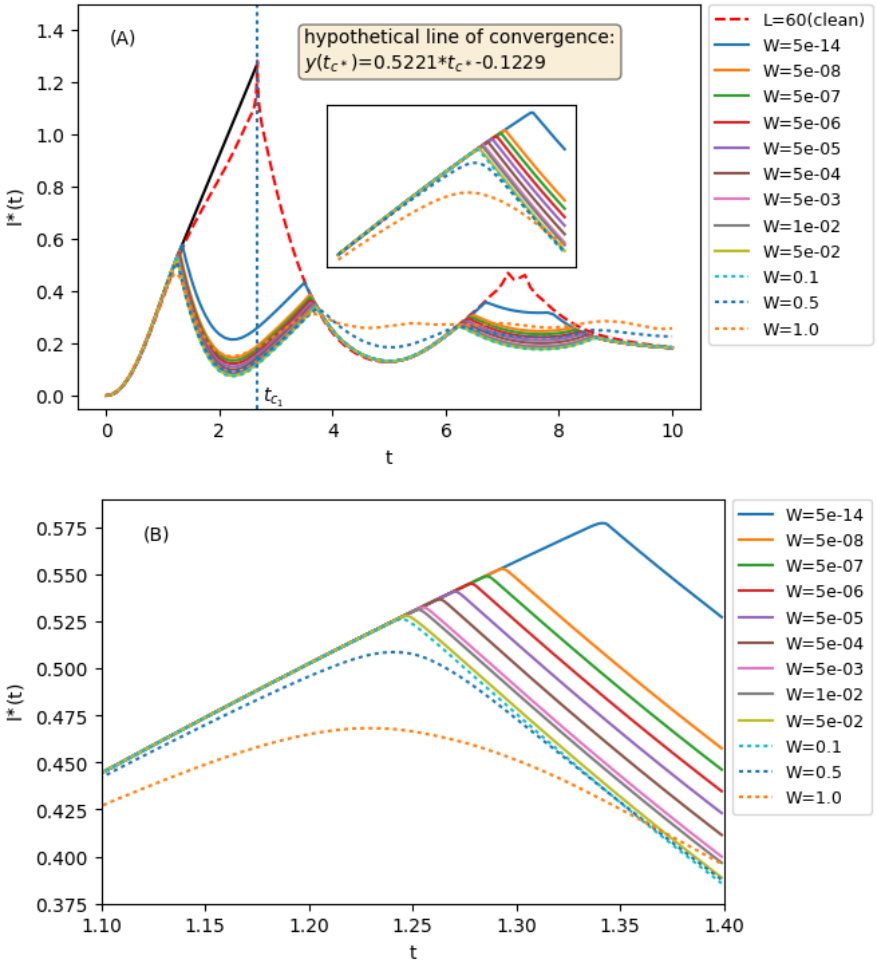

FIGURE 6.7: (A) Disorder-averaged return rates for the non-interacting disordered SSH model with OBC and system sites $L = 800$. The system is quenched from the trivial phase $\delta = -0.5$ into the topological phase $\delta = +0.5$. (B) Enlargement of the first few tipping-points on the return rates. Each result is averaged over 2500 random samples.

Next, we consider disordered SSH model with OBC quenching quenching from $\delta > 0$ into the trivial phase $\delta < 0$, see case A.III.. The edge states are absent in this case, so the problem of almost-zero eigenvalues is worry-free. We can then look at two systems both with system sites $L = 60$ but different dimerizations: $\delta = 0.95$ and 0.5. Fig. 6.8 shows the DARRs and their derivatives for the two systems. The

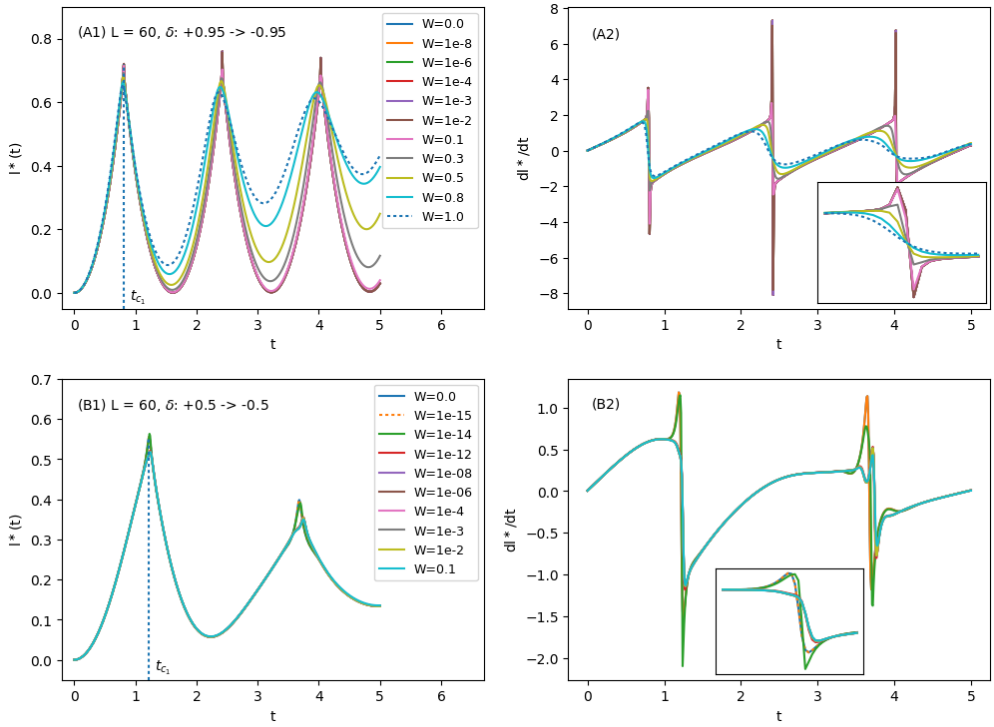

FIGURE 6.8: Disorder-averaged return rates $l^*(t)$, and the corresponding derivatives dl^*/dt of the DARRs, for the non-interacting disordered SSH model with OBC and system sites $L = 60$. The disordered systems are quenched from the topological phase $\delta > 0$ into the trivial phase $\delta < 0$. Top: Symmetric quench $|\delta| = 0.95$. Bottom: Symmetric quench $|\delta| = 0.5$. Insects: Zoom-in of the first cusp in dl^*/dt. Each result is averaged over 2500 random samples.

system with $\delta = 0.5$ is very susceptible to disorder, for the first DPT of the clean system is already different from that of the disordered system for $W = 1 \times 10^{-14}$. dl^*/dt for $W = 1 \times 10^{-15}$ overlaps with dl/dt for the clean system; hence, the WDR for this system is for $W = 1 \times 10^{-15}$, and the time scale is $t_{c_1} = 0.81$. The WDR for the system with $\delta = 0.95$ is for $W = 0.01$ with a time scale $t_{c_1} = 1.22$.

We now turn to the disordered system with PBC, the last case A.IV. for the single-particle Hamiltonian. Here we look at three cases: $L = 300$ with $|\delta| = 0.95$, $L = 300$ with $|\delta| = 0.5$ and $L = 800$ with $|\delta| = 0.5$. As shown in Fig. 6.9, we observe that disorder parameter $W = 0.1$ serves as a threshold between the weak

and strong disorder systems for the three cases here. For systems with $W < 0.1$, the DARRs of disordered systems overlap with the return rate of the clean system $W = 0$; the DTPs are as sharp as those for the clean system. For systems with $W \geq 0.1$, the return rates become become smooth and DPTs disappear.

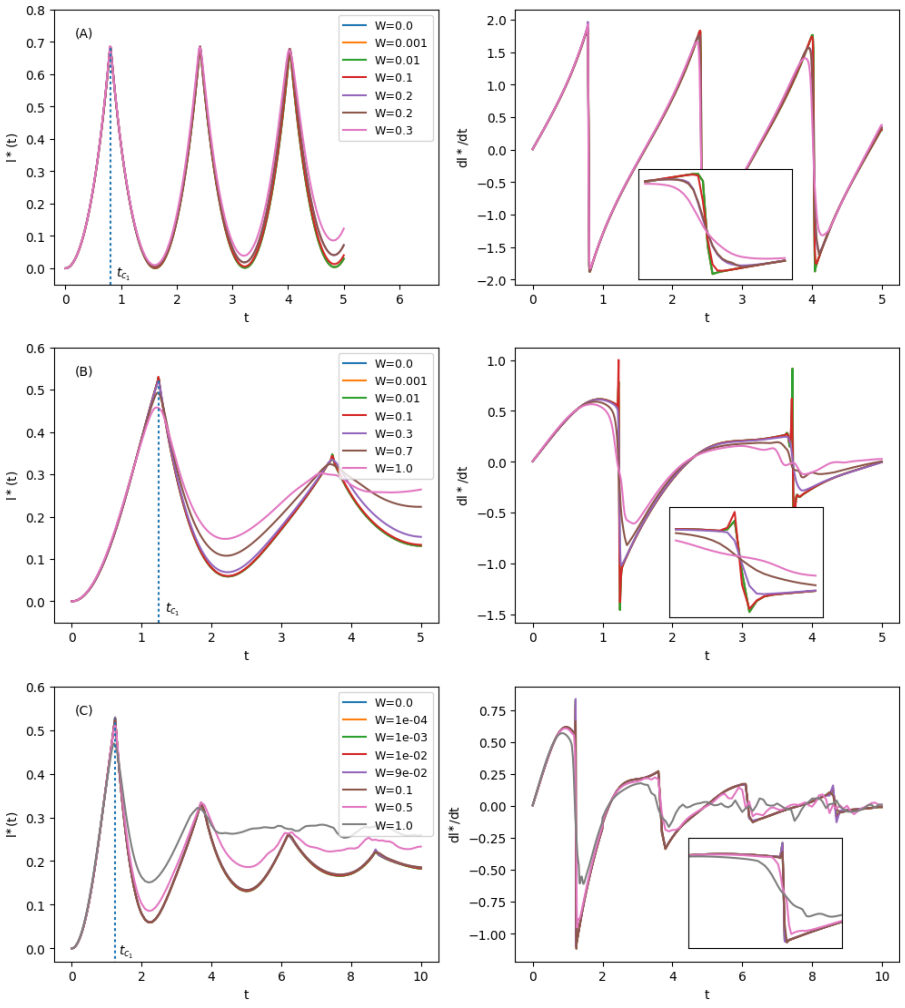

FIGURE 6.9: Disorder-averaged return rates (left), and the corresponding derivatives dl^*/dt of the DARRs (right), for the non-interacting disordered SSH model with PBC. (A) System sites $L = 300$ and symmetric quench $|\delta| = 0.95$. (B) $L = 300$ and $|\delta| = 0.5$. (C) $L = 800$ and $|\delta| = 0.5$. Insets: Zoom-in of the first DPT. The results are averaged over 500 samples.

In summary, we have investigated the dynamical phase transitions for the non-interacting disordered SSH model in various cases (A.I.)-(A.IV.). The weak disorder regimes are summarized in Table 6.1. There are two key messages to take away from this model. First, the time scale at which the first DPT takes place solely depends on the dimerization δ for systems with either OBC or PBC. As shown in Table (6.1), for systems with PBC and symmetric quench $|\delta| = 0.5$, the time scales take place at 1.24 for both systems sites $L = 300$ and $L = 800$. Another example is for systems with OBC quenching from $\delta = -0.5$ into $\delta = +0.5$, and the time scales take place at 2.669 for both systems sites $L = 60$ and $L = 800$. Secondly, the localization length for systems with OBC is different from systems with PBC. Due to the nature of PBC, the localization length of the system ξ_{loc} is much longer than the system size L, so the disorder strength quickly converges to $W = 0.1$ for all system size $L < \xi_{loc}$. This can be ascribed to $\xi_{loc} \propto W^2$. Due to the edge states present in systems with OBC, the system is very susceptible to disorder. The weak disorder regime is very small, and it decreases as we increase the system size L. We can say that the localization length is approximately the same as the system size: $\xi_{loc} \approx L$, and single-particle states become localized for the slightest disorder. The relation $\xi_{loc} \propto W^2$ no longer holds for this case, but looking for an analytical solution of the localization length is out of the scope in this project.

Non-interacting Disordered SSH Model			Weak Disorder	Time Scale
System	Sites L	Quench Direction δ	Regime $[-W, W]$	t_{c_1}
OBC	18	$\delta : -0.95 \rightarrow +0.95$	1×10^{-8}	1.647
	60	$\delta : -0.50 \rightarrow +0.50$	1×10^{-8}	2.669
	180	$\delta : -0.15 \rightarrow +0.15$	1×10^{-7}	7.186
	800	$\delta : -0.50 \rightarrow +0.50$	1.67×10^{-128}	2.669
	60	$\delta : +0.95 \rightarrow -0.95$	0.01	0.81
	60	$\delta : +0.50 \rightarrow -0.50$	1×10^{-15}	1.22
PBC	300	$\lvert\delta\rvert = 0.95$	0.01	0.81
	300	$\lvert\delta\rvert = 0.50$	0.01	1.24
	800	$\lvert\delta\rvert = 0.50$	0.01	1.24

TABLE 6.1: Summary of the weakly disordered regime for the non-interacting disordered SSH model.

6.1.3 The Interacting Disordered SSH Model

We now turn to the disordered interacting SSH model and investigate the dynamical phase transitions. The many-particle Hamiltonian (MPH) is given by Eq. (6.6)

$$\hat{H}_{SSH} = J\sum_{j=1}^{L}[(1+\delta e^{i\pi j})\hat{c}_j^{\dagger}\hat{c}_{j+1} + h.c.] + \sum_j \mu_j \hat{c}_j^{\dagger}\hat{c}_j + \triangle \sum_{j=1}^{L}\left(\hat{n}_j\hat{n}_{j+1} - \frac{1}{4}\right).$$

In the many-particle system, the energy eigenvalue of a single particle depends on the energies of all other particles due to interactions, so strictly speaking a single-particle picture does not exist anymore. In the absence of interactions, however, the energy eigenvalue of a many-particle state in the Fock space can be taken as the sum of the eigenvalues of single particles in real space for the semi-finite chain. For instance, the eigen-energy of the ground state $\lambda_{GS} = \sum_{k=1}^{L/2}\epsilon_k$, where ϵ_k is the eigen-energy of the single particle in the real space. Depending on the situation, the eigen-energy of a many-particle state is either unique or many-fold degenerate. Edge states are present in the topological non-trivial phase, and their eigenvalues can be numerically resolved depending on the value of the dimerization δ and the system size L. Fig. 6.10 shows eigen-energy of the non-interacting ($\triangle = 0$) many-particle states (6.6) with system sites $L = 6$ in the topological non-trivial phase $\delta = +0.95$. The ground state is two-fold degenerate as the consequence of the existence of edge states with zero energy. Consider two particles at energy-eigenvalue $\epsilon = -2$. The third particle can go in either of the two zero energy states, so that the ground state with 3 particles has energy $\lambda_{GS} = -4$ and is two-fold degenerate. Alternatively, one can look at the entanglement spectrum of the interacting many-particle SSH model, which changes upon considering the

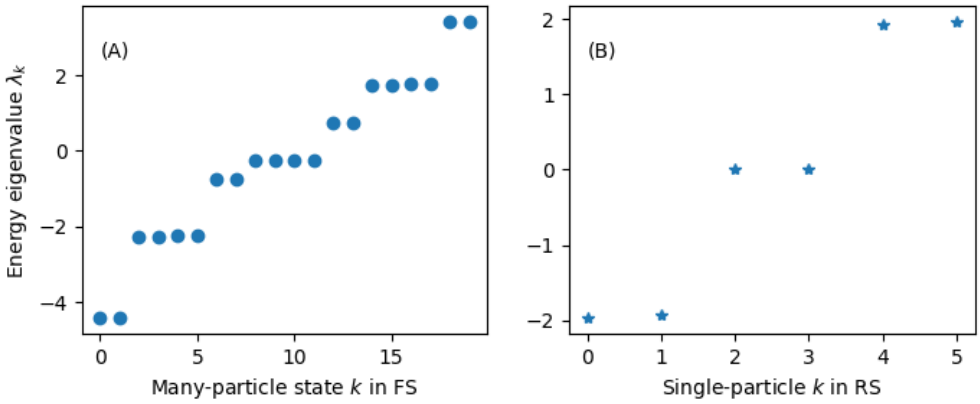

FIGURE 6.10: The energy eigenvalues of many-particle states residing in the Fock space in (A), and of single-particles residing in the real space in (B). The system has 6 system sites.

nearest-neighbour interaction [12].

The major computational challenge in calculating the Loschmidt echo for interacting systems with large system size is the matrix size of the many-particle Hamitonian. Because the Hamiltonian involves nearest-neighbour interactions, it can no longer be expressed in the bilinear form. Evaluating the many-particle Hamiltonian (MPH) with large system size, such as $L = 800$, is basically impossible due to the size of the Hamiltonian, which requires an enormous amount of computational memory. In a single-particle Hamiltonian with system sites $L = 14$, for instance, there are 14 single-particle states, each occupying a single site and leaving 13 other sites empty. The Hamiltonian matrix is 14×14. However, because interacting particles live in Fock space, where there are 2^N possibilities, particles will be distributed permutatively. In the case of system sites $L = 14$ with 7 particles and 7 holes, there are $\frac{14!}{7!\cdot 7!} = 3432$ distinct many-particle states. The matrix of the many-particle Hamiltonian, therefore, has the system size of the square of distinct many-particle states, and it is 3432×3432 in our case. Each unit in a

computation matrix takes 8 Bytes in the double precision float (float64), so the total memory for the MPH of $L = 14$ system sites is $3432 \times 3432 \times 8 \approx 9.2 \times 10^6$ Bytes or 94.2 Megabytes. Calculating the LE with this Hamiltonian matrix takes much longer than calculating the LE for the single-particle Hamiltonian, where the size is only $14 \times 14 \times 8 = 1568$ bytes. Therefore, we restrict ourselves to small size systems for critical systems.

We calculate the LE for the critical disordered SSH model using Eq. (6.2),

$$\mathcal{L}(t) = \left| \langle \Psi_0 | \mathbf{U}^\dagger e^{-i\mathbf{D}t} \mathbf{U} | \Psi_0 \rangle \right|^2.$$

Here $|\Psi_0\rangle$ is the many-body ground state of the initial Hamiltonian in the eigenbasis before quenching. $\mathbf{D}$ and $\mathbf{U}$ are the eigenvalues and eigenvectors of the final Hamiltonian after quenching. $\mathbf{U}^\dagger e^{-i\mathbf{D}t}\mathbf{U}$ is the unitary time operator in the eigenbasis. We provide mathematical derivations for both $\mathbf{D}$ and $|\Psi_0\rangle$ in Appendix (A). The python algorithm to calclulate the LE for the MPH is provided in Appendix (C).

The interaction $\triangle$ serves as a parameter in addition to the dimerization δ. To determine which parameters to use for small size systems, we look at different cases with $\triangle$ and δ for the critical SSH model. First of all, we compare the return rates for the clean system ($\triangle = 0$) with different dimerizations for three system sites $L = 12$, 14 and 22 on systems with both OBC and PBC, see Fig. 6.11. For small dimerizations $|\delta| = 0.15$ and $|\delta| = 0.5$, the return rates look completely different from one system size to another, and dynamical phase transitions occur at different critical times in different cases. Only for $|\delta| = 0.95$ do we observe similar, periodic return rates in all three system sizes, so we will quench disordered systems with

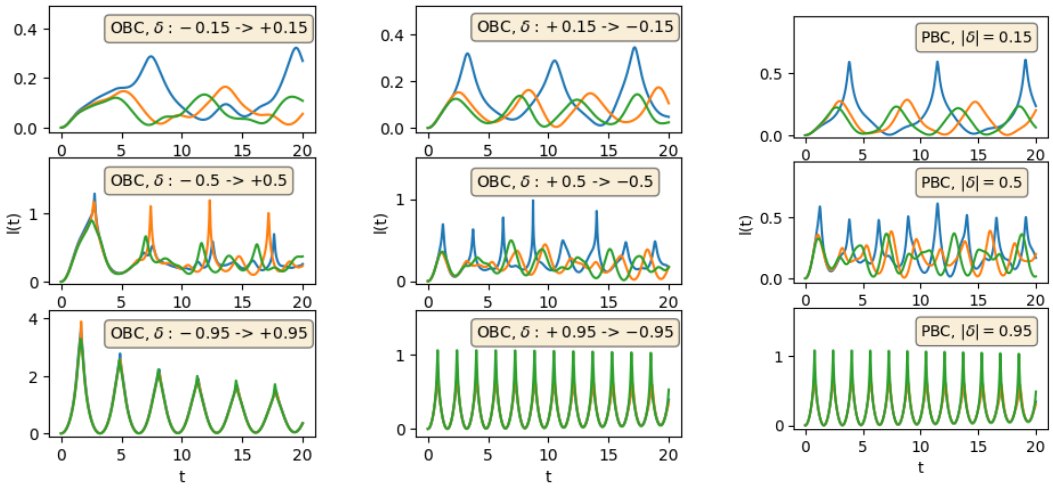

(A) (B) (C)

FIGURE 6.11: Comparisons of the return rates for the clean SSH model with three dimerizations for system sites $L = 12$ (green line), $L = 14$ (orange line) and $L = 22$ (blue line) in absence of interaction, $\triangle = 0$.

dimerization $|\delta| = 0.95$. Since the localization length is not so much different from one to another in small size systems, $L = 12$ suffices to investigate the DPTs.

Secondly, we know that static phase transitions occur in the interacting SSH model (no disorder) as the interaction strength $\triangle$ varies with the dimerization δ [12]. There is a transition line: Below is the topological phase and above is the charge-density wave phase. For instance, the transition line is at $\triangle \approx 7$ with $|\delta| = 0.95$, see Fig. 6.12. Hence, we can investigate dynamical phase transitions for the interacting system with different interaction strengths $\triangle$ for $|\delta| = 0.95$. Since the SSH model with OBC has edge states, which is absent from the system with PBC, we look at return rates for systems with both OBC and PBC. We can also look at two kinds of systems: (i) one in which we can fix the interaction before and after the quench, and (ii) another in which we quench from the non-interacting system $\triangle = 0$ to a the interacting system with given $\triangle$. Fig. 6.13 shows the return

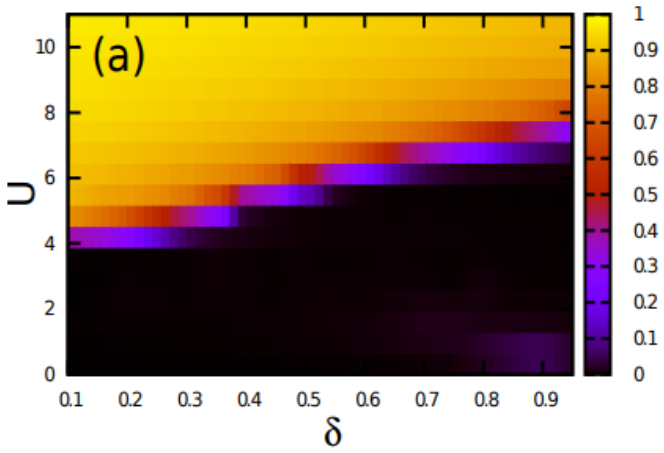

FIGURE 6.12: Static phase transitions in the interacting SSH model. **U** is the interaction strength. Figure taken from [12] (Copyright obtained).

rates for interacting SSH systems with OBC. For small interactions $\triangle = 0.01$ and 0.1, the return rates look almost identical to one another in cases where (i) we fix $\triangle$ before and after the quench and (ii) quench from 0 to $\triangle$. For $\triangle = 0.01$, they show periodicity and the cusps indicate DPTs; whereas there is only one cusp in the return rate for $\triangle = 0.1$. For strong interactions, the return rates look different from one another. The same observations can be seen for systems with PBC, see Fig. 6.14. The return rates for systems with PBC show periodicity, and they show more cusps for the system in which we quench across the sharp phase transition $\triangle = 7.0$, as shown in (D). Therefore, we will investigate the DPTs by evaluating the disorder-averaged Loschmidt echo for the interacting disordered SSH model with system sites $L = 12$ and the following setting:

B.I. OBC, system with fixed interaction $\triangle$ and sytem quenching from $\delta = -0.95$ into $\delta = +0.95$;

B.II. OBC, system with interaction $\triangle$ that varies, and system quenching from $\delta = -0.95$ into $\delta = +0.95$;

B.III. PBC, system with fixed interaction $\triangle$ and symmetric quench $|\delta| = 0.95$;

B.IV. PBC, system with interaction $\triangle$ that varies, and symmetric quench $|\delta| = 0.95$;

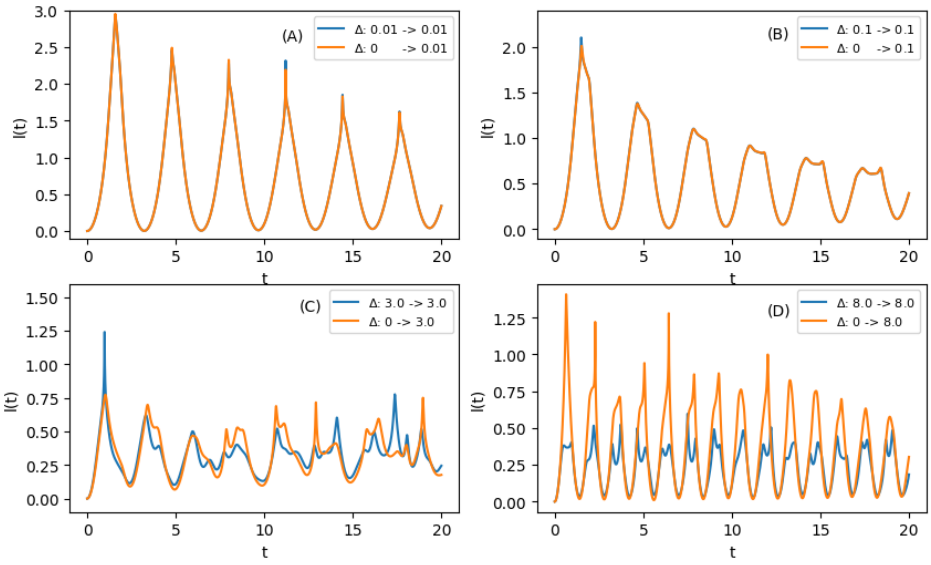

FIGURE 6.13: Return rates for the interacting SSH model with system sites $L = 12$ and OBC. Blue line: the interaction strength $\triangle$ is fixed before and after the quench. Orange line: $\triangle$ is quenched from 0 to a later value.

To begin with, we investigage DPTs for systems with OBC. We look at the disorder-averaged return rates (DARRs, $l^*(t)$) for the first case in the setting B.I., see Fig. 6.15. To identify the weakly disordered regime, we look for complete overlaps in the DARRs and sharp cusps of DPTs for different disorder parameters W. For $\triangle = 0.01$, the weakly disordered regime is for $W \leq 1 \times 10^{-4}$, as the DARR is identical to that for the interacting system without disorder. For $\triangle = 0.1$, the weakly disordered regime is for $W \leq 1 \times 10^{-3}$. For $\triangle = 0.01$, the weakly disordered regime is for $W \leq 1 \times 10^{-3}$. For $\triangle = 3.0$, the weakly disordered regime is for $W \leq 0.01$. For $\triangle = 8.0$, the weakly disordered regime is for $W \leq 0.01$.

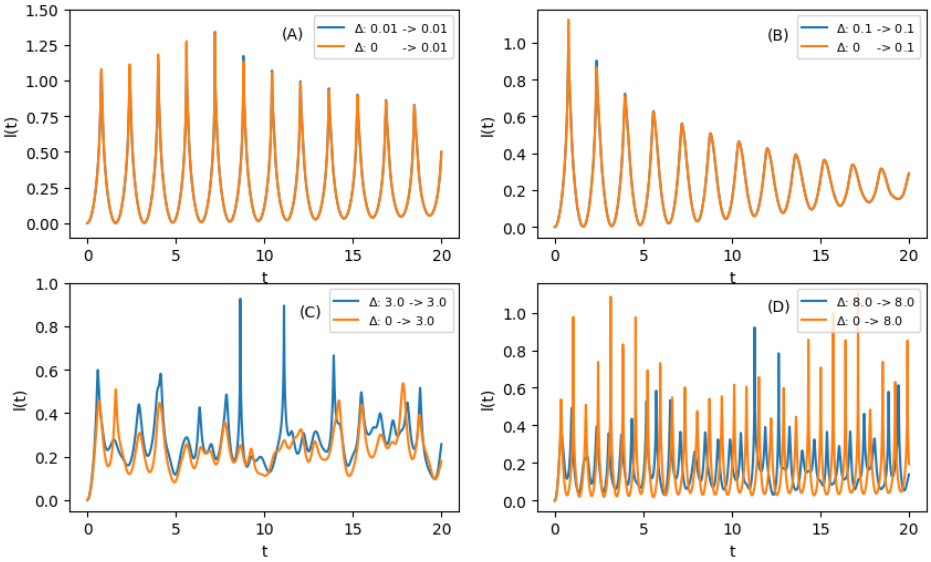

FIGURE 6.14: Return rates for the interacting SSH model with system sites $L = 12$ and PBC. Blue line: the interaction strength $\triangle$ is fixed before and after the quench. Orange line: $\triangle$ is quenched from 0 to a later value.

Since systems with OBC are sensitive due to the presence of edge states, the regime outside the weakly disordered regime is the strongly disordered regime, where the cusps become smooth and dynamical phase transitions disappear. The DARRs show periodic wave forms in weak interacting systems (A) and (B) for $W = 1.0$, while they become almost flat in strong interacting systems (C) and (D) for $W = 5.0$. The same can be said for the second case B.II., where we quench $\triangle$ from 0 to $\triangle$, see Fig. 6.16. The exception is that for strong interacting system (D), the DARR also shows periodicity for $W = 1.0$.

We now turn our attention to systems with PBC. We look at the disorder-averaged return rates for the third case B.III., see Fig. 6.17. We see that the DARRs overlap with one another in all cases of interaction strengths for $W \leq 0.01$, which marks the weak disorder regime. In the disordered regime $0.01 \leq W \leq 0.1$, the DARRs still look close to those in the weakly disordered regime; DPTs are still

present for shorter time durations (i.e. $t < 10$) in weak interacting systems (A) and (B). The amplitude of the return rate for $W = 1.0$ decreases as we increase the interaction strength $\triangle$, but the amplitude of the DARRs for $W = 5.0$ remain the same for all $\triangle$ considered. The DARRs for $W = 5.0$ in the weak interacting systems show periodicity. For systems with strong interaction $\triangle = 8.0$, the DARRs with $W = 1.0$ and $W = 5.0$ become flat after a short time and their amplitudes are close to each other. The system is said to be in the FMBL phase with strong disorder and interaction. Finally, we now turn to the last case B.IV., see Fig. 6.18. Similar to the third case, the weak disorder regime is for $W \leq 0.01$. The DARRs show periodicity for $W = 1.0$ and 5.0 in strong interacting disordered systems (A) and (B), and they become flat for $W = 5.0$ in (C) and (D). Unlike Fig. 6.17 D (case B.III.), the DARR also shows periodicity even for disorder $W = 1.0$ in Fig. 6.18 D. The reason is that as we quench from $\triangle = 0$ to $\triangle = 8$, we should see DPTs for the system without disorder, but here the return rate becomes smooth due to strong disorder $W = 1.0$. The periodicity indicates that the Loschmidt echo cannot decay completely, and the system is in the FMBL phase.

In summary, we have investigated the dynamical phase transitions for the interacting disordered SSH model with system sites $L = 12$. We have included considerations for systems with OBC, PBC, fixed interaction and quenched interaction. The weak and strong disorder regimes are summarized in Table 6.2.

Interacting Disordered SSH Model		Weak Disorder Regime $[-W, W]$		Time scale t_{c_1}	
$L = 12$	Int. Str. $\triangle$	Fixed $\triangle$	Quenched $\triangle$	Fixed $\triangle$	Quenched $\triangle$
OBC	0.01	$W = 1 \times 10^{-4}$	$W = 1 \times 10^{-4}$	1.585	2.2
	0.1	$W = 1 \times 10^{-3}$	$W = 1 \times 10^{-3}$	1.495	1.515
	3.0	$W = 0.01$		0.985	1.03
	8.0			2.2	0.645
PBC	0.01	$W = 0.01$		0.8	0.8
	0.1			0.77	0.775
	3.0			0.6	0.67
	8.0			0.955	0.355

TABLE 6.2: Summary of weakly and strongly disordered regimes for the disordered SSH system with nearest-neighbour interactions.

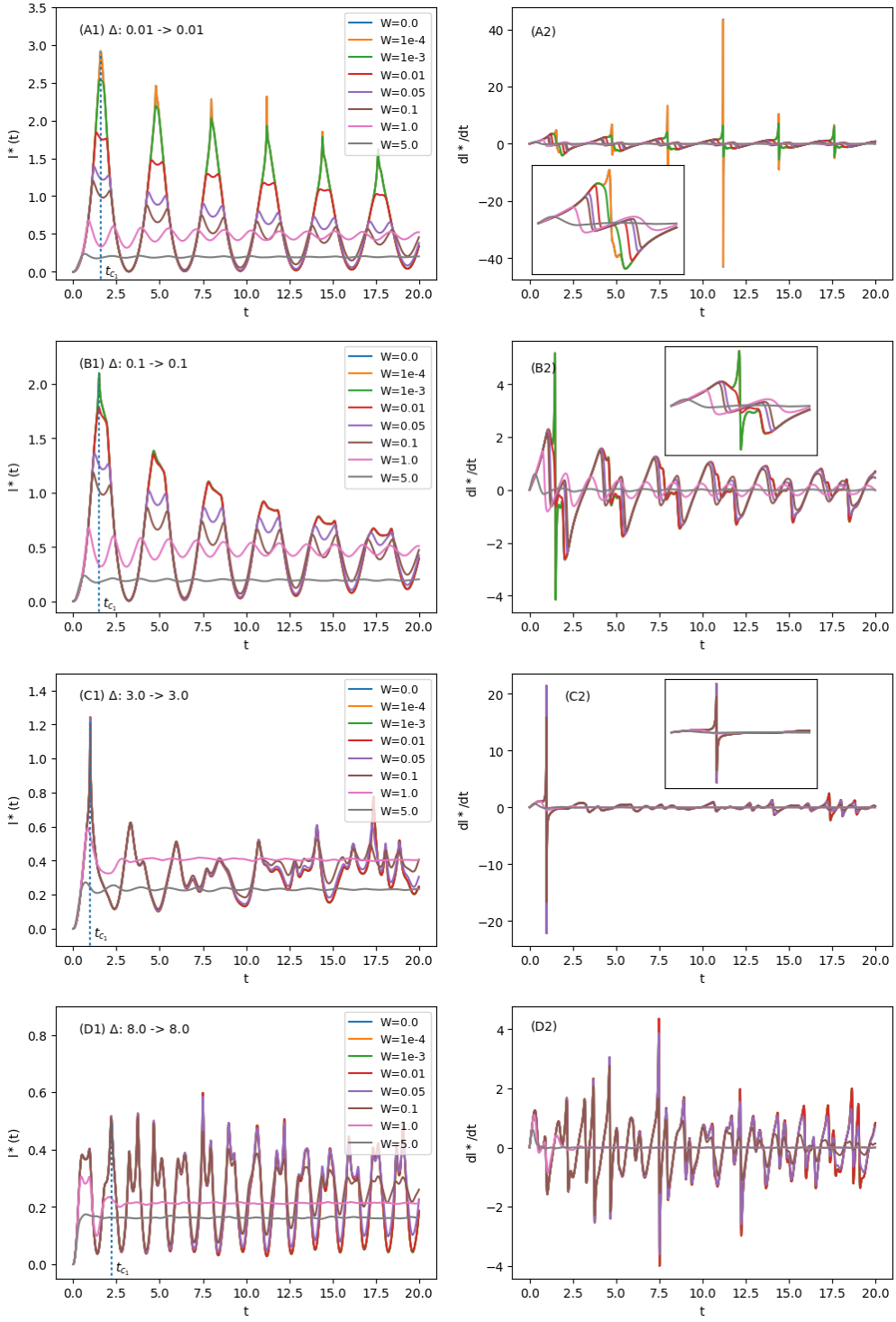

FIGURE 6.15: Disorder-averaged return rates for the interacting disordered SSH model with system sites $L = 12$ and *OBC* (case B.I.). The system is quenched from the trivial phase $\delta = -0.95$ into the topological phase $\delta = +0.95$. The interaction strength is *fixed* before and after the quench.

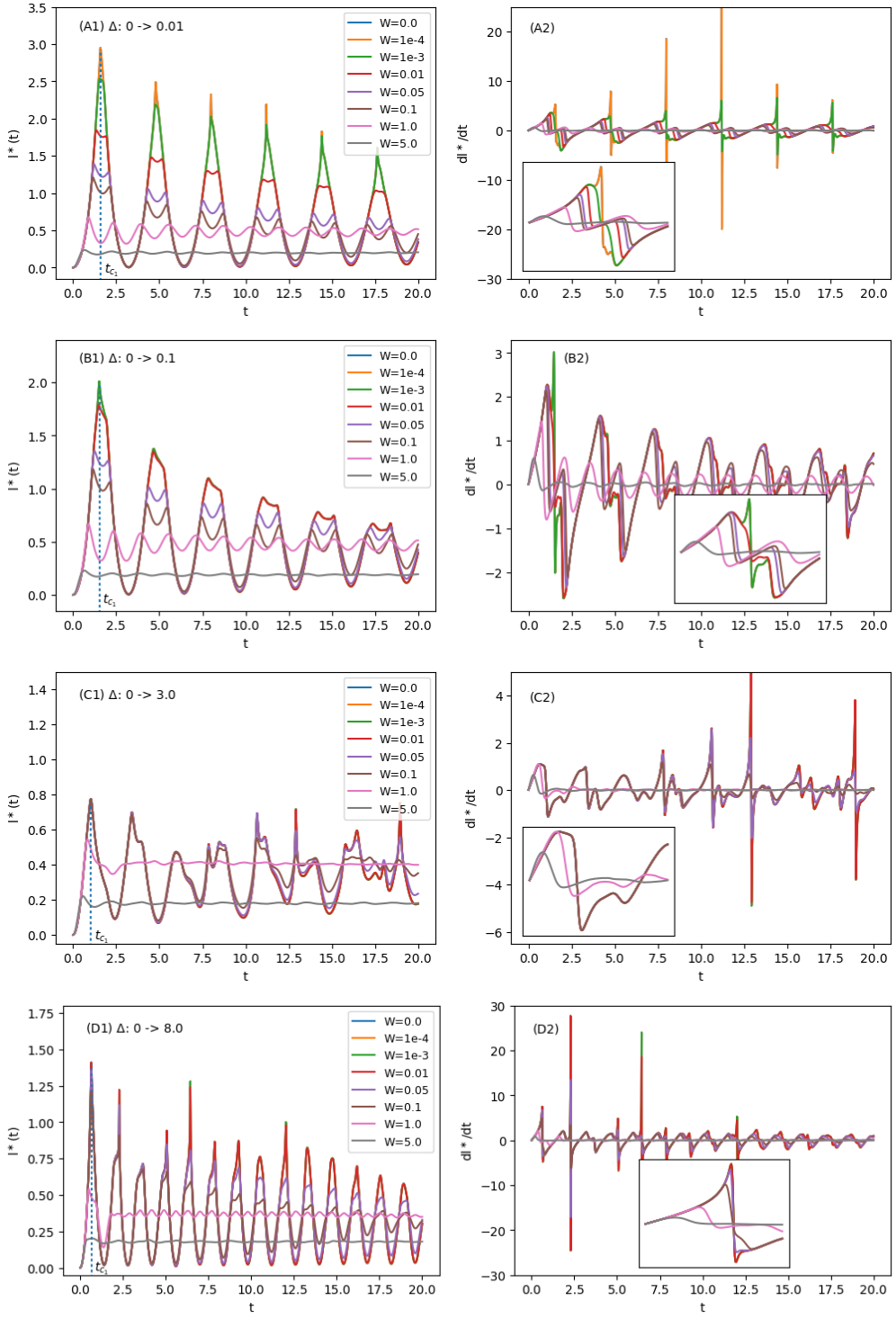

FIGURE 6.16: Disorder-averaged return rates for the interacting disordered SSH model with system sites $L = 12$ and *OBC* (case B.II.). The system is quenched from the trivial phase $\delta = -0.95$ into the topological phase $\delta = +0.95$. The interaction $\triangle$ is *quenched* from 0 into a given value.

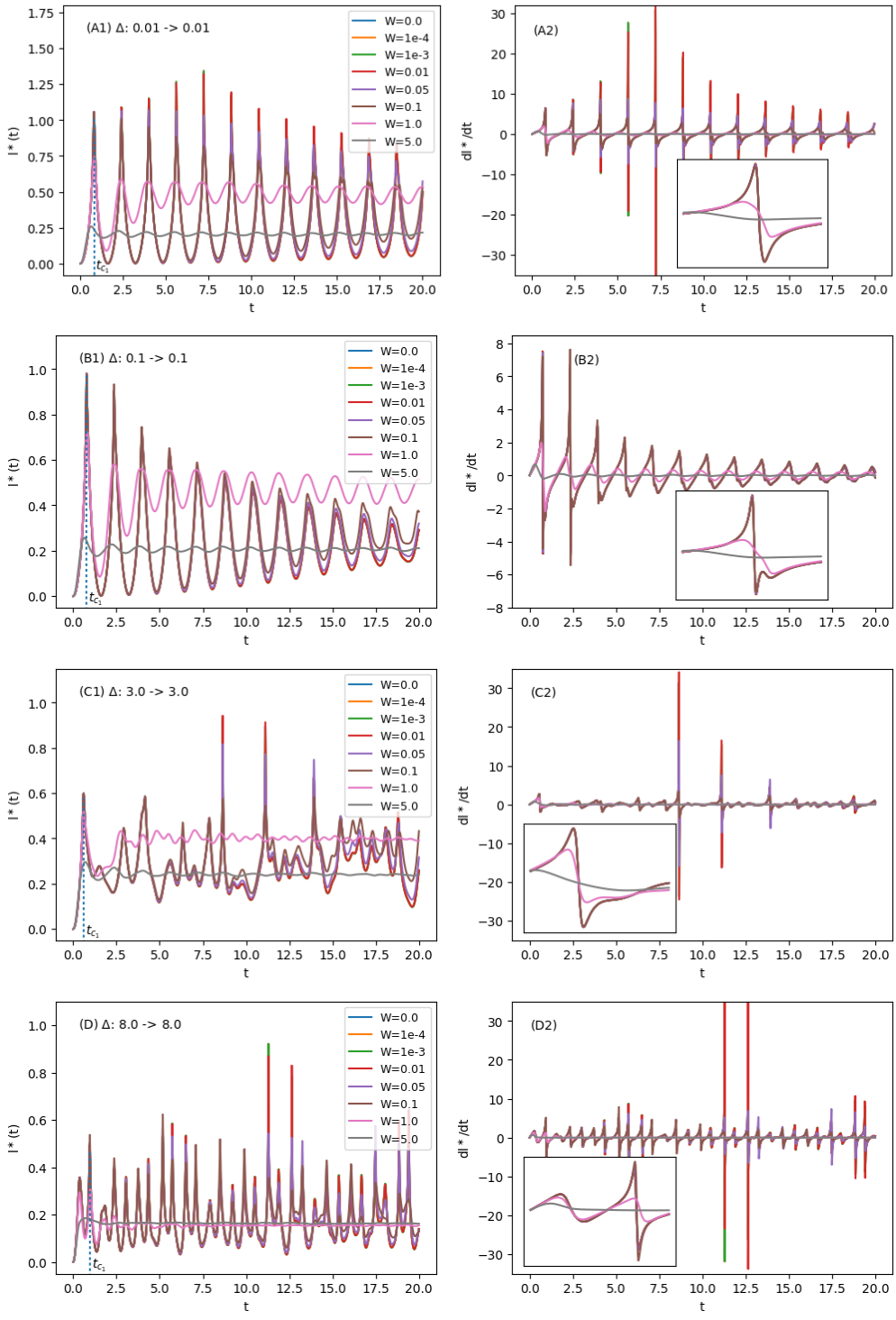

FIGURE 6.17: Disorder-averaged return rates for the interacting disordered SSH model with system sites $L = 12$ and *PBC* (case B.III.). The system is quenched symmetrically $|\delta| = 0.95$. The interaction strength is *fixed* before and after the quench.

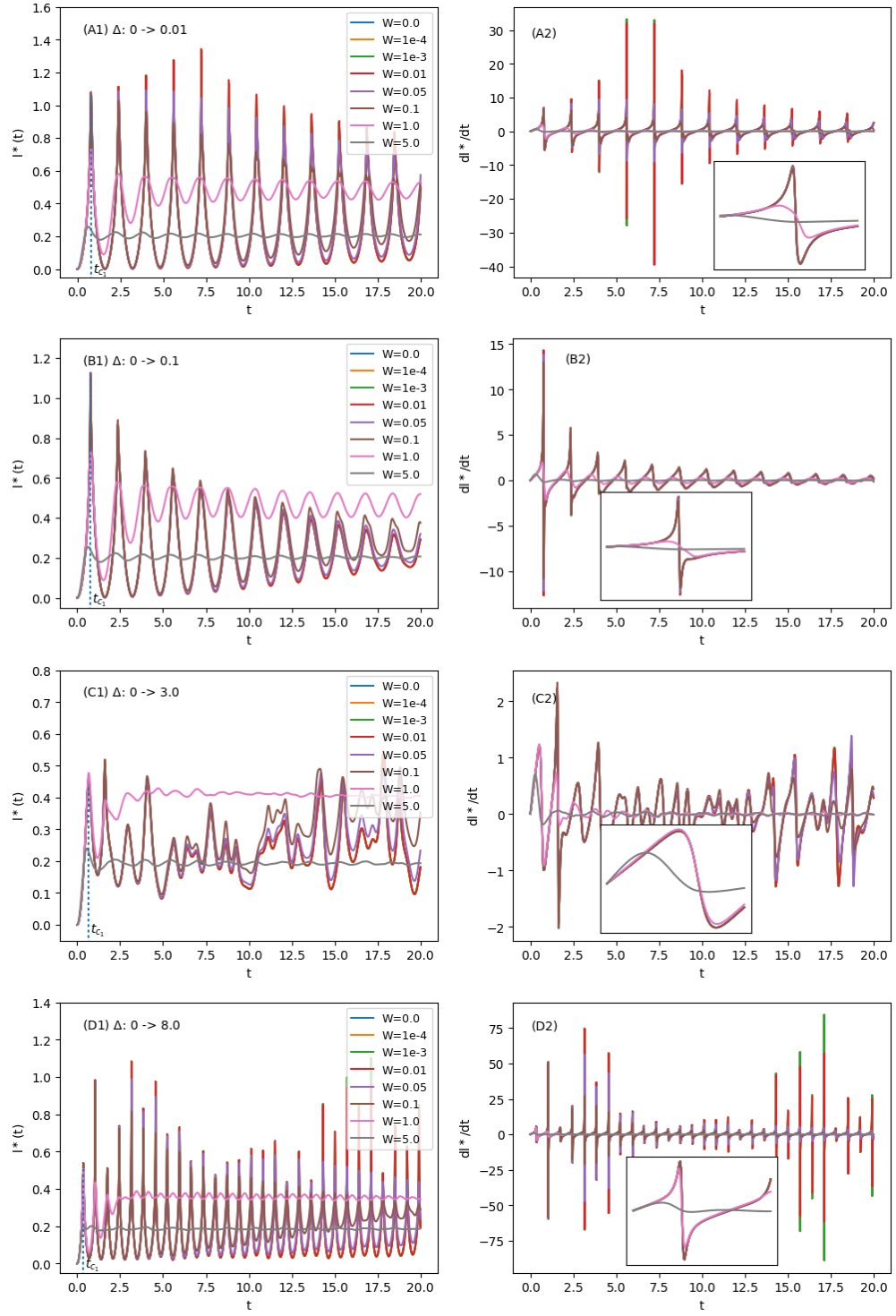

FIGURE 6.18: Disorder-averaged return rates for the interacting disordered SSH model with system sites $L = 12$ and *PBC* (case B.IV.). The system is quenched symmetrically $|\delta| = 0.95$. The interaction $\triangle$ is *quenched* from 0 into a given value.

6.2 The XXZ Model

In this section, we will look at the dynamical phase transitions for both the XX model and the XXZ model with disorder. The many-particle Hamiltonian of the XXZ model with disorder potential has the following form,

$$\hat{H}_{XXZ} = \frac{J}{2}\sum_{j=1}^{L}(\hat{c}_j^\dagger \hat{c}_{j+1} + \hat{c}_{j+1}^\dagger \hat{c}_j) + \sum_{j=1}^{L}\mu_j \hat{c}_j^\dagger \hat{c}_j + \triangle \sum_{j=1}^{L}\left(\hat{n}_j \hat{n}_{j+1} - \frac{1}{4}\right). \tag{6.10}$$

The disordered XX model is a special case of the XXZ model with $\triangle = 0$,

$$\hat{H}_{XX} = \frac{J}{2}\sum_{j=1}^{L}(\hat{c}_j^\dagger \hat{c}_{j+1} + \hat{c}_{j+1}^\dagger \hat{c}_j) + \sum_{j=1}^{L}\mu_j \hat{n}_j. \tag{6.11}$$

6.2.1 The Disordered XX Model

Due to the absence of the nearest-neighbour interaction, the Hamiltonian of the XX model $\hat{H}_{XX}$ is bilinear, and we can calculate the Loschmidt echo using the single-particle Hamiltonian approach. The XX model is different from the SSH model for that there is no edge states in the XX model, and then there are several immediate consquences. First, the eigenvalues are resolved numerically, so the eigenvalue problem is worry-free in systems with OBC or PBC. We are able to evaluate the Loschmidt echo for large size system using Eq. (6.1),

$$\mathcal{L}(t) = |\det(\mathbb{1} - \mathbf{C} + \mathbf{C}e^{-i\mathcal{H}t})|^2.$$

An example of the SPHA is given in Section (5.3). Secondly, due to the absence of the edge states and nearest-neighbour interaction, evaluating the Hamiltonian (6.11) with either PBC or OBC using exact diagonalization for large size systems

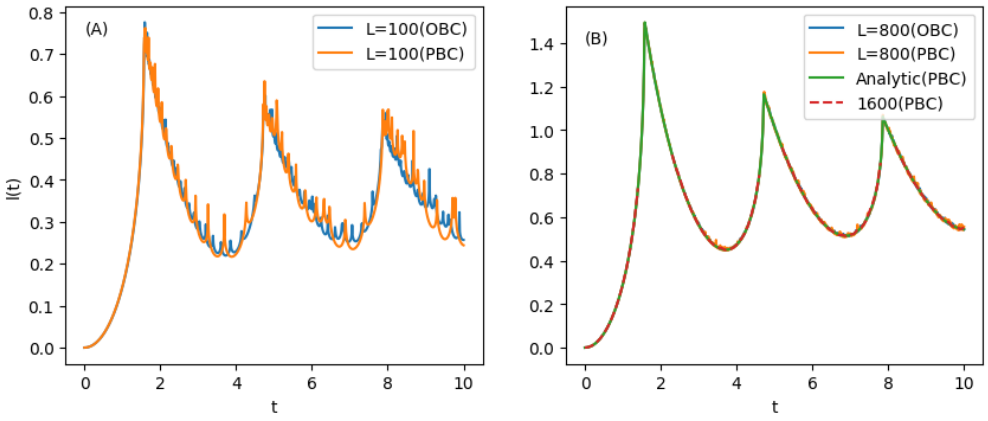

FIGURE 6.19: Comparisons of the return rates for the XX model for small and large size systems. (A) System with sites $L = 100$ in both OBC and PBC. (B) System with sites $L = 800$ in both OBC and PBC and the analytical solution. Values are "erased" due to numerical precision limit for $L = 1600$.

would give initimate eigenvalues; hence, calculating the LE would give similar results, see Fig. 6.19. For finite small systems, there are cusps occuring at critical times $t_{\epsilon_{kn}}$ in Eq. (5.16). As we increase the system size to the thermodynamic limit $N \to \infty$, we can evaluate the return rate using the analytical solution (5.15) and the critical times become periodic, $t_c = \pi/2(2m + 1)$ (5.17). Even though $L = 800$ is still finite in system size, the return rate of this finite system is fairly close to the analytical solution $l(t)$. Morever, due to the numerical precision limit, almost-zero-values of the LE are present for larger size systems, such as $L = 1600$. These values are computatinally neglected in the return rate when taking the natural log $\ln \mathcal{L}(t)$, see Fig. 6.19. Hence, we will use system size $L = 800$ to investigate DPTs in disordered systems. The third difference is that the XX or XXZ model are not topological systems, so the dimerization parameter is absent from the models. The interaction strength $\triangle$ is marked as the point of critical phase transition for the spin model, and with this in mind, we are able to quench

back and forth between the Luttinger liquid phase and the antiferromagnet. We are interested in the specific quench direction: from the antiferromagnetic phase ($\triangle \geq 1$) into the Luttinger liquid phase ($\triangle = 0$), where the Hamiltonian $\hat{H}_{XX}$ in (6.11) is disordered. We choose the initial state as the Néel state in the AFM phase. To obtain the disorder-averaged Loschmidt echo, therefore, we use the following setting: system sites $L = 14$ and $L = 800$, a variety choice of disorder parameter W, and 1500 disordered samples.

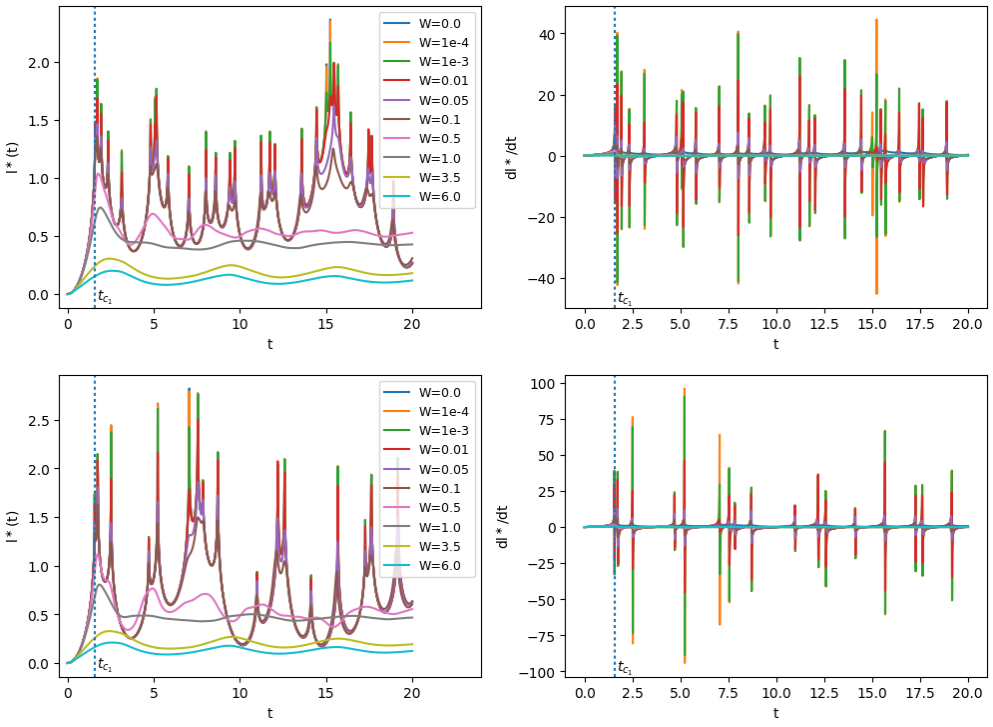

FIGURE 6.20: Disorder-averaged return rates $l^*(t)$ and derivatives dl^*/dt for the XX model with system sites $L = 14$. Top: System with OBC. Bottom: System with PBC. Each result is averaged over 2500 random samples.

We calculate the disorder-averaged return rates $l^*(t)$, and the derivatives dl^*/dt, for the disordered XX model with both small and large systems. For the small size system, we use sites $L = 14$, see Fig. 6.20. The reason that we include this

extra step is for comparing results for the interacting XXZ model with system sites $L = 14$. For disordered XX models with both OBC and PBC, the DPTs for disorder strength $W \leq 1 \times 10^{-3}$ are as sharp across critical times as those for the clean system, so the weak disorder regimes are $W \leq 1 \times 10^{-3}$. The critical time scales are $t_{c_1} = \pi/2$. Then we consider large size system with $L = 800$ sites, see Fig. 6.21. The derivatives $dl^*(t)/dt$ show that the first cusp of the clean system overlap with that for the disordered system for $W \leq 1 \times 10^{-3}$, see (B) of Fig. 6.21. The cusps which appears in derivative plots (6.21) is the result of the critical times $t_{\epsilon_{k_n}}$ (5.16) due to the system size being finite ($L = 800$), see (C) of Fig. 6.21. In the thermodynamic limit, these cusps disappear and the dynamical phase transitions take place at periodic critical times $t_c = \pi/2(2m + 1)$ for $m \in \mathbb{Z}$. The first critical time, or the time scale t_{c_1}, is $\pi/2$. For the disordered XX model with system size $L = 800$, the weak disorder regime is in the disorder potential box $[-W, W]$ for $W \leq 0.001$, where the localization length ξ_{loc} is longer than then system length $L = 800$. With strong enough disorder strength $W > 0.001$, ξ_{loc} is shorter than $L = 800$, the single-particle eigenstates are all localized, and the DPTs are consequently disappeared.

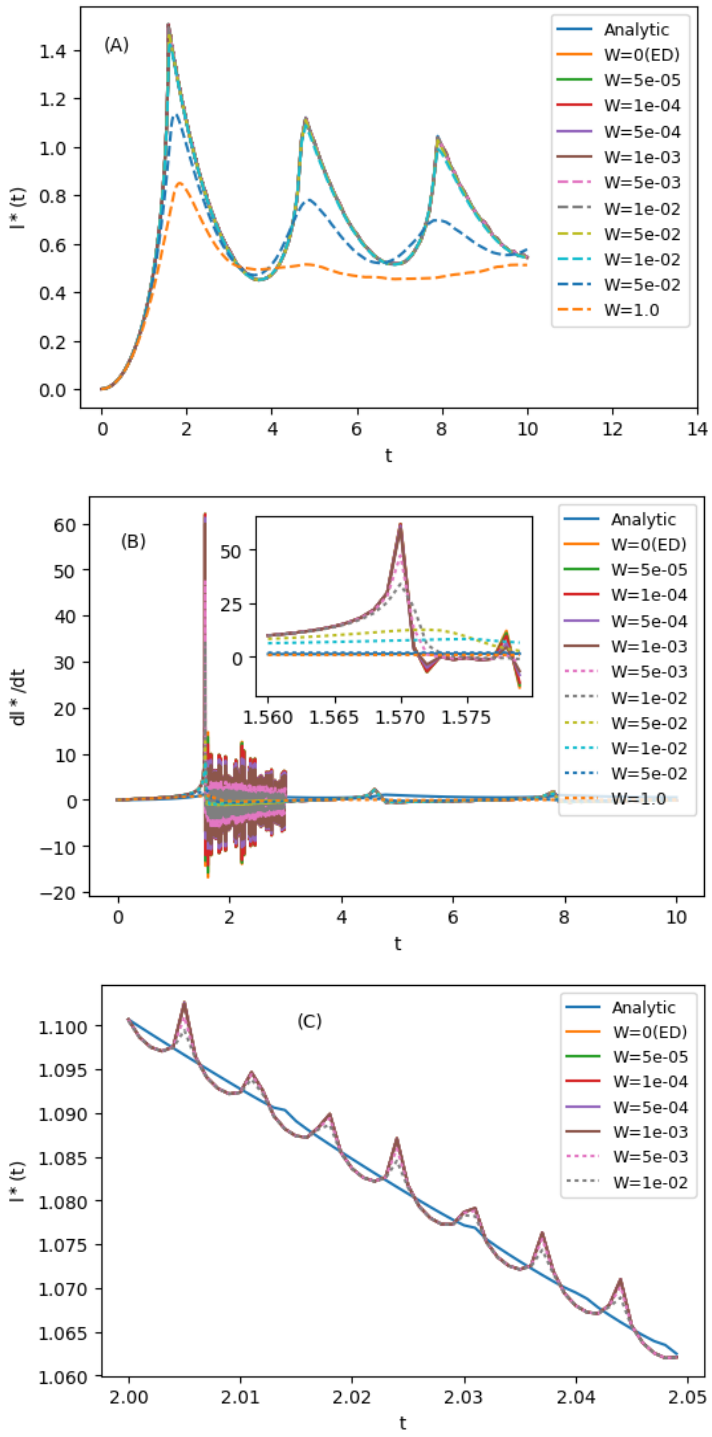

FIGURE 6.21: (A) The disorder-averaged return rates $l^*(t)$ for the disordered XX model. (B) The first time-derivative of DARRs, $dl^*(t)/dt$; inset: enlargement of the first cusp. (C) The DARRs in the small time interval.

6.2.2 The Disordered XXZ Model

We now turn to the disordered XXZ model and investigate the dynamical phase transitions. The many-particle Hamiltonian (MPH) is given by Eq. (6.10),

$$\hat{H}_{XXZ} = \frac{J}{2}\sum_{j=1}^{L}(\hat{c}_j^\dagger \hat{c}_{j+1} + \hat{c}_{j+1}^\dagger \hat{c}_j) + \sum_{j=1}^{L}\mu_j \hat{c}_j^\dagger \hat{c}_j + \triangle \sum_{j=1}^{L}\left(\hat{n}_j \hat{n}_{j+1} - \frac{1}{4}\right),$$

and we evaluate the LE using Eq. (6.2),

$$\mathcal{L}(t) = |\,\langle \Psi_0 | \mathbf{U} e^{-i\mathbf{D}t} \mathbf{U}^\dagger | \Psi_0 \rangle\,|^2.$$

Since there is no analytic solution for the XXZ model, calculating the many-particle Hamiltonian is entirely done by exact diagonalization, see Appendix (C). The clean system is critical for $-2 \leq \triangle \leq 2$, and gapped otherwise. The model (6.10) has been investigated for the spectral properties of the disordered Hamiltonian by RSRG-X in Ref. [145] and by exact diagonalizations in Ref. [146]. The entanglement entropy for this model has been discussed using exact diagonalization and the light-cone renormalization group (LCRG) in Ref. [2]. Here we study the dynamical phase transitions by means of exact diagonalization. We choose $L = 14$ as the system size, because the localization length would not be too much different for slightly larger system size. Evaluating the Hamiltnian matrix would consume too much resources, and calculating the disorder-averaged LE over many random samples take much a longer calculation time. The many-body ground state $|\Psi_0\rangle$ is the Néel state in the eigenbasis. We quench the system within the antiferromagnetic phase from the Néel state for $J\triangle > 0$ across both the weak and strong interactions $\triangle = 1$, 2 and 8.

The disorder-averaged return rates $l^*(t)$ and derivatives for disordered systems with OBC and interaction strengths $\triangle = 1.0$, 2.0 and 8.0 are presented in Fig. 6.22. The dynamical phase transitions for all three cases considered are no longer periodic or predictable. Comparing $l^*(t)$ for systems with $\triangle = 1.0$ and $\triangle = 2.0$, we see that there are fewer DPTs for the system with $\triangle = 2.0$. For the system with $\triangle = 8.0$ and $W \leq 1.0$, the DPTs become periodic, but the amplitudes of $l^*(t)$ are very small in the range $[0, 0.0175]$, see (C) of Fig. 6.22. The derivative plots show that the weak disorder regimes are disorder potential boxes $[-W, W]$ with $W \leq 0.01$ for all systems with $\triangle = 1.0$, 2.0 and 8.0, respectively. As the disorder strength W is increased from 0.1 to 6.0, the amplitudes of $l^*(t)$ are also increased from ≈ 0.011 to inbetween 0.06 and 0.08, see (D). The behaviour of the increased amplitude of $l^*(t)$ for strong interaction and disorder strengths is only present in the XXZ model (absent in the XX model), see Fig. 6.20. The same can be said for the disordered XXZ model with periodic boundary conditions, see Fig. 6.20.

In summary, we have investigated the dynamical phase transitions for the disordered XX and XXZ models. We have included considerations for systems with OBC, PBC, weak and strong nearest-neighbour interaction strengths $\triangle$. The weak and strong disorder regimes are summarized in Table 6.3. The localization length ξ_{loc} for the XXZ (XX) model is much longer than system sites $L = 800$, so that only large enough disorder strength $W > 0.001$ would bring the system into the strongly localized state, where dynamical phase transitions become smooth. The time scales of the first DPT for the XX model is $\pi/2$ regardless of the system size or periodic conditions. Due to the presence of nearest-neigbour interactions, the time scales of the first DPT for the XXZ model are different for different $\triangle \neq 0$.

As shown from Table (6.3), the time scale increases from $\pi/2$ to 9.055 as we increase $\triangle$; however, after a certain interaction threshold $2 \leq \triangle \leq 8$, the return rate shows many DPTs, and the time scale becomes 0.43 for system with OBC and 0.385 for system with PBC. This is because many-particle states are all localized due to strong interactions, and the time evolution of the system would show many dynamical phase transitions of localized states.

Critical Disordered XX & XXZ Models		Weak Disorder Regime $[-W, W]$		Time scale t_{c_1}	
	Int. Str. $\triangle$	$L = 14$	$L = 800$	$L = 14$	$L = 800$
OBC	0.0	$W = 1 \times 10^{-3}$	$W = 1 \times 10^{-3}$	$\pi/2$	$\pi/2$
	1.0	$W = 1 \times 10^{-3}$	N/A	3.095	N/A
	2.0			9.055	
	8.0			0.43	
PBC	0.0	$W = 1 \times 10^{-3}$	$W = 1 \times 10^{-3}$	$\pi/2$	$\pi/2$
	1.0	$W = 1 \times 10^{-3}$	N/A	4.01	N/A
	2.0			8.175	
	8.0			0.385	

TABLE 6.3: Summary of weakly and strongly disordered regimes for the disordered XX and XXZ models.

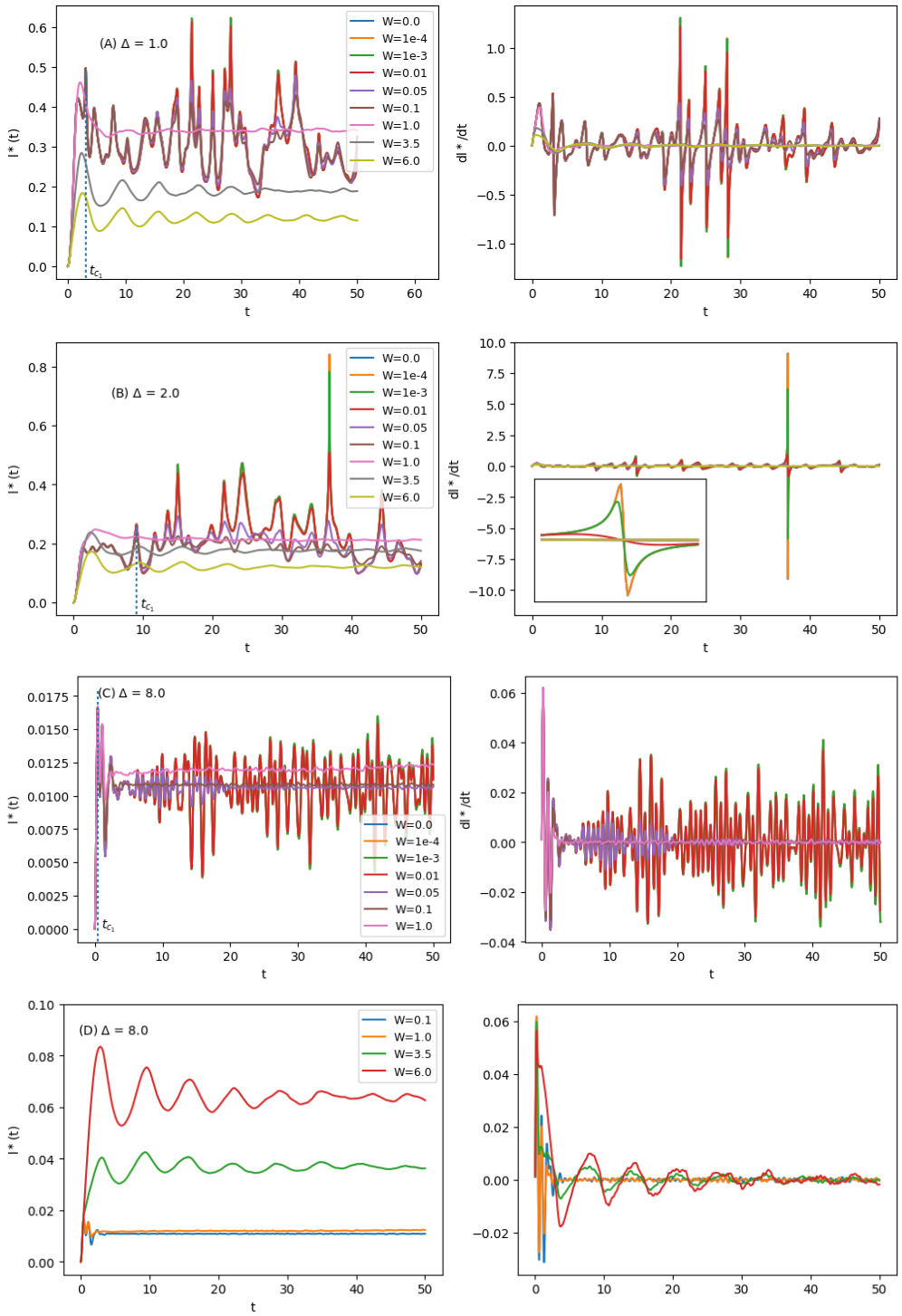

FIGURE 6.22: The disorder-averaged return rates $l^*(t)$ (left) and the derivatives dl^*/dt (right) for the disordered XXZ model with *OBC* and system sites $L = 14$. (A) Interaction strenght $\triangle = 1.0$. (B) $\triangle = 2.0$; inset: zoom-in of the DPT at t_{c_1}. (C) $\triangle = 8.0$ for $W \leq 1.0$. (D) $\triangle = 8.0$ for $W > 1.0$.

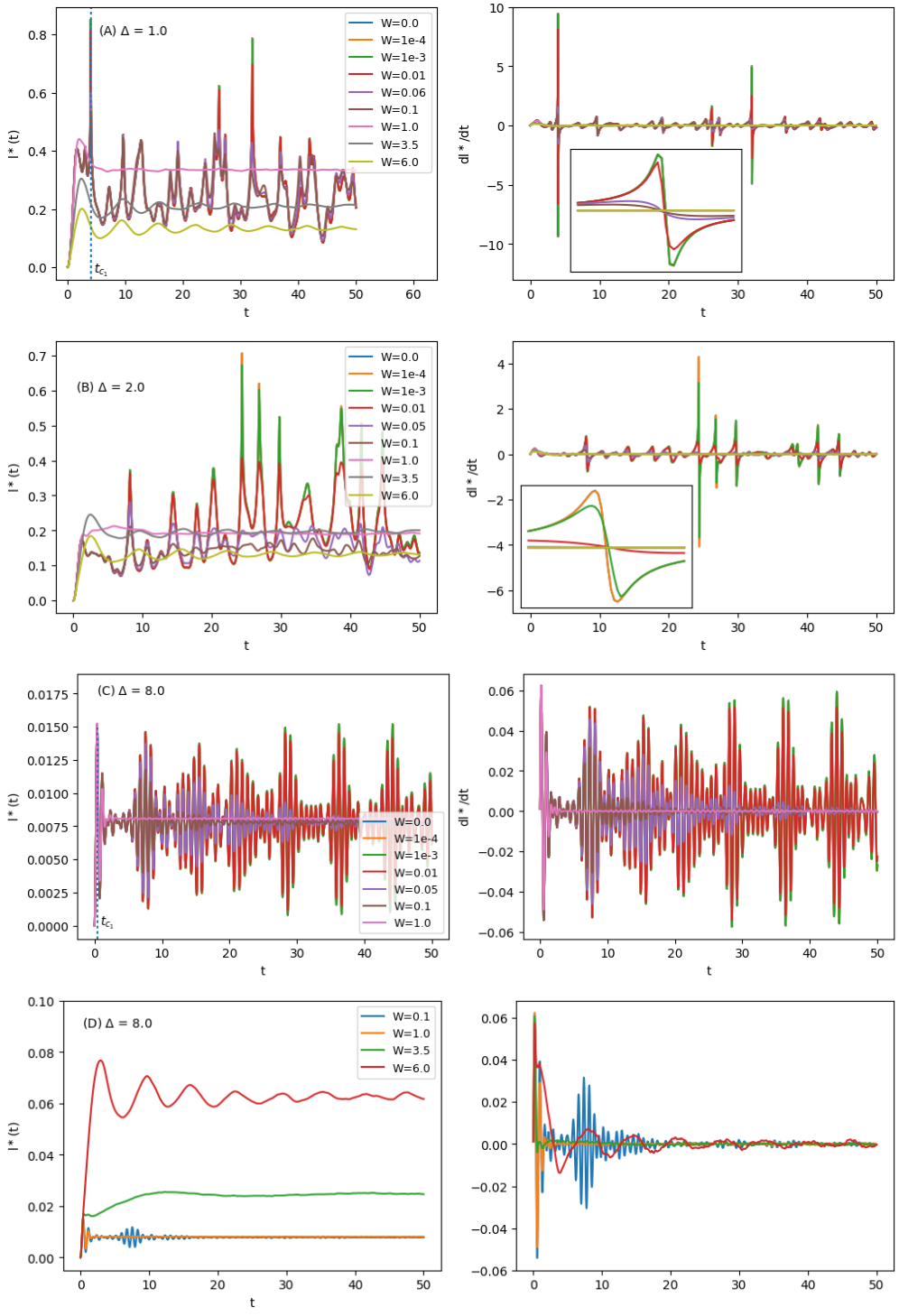

FIGURE 6.23: The disorder-averaged return rates $l^*(t)$ (left) and the derivatives dl^*/dt (right) for the disordered XXZ model with *PBC* and system sites $L = 14$. (A) Interaction strength $\triangle = 1.0$. (B) $\triangle = 2.0$; inset: zoom-in of the DPT at t_{c_1}. (C) $\triangle = 8.0$ for $W \leq 1.0$. (D) $\triangle = 8.0$ for $W > 1.0$.

Chapter 7

Conclusion

In the thermodynamic limit, an interacting disordered many-body quantum system can show a phase transition between an ergodic and a localized phase. When different parts of the Hilbert space are fully explored by energy and particle exchange, the unitary quantum dynamics leads to the thermalization of subsystems. Quantum thermalization is a process of a closed system going into thermal equilibrium, provided that the system is able to act as its own reservoir. In contrast to thermalizing systems, localized systems do not act as reservoirs; the long-time states of subsystems are determined by some local details of the system's initial state. Quantum decoherence in localized systems is the loss of quantum coherence in time, and it is of interest to study the stability of time reversal and dynamical phase transitions with respect to small perturbations in disordered quantum systems.

The Loschmidt echo is the measure of the stability of time reversal. The generalized Loschmidt echo formula $\mathcal{L}(t) = |\langle\Psi_0|\Psi(t)\rangle|^2$ describes the overlap between the initial state $|\Psi_0\rangle$ and the time-evolved state $|\Psi(t)\rangle = e^{-itH}|\Psi_0\rangle$. The zeros of the Loschmidt echo corresponds to dynamical phase transitions (non-analyticities) in the return rate function $l(t)$ in the thermodynamic limit. Although the choice of the initial state of a many-particle interacting system can technically be controlled in experiments, it is convenient to numerically access the initial state from

the many-body eigenstate of the Hamiltonian in the eigenbasis for calculation purposes. For non-interacting systems, the many-particle problem reduces to a single-particle problem, and evaluating large system sizes can be easily achieved with the alternative formula $\mathcal{L}(t) = |\det(\mathbb{1} - \mathbf{C} + \mathbf{C}e^{-i\mathcal{H}t})|^2$. We have described two sets of numerical algorithms by exact diagonalization to calculate the Loschmidt echo for the single-particle and the many-particle problems. Using the non-interacting SSH and the XX models with small system size, we have shown that the two formulae are equivalent in both the clean and the disordered cases. On-site disorder potentials take random values within a boundary box $[-W, W]$, so each disorder-averaged Loschmidt echo for a given disorder parameter W is obtained by taking the averaged value over many disorder configurations.

For a non-interacting one dimensional system with short-range hoppings, it is well-known that even an infinitesimal amount of disorder will lead to a localization of the single-particle wave functions. This phenomena is known as Anderson localization. The localization length is described by the inverse power law of the disorder strength. For a system with finite system size, one expects to see that electron eigenstates are localized if the localization length is shorter than the system size. With this in mind, we attempt to understand several questions in this research. Does the disorder-averaged Loschmidt echo (return rate) show dynamical phase transitions? What is the the time scale at which dynamical phase transitions occur? Can $\mathcal{L}(t)$ decay completely in disordered systems? What is the difference between interacting disordered systems and the non-interacting ones?

In the rest of the thesis, we discussed the above questions with numerical data from the disorder-averaged return rates for the disordered SSH model with and

without nearest-neighbour interactions, the disordered XX model, and the disordered XXZ model in cases where analytical solutions are not available. We have the following conclusion. (1) For systems with finite system sizes, we showed that the disorder-averaged return rates show dynamical phase transitions in weak disorder regimes. For strong disorder strengths, localization lengths are shorter than system sizes, and we showed that return rates become smooth and dynamical phase transitions disappear. (2) The time scales at which non-analyticities occur for systems in weak disorder regimes are summarized in various tables. (3) The Loschmidt echo can decay completely for finite system size in the weak disorder regime. For strongly disordered systems, the Loschmidt echo cannot decay completely even for small system size. (4) The SSH model shows significant difference between interacting disordered systems and non-interacting ones, but the difference between the XX and the XXZ model is not very obvious. We first look at the SSH model. For the non-interacting disordered SSH model in the topological phase, the system is expected to be very susceptible to disorder due to the presence of the edge states. Our results showed that the weak disorder regime $[-W, W]$ is very small with $W \approx \times 10^{-128}$ for system size $L = 800$. For the system in the trivial phase with symmetric quenches, $W = 0.01$. Comparing the non-interacting and the interacting disordered SSH systems, we observed that the weak disorder regimes are smaller in the former case. The value of W increases as we increase the interaction strength $\triangle$, and we found that the weak disorder regimes $[-W, W]$ are the same, $W = 0.01$, for interacting systems with $\triangle \geq 3.0$. This result has a strong implication. Based on the Loschmidt echo, unless we know the time scales of non-analyticities, we have no access to the initial eigenstate of a strongly disordered system because we cannot know if the system is subject to open or periodic

boundary conditions. We now turn to the spin model in which we quench from the Néel state across the antiferromagnetic phase. To begin with, the time scales agree with the analytical solutions for the XX model. Moreover, we showed that the weak disorder regimes for both of these models are the same: $[-W, W]$ with $W = 10^{-3}$. This is in contrary to what we expected to see: the weak disorder regime would be larger in the interacting XXZ model than in the non-interacting XX model. This result has two implications. First, the localization lengths in both systems are the same for the same disorder strength W. Secondly, because of the first implication, one can analytically calculate the localization length for the XX model to determine the localization length for the XXZ model.

In conclusion, we have investigated dynamical phase transitions for the disordered SSH and XXZ models and come to the above conclusion. Not only have our work provided calculation convenience in evaluating both single-particle and many-particle systems, but we have also shown an indirect access to many-body initial state by calculating time scales for disordered systems. For future works related to the two disordered models, one can prepare the systems in an randomized initial state and study the dynamics. As a powerful tool to indirectly measure dynamical phase transitions, the Loschmidt echo can be applied to many strongly-correlated quantum systems. Meanwhile, the Loschmidt echo can be indirectly used to determine the system's susceptibility to disorder and distinguish weakly and strongly disorder regimes. Quantum decoherence due to disorder is the loss of information in localized systems, and how much information can be retained in the initial state matters for quantum computing. Hence, one can learn how much information can be preserved in the initial state under unitary quantum dynamics by investigating the dynamical many-body correlated functions for disordered systems.

Appendix A

Mathematical Derivations

We provide a rigorous proof to show that Equations (5.9) and (5.2) are mathematically equivalent. First, we will provide an expression for the two-point correlation matrix $\mathbf{C} = \langle \Psi_i^\dagger \Psi_j \rangle$ in the eigenbasis. Secondly, we provide a convenient method to evaluate the exponential term $e^{-i\mathcal{H}t}$. Finally, we show that Eq. (5.10) is true. The Hamiltonian that we consider here represents single-particle states and is bilinear and hermitian.

A.1 Correlation Matrix C in Eigenbasis

To change from the general basis to eigenbasis of the initial Hamiltonian H_i before quenching, it is sufficient to express$\{c_k, c_k^\dagger\}$ in terms of the normal mode operators $\{\eta_k, \eta_k^\dagger\}$ which diagonalize H_i,

$$\eta_k = \sum_i \left[\frac{\phi_{k,i} + \psi_{k,i}}{2} c_i + \frac{\phi_{k,i} - \psi_{k,i}}{2} c_i^\dagger \right], \tag{A.1}$$

$$\eta_k^\dagger = \sum_i \left[\frac{\phi_{k,i} + \psi_{k,i}}{2} c_i^\dagger + \frac{\phi_{k,i} - \psi_{k,i}}{2} c_i \right], \tag{A.2}$$

where $\phi_{k,i}$ and $\psi_{k,i}$ satisfy the following coupled linear equations

$$\vec{\phi}_k(\mathbf{A}-\mathbf{B}) = E_k\vec{\psi}_k,$$
$$\vec{\psi}_k(\mathbf{A}+\mathbf{B}) = E_k\vec{\phi}_k,$$

whose solution permits to find the eigenbasis of the Hamiltonian in Eq. (5.6) ([140]). Due to the fact that $\mathbf{A}$ is symmetric and $\mathbf{B}$ is antisymmetric, the set of all eigenvalues E_k's are real, and we can choose all the ϕ_k's and ψ_k's to be real and orthonormal.

To find the canonical relations, we can define the following variables

$$g_{k,i} = \frac{1}{2}(\phi_{k,i}+\psi_{k,i}), \tag{A.3}$$
$$h_{k,i} = \frac{1}{2}(\phi_{k,i}-\psi_{k,i}). \tag{A.4}$$

For a given index i, the following relations hold

$$\begin{aligned} g_k g_{k'} + h_k h_{k'} &= \frac{1}{2}(\phi_k+\psi_k)\frac{1}{2}(\phi_{k'}+\psi_{k'}) \\ &\quad + \frac{1}{2}(\phi_k-\psi_k)\frac{1}{2}(\phi_{k'}-\psi_{k'}) \\ &= \frac{1}{4}(\phi_k\phi_{k'}+\phi_k\psi_{k'}+\phi_{k'}\psi_k+\psi_k\psi_{k'}) \\ &\quad + \frac{1}{4}(\phi_k\phi_{k'}-\phi_k\psi_{k'}-\phi_{k'}\psi_k+\psi_k\psi_{k'}) \\ &= \frac{1}{2}(\phi_k\phi_{k'}+\psi_k\psi_{k'}) \\ &= \delta_{k,k'} \end{aligned}$$

$$\begin{aligned} g_k h_{k'} - g_{k'} h_k &= \frac{1}{2}(\phi_k + \psi_k)\frac{1}{2}(\phi_{k'} - \psi_{k'}) \\ &\quad - \frac{1}{2}(\phi_{k'} + \psi_{k'})\frac{1}{2}(\phi_k - \psi_k) \\ &= \frac{1}{4}(\phi_k\phi_{k'} - \phi_k\psi_{k'} + \phi_{k'}\psi_k - \psi_k\psi_{k'}) \\ &\quad - \frac{1}{4}(\phi_{k'}\phi_k - \phi_{k'}\psi_k + \phi_k\psi_{k'} - \psi_{k'}\psi_k) \\ &= 0 \end{aligned}$$

The two canonical relations are then immediately expressed as

$$\begin{aligned} \sum_i (g_{k,i} g_{k',i} + h_{k,i} h_{k',i}) &= \delta_{k,k'} \\ \sum_i (g_{k,i} h_{k',i} - g_{k,i} h_{k',i}) &= 0, \end{aligned}$$

which serve as the necessary and sufficient condition that $\{\eta_k, \eta_k^\dagger\}$ be canonical Fermionic operators with $\mathbf{g}\mathbf{g}^\mathbf{T} + \mathbf{h}\mathbf{h}^\mathbf{T} = \mathbb{1}$ and $\mathbf{g}\mathbf{h}^\mathbf{T} - \mathbf{h}\mathbf{g}^\mathbf{T} = 0$ being the imposed constraints.

Equations (A.1) and (A.2) can be expressed using g_{k_i} and $h_{k,i}$ as

$$\begin{aligned} \eta_k &= \sum_i \left[g_{k,i} c_i + h_{k,i} c_i^\dagger \right], \\ \eta_k^\dagger &= \sum_i \left[g_{k,i} c_i^\dagger + h_{k,i} c_i \right], \end{aligned}$$

We can write the above equations in the compact vector form,

$$\hat{\eta} = \mathbf{g} \cdot c + \mathbf{h} \cdot c^{\dagger}, \tag{A.5}$$

$$\hat{\eta}^{\dagger} = \mathbf{g} \cdot c^{\dagger} + \mathbf{h} \cdot c. \tag{A.6}$$

By inverting the above Equations (A.5) and (A.6), we can express the fermionic operators $\{c_k, c_k^{\dagger}\}$ in the compact matrix form

$$c = \mathbf{g^T} \cdot \eta + \mathbf{h^T} \cdot \eta^{\dagger}, \tag{A.7}$$

$$c^{\dagger} = \mathbf{g^T} \cdot \eta^{\dagger} + \mathbf{h^T} \cdot \eta, \tag{A.8}$$

Substituting Equations (A.7) and (A.8) into the correlation matrix $\mathbf{C}$, we can express the correlation matrix $\mathbf{C}$ in the eigenbasis as

$$\mathbf{C} = \begin{pmatrix} \mathbf{h^T h} & \mathbf{h^T g} \\ \mathbf{g^T h} & \mathbf{g^T g} \end{pmatrix}.$$

In absence of pair creation or annhilation, the off-diagonal elements are all zero, and $\mathbf{h^T h} = \mathbb{1} - \mathbf{g^T g}$, and we have obtained correlation matrix $\mathbf{C}$ in the eigenbasis

$$\mathbf{C} = \begin{pmatrix} \mathbf{h^T h} & 0 \\ 0 & \mathbf{g^T g} \end{pmatrix}. \tag{A.9}$$

A.2 The Exponential $e^{-i\mathcal{H}t}$

We provide a method for the evalution of the exponential term in the formula $e^{-i\mathcal{H}t}$, where $\mathcal{H}$ is the matrix elements of the final Hamiltonian H. It is important

to distinguish the initial and final Hamiltonians in the following calculations. We introduce the vector $\mathbf{\Gamma}^\dagger = (\eta_1^\dagger \dots \eta_N^\dagger, \eta_1 \dots \eta_N)$, where η_k is the normal mode operator that diagnoalize the initial Hamiltonian H_i. We then have $\mathbf{\Psi} = \mathbf{U}^\dagger\mathbf{\Gamma}$, where $\mathbf{U}$ is the eigenbasis of the final Hamiltonian H,

$$\mathbf{U} = \begin{pmatrix} \mathbf{g^{(f)}} & \mathbf{h^{(f)}} \\ \mathbf{h^{(f)}} & \mathbf{g^{(f)}} \end{pmatrix}.$$

We can readily perform a backward transformation to verify that $\mathbf{\Psi} = \left(c_1 \dots c_N, c_1^\dagger \dots c_N^\dagger\right)$.

$$\mathbf{\Psi} = \mathbf{U}^\dagger\mathbf{\Gamma} = \begin{pmatrix} \mathbf{g^{T(f)}} & \mathbf{h^{T(f)}} \\ \mathbf{h^{T(f)}} & \mathbf{g^{T(f)}} \end{pmatrix} \begin{pmatrix} \eta_1 \\ \vdots \\ \eta_N \\ \\ \eta_1^\dagger \\ \vdots \\ \eta_N^\dagger \end{pmatrix}.$$

$$\mathbf{\Psi} = \begin{pmatrix} \mathbf{g^{T(f)}}\eta + \mathbf{h^{T(f)}}\eta^\dagger \\ \vdots \\ \mathbf{g^{T(f)}}\eta + \mathbf{h^{T(f)}}\eta^\dagger \\ \\ \mathbf{h^{T(f)}}\eta + \mathbf{g^{T(f)}}\eta^\dagger \\ \vdots \\ \mathbf{h^{T(f)}}\eta + \mathbf{g^{T(f)}}\eta^\dagger \end{pmatrix} = \begin{pmatrix} c_1 \\ \vdots \\ c_N \\ c_1^\dagger \\ \vdots \\ c_N^\dagger \end{pmatrix},$$

where $c_k = \sum_i g_{k,i}^{T(f)} \eta_i^{(i)} + h_{k,i}^{T(f)} \eta_i^{(i)\dagger}$ follows from Equations (A.7) and (A.8).

Substituting $\mathbf{\Psi} = \mathbf{U}^\dagger \mathbf{\Gamma}$ in Eq. (5.8), we can express H in the eigenstates which diagonalize the Hamiltonian

$$H = \mathbf{\Psi}^\dagger \mathcal{H} \mathbf{\Psi} = \mathbf{\Gamma}^\dagger \mathbf{U} \mathcal{H} \mathbf{U}^\dagger \mathbf{\Gamma} \equiv \mathbf{\Gamma}^\dagger \mathbf{D} \mathbf{\Gamma},$$

where $\mathbf{D}$ is a $2N \times 2N$ diagonal matrix, whose elements are the energy eigenvalues of the final Hamiltonian H.

$$\mathbf{D} = \begin{pmatrix} \mathbf{E^{(f)}} & 0 \\ 0 & -\mathbf{E^{(f)}} \end{pmatrix} = \begin{pmatrix} E_1^f & & & & & \\ & \ddots & & & 0 & \\ & & E_N^f & & & \\ & & & -E_N^f & & \\ & 0 & & & \ddots & \\ & & & & & -E_1^f \end{pmatrix}.$$

It then follows that

$$\mathcal{H} = \mathbf{U}^\dagger \mathbf{D} \mathbf{U}, \tag{A.10}$$

from which we can easily calculate the exponential $e^{-i\mathcal{H}t}$ in the eigenbasis of H using a transformation

$$e^{-i\mathcal{H}t} = \mathbf{U}^\dagger e^{-i\mathbf{D}t} \mathbf{U}. \tag{A.11}$$

It is easy to verify the above Equation by substituting $\mathcal{H} = \mathbf{U}^\dagger \mathbf{D} \mathbf{U}$ the exponential term $e^{-i\mathcal{H}t}$.

$$
\begin{aligned}
e^{-i\mathcal{H}t} &= e^{-i(\mathbf{U}^\dagger \mathbf{D}\mathbf{U})t} = e^{\mathbf{U}^\dagger(-i\mathbf{D}t)\mathbf{U}} \\
&= \sum_{k=0}^{\infty} \frac{\mathbf{U}^\dagger(-i\mathbf{D}t)\mathbf{U}}{k!} \\
&= \mathbb{1} + \mathbf{U}^\dagger(-i\mathbf{D}t)\mathbf{U} + \frac{(\mathbf{U}^\dagger(-i\mathbf{D}t)\mathbf{U})^2}{2!} + \dots \\
&= \mathbf{U}^\dagger \mathbb{1} \mathbf{U} + \mathbf{U}^\dagger(-i\mathbf{D}t)\mathbf{U} + \mathbf{U}^\dagger \frac{(-i\mathbf{D}t)}{2!}\mathbf{U} + \dots \\
&= \mathbf{U}^\dagger \left[\mathbb{1} + (-i\mathbf{D}t) + \frac{(-i\mathbf{D}t)}{2!} + \dots \right] \mathbf{U} \\
&= \mathbf{U}^\dagger \left[\sum_{k=0}^{\infty} \frac{-i\mathbf{D}t}{k!} \right] \mathbf{U} \\
\therefore\ e^{-i\mathcal{H}t} &= \mathbf{U}^\dagger e^{-i\mathbf{D}t} \mathbf{U}.
\end{aligned}
$$

A.3 The Determinant Formula

Finally, we show that Eq. (5.10) is valid via an intermediate step. Substituting Eq. (5.8) into Eq. (5.2), we get

$$
\begin{aligned}
\mathcal{L}(t) &= |\left\langle \Psi_0 \right| e^{-iHt} \left| \Psi_0 \right\rangle|^2 \\
&= \left| \left\langle e^{-it\sum_j \Psi_j^\dagger \mathcal{H} \Psi_j} \right\rangle \right|^2 .
\end{aligned}
$$

Recalling that $\mathbf{\Psi}^\dagger = \left(c_1^\dagger \dots c_N^\dagger, c_1 \dots c_N \right)$ are the fermionic operators on the ground state of the initial Hamiltonian H_i. Since $\langle \Psi_j^\dagger \Psi_k \rangle = \delta_{j,k}$, and all other expectation values are zeros, we can use on-site density operators $c_j^\dagger c_j$ in the above

expression,

$$\sum_{j}^{N} \Psi_j^{\dagger} \mathcal{H} \Psi_j \Rightarrow \sum_{j}^{2N} c_j^{\dagger} \mathcal{H} c_j.$$

From here we will show the derivation for Eq. (5.9), namely

$$\left| \left\langle e^{-it \sum_j c_j^{\dagger} \mathcal{H} c_j} \right\rangle \right|^2 \Longrightarrow |\det(1 - \mathbf{C} + \mathbf{C} e^{-i\mathcal{H}t})|^2.$$

We use the modification of an appraoch originally due to Lieb, Schultz and Mattis ([111, 147]). It is based on a representation of the correlation function $R(Q, l)$ of the Equation as the Toeplitz determinant

$$R(Q, 2N) = \left\langle \exp\, iQ \sum_{j}^{2N} c_j^{\dagger} c_j \right\rangle = \det(M^{(2N)})$$

where $M^{(2N)}$ is an $2N \times 2N$ matrix, and Q is an arbitrary complex value, which can be set to the individual elements of the final Hamiltonian H multiplied by t,

$$Q = -\mathcal{H}_j t.$$

The following relation holds

$$e^{iQc_j^{\dagger} c_j} = (c_j^{\dagger} + c_j)(c_j^{\dagger} + e^{iQ} c_j)$$

which is readily verfied in the representation diagonalization $c_j^{\dagger} c_j$ ([147]). Defining

$$A_j = c_j^{\dagger} + c_j, \quad B_j = c_j^{\dagger} + e^{iQ} c_j,$$

we have

$$R(-\mathcal{H}t, 2N) = \left\langle \exp\left(-it\sum_{j}^{2N} \mathcal{H}c_j^\dagger c_k\right)\right\rangle = \langle A_1 B_1 A_1 B_2 \dots B_{2N-1} A_{2N} B_{2N}\rangle.$$

By applying the Wick theorem, we are allowed to express the expectation value in terms of expectation values of products of just two operators. One notices that

$$\langle A_j A_k\rangle = \langle B_j B_k\rangle = 0, \quad j \neq k,$$

and

$$\langle A_j B_k\rangle = \delta_{jk} - (1 - e^{-i\mathcal{H}t})C_{jk},$$

where $C_{jk} = \langle c_j^\dagger c_k\rangle$ is matrix element of the two-point fermionic correlation function defined in Eq. (A.9). The most straightforward contribution is

$$\langle A_1 B_1\rangle\langle A_2 B_2\rangle \dots \langle A_{2N} B_{2N}\rangle$$

As a result the $2N \times 2N$, matrix $M_{ij}^{(2N)}$ can be expressed in terms of A_j and B_j,

$$M^{(2N)} = \begin{pmatrix} \langle A_1 B_1\rangle & 0 & & & \\ 0 & \langle A_1 B_1\rangle & & 0 & \\ & & \ddots & & \\ & 0 & & \langle A_{2N-1} B_{2N-1}\rangle & 0 \\ & & & 0 & \langle A_{2N} B_{2N}\rangle \end{pmatrix}$$

$$
\begin{aligned}
M^{(2N)} &= \langle A_1 B_1 \rangle \langle A_2 B_2 \rangle \dots \langle A_N B_N \rangle \\
M^{(2N)} &= \big[1 - (1 - e^{-i\mathcal{H}t}) C_{1,1}\big] \times \\
&\quad \big[1 - (1 - e^{-i\mathcal{H}t}) C_{2,2}\big] \times \dots \\
&\quad \big[1 - (1 - e^{-i\mathcal{H}t}) C_{2N,2N}\big] \\
M^{(2N)} &= \mathbb{1} - (1 - e^{-i\mathcal{H}t})\mathbf{C}
\end{aligned}
$$

Therefore,

$$
\begin{aligned}
|R(-Ht, 2N)| &= \left| \left\langle e^{-it \sum_j c_j^\dagger \mathcal{H} c_j} \right\rangle \right| = \left| \det(M^{(2N)}) \right| \\
&= \left| \det\big[\mathbb{1} - (1 - e^{-i\mathcal{H}t})\mathbf{C}\big] \right| \\
&= \left| \det\big(\mathbb{1} - \mathbf{C} + \mathbf{C} e^{-i\mathcal{H}t}\big) \right|.
\end{aligned}
$$

Therefore, we have arrived Eq. (5.10) as desired

$$
\mathcal{L}(t) = |\langle \Psi_0 | e^{-iHt} | \Psi_0 \rangle|^2 = |\det(\mathbb{1} - \mathbf{C} + \mathbf{C} e^{-i\mathcal{H}t})|^2.
$$

In short, we have shown that the Loschmidt echo equations are equivalent. The two-point correlation matrix $\mathbf{C}$ in the eigenbasis and the exponential form $e^{-i\mathcal{H}t}$ are crucial components in evaluating the LE for the single-particle problem where the Hamiltonian is bilinear and hermitian. We have also demonstrated the equivalence of those equations numerically for both the SSH model and the XXZ model in Chapter 5.

Appendix B

Mathematica Algorithm for the XX Model

MPH Approach: Quench from Neel State for the clean XX Model with L = 2 and OBC

```
MH = {{0, 0.5}, {0.5, 0}}
```

```
{{0, 0.5}, {0.5, 0}}
```

```
MH // MatrixForm
```

$$\begin{pmatrix} 0 & 0.5 \\ 0.5 & 0 \end{pmatrix}$$

```
ME = Sort[Eigenvalues[MH], Greater]
```

```
{0.5, -0.5}
```

```
evol = Exp[-it ME]
```

$$\left\{e^{-0.5\,it},\ e^{0.5\,it}\right\}$$

```
{MV1, MV2} = Normalize /@ Eigenvectors[MH]
```

```
{{-0.707107, 0.707107}, {0.707107, 0.707107}}
```

```
U = MV1
```

```
{-0.707107, 0.707107}
```

```
LE = Abs[Simplify[evol.(U^2)]]^2
```

$$\text{Abs}\left[0.5\,e^{-0.5\,it} + 0.5\,e^{0.5\,it}\right]^2$$

SPH Approach: Quench from Neel State for the XX Model with L = 2 and OBC

```
SH = {{0, 0.5}, {0.5, 0}}
```

```
{{0, 0.5}, {0.5, 0}}
```

```
SH // MatrixForm
```

$$\begin{pmatrix} 0 & 0.5 \\ 0.5 & 0 \end{pmatrix}$$

```
EV = Sort[Eigenvalues[SH], Greater]
```

```
{0.5, -0.5}
```

```
ED = DiagonalMatrix[Exp[-it EV]]
```

$$\left\{\left\{e^{-0.5\,it}, 0.\right\}, \left\{0., e^{0.5\,it}\right\}\right\}$$

```
{V1, V2} = Simplify[Normalize /@ Eigenvectors[SH]]
```

```
{{-0.707107, 0.707107}, {0.707107, 0.707107}}
```

```
V = {V2, V1}
```

```
{{0.707107, 0.707107}, {-0.707107, 0.707107}}
```

```
Ut = Conjugate[V].ED.ConjugateTranspose[V]
```

```
CM = {{1, 0}, {0, 0}}
```

```
{{1, 0}, {0, 0}}
```

```
ID = IdentityMatrix[2]
```

```
{{1, 0}, {0, 1}}
```

```
M = ID - CM + CM.Ut
```

```
R = Det[M]
```

$$0.5\,e^{-0.5\,it} + 0.5\,e^{0.5\,it}$$

```
Simplify[Expand[Simplify[R]]]
```

```
LE = Abs[%]^2
```

$$\text{Abs}\left[0.5\,e^{-0.5\,it} + 0.5\,e^{0.5\,it}\right]^2$$

MPH Approach: Quench from Neel State for the clean XX Model with L = 4 and OBC

```
MH = {{0, 0.5, 0, 0, 0, 0}, {0.5, 0, 0.5, 0.5, 0, 0}, {0, 0.5, 0, 0, 0.5, 0},
   {0, 0.5, 0, 0, 0.5, 0}, {0, 0, 0.5, 0.5, 0, 0.5}, {0, 0, 0, 0, 0.5, 0}}
```

```
{{0, 0.5, 0, 0, 0, 0}, {0.5, 0, 0.5, 0.5, 0, 0}, {0, 0.5, 0, 0, 0.5, 0},
 {0, 0.5, 0, 0, 0.5, 0}, {0, 0, 0.5, 0.5, 0, 0.5}, {0, 0, 0, 0, 0.5, 0}}
```

```
MH // MatrixForm
```

$$\begin{pmatrix} 0 & 0.5 & 0 & 0 & 0 & 0 \\ 0.5 & 0 & 0.5 & 0.5 & 0 & 0 \\ 0 & 0.5 & 0 & 0 & 0.5 & 0 \\ 0 & 0.5 & 0 & 0 & 0.5 & 0 \\ 0 & 0 & 0.5 & 0.5 & 0 & 0.5 \\ 0 & 0 & 0 & 0 & 0.5 & 0 \end{pmatrix}$$

```
ME = Simplify[Sort[Eigenvalues[MH], Greater]]
```

$$\{1.11803,\ 0.5,\ 1.06254 \times 10^{-16},\ 0.,\ -0.5,\ -1.11803\}$$

```
evol = Exp[-it ME]
```

$$\{e^{-1.11803\, it},\ e^{-0.5\, it},\ e^{-1.06254\times 10^{-16}\, it},\ 1.,\ e^{0.5\, it},\ e^{1.11803\, it}\}$$

```
{MV1, MV2, MV3, MV4, MV5, MV6} = Normalize /@ Eigenvectors[MH]
```

$$\{\{-0.223607,\ -0.5,\ -0.447214,\ -0.447214,\ -0.5,\ -0.223607\},$$
$$\{-0.223607,\ 0.5,\ -0.447214,\ -0.447214,\ 0.5,\ -0.223607\},$$
$$\{0.5,\ 0.5,\ 4.44089 \times 10^{-16},\ 4.44089 \times 10^{-16},\ -0.5,\ -0.5\},$$
$$\{-0.5,\ 0.5,\ -4.44089 \times 10^{-16},\ -4.44089 \times 10^{-16},\ -0.5,\ 0.5\},$$
$$\{0.632456,\ 2.81452 \times 10^{-308},\ -0.316228,\ -0.316228,\ 6.3195 \times 10^{-16},\ 0.632456\},$$
$$\{0.,\ 0.,\ 0.707107,\ -0.707107,\ 0.,\ 0.\}\}$$

```
U = MV4
```

$$\{-0.5,\ 0.5,\ -4.44089 \times 10^{-16},\ -4.44089 \times 10^{-16},\ -0.5,\ 0.5\}$$

```
LE = Abs[Simplify[evol.(U^2)]]^2
```

$$\text{Abs}\left[1.97215 \times 10^{-31} + 0.25\, e^{-1.11803\, it} + 0.25\, e^{-0.5\, it} + 1.97215 \times 10^{-31}\, e^{-1.06254\times 10^{-16}\, it} + 0.25\, e^{0.5\, it} + 0.25\, e^{1.11803\, it}\right]^2$$

SPH Approach: Quench from Neel State for the XX Model with L = 4 and OBC

```
In[118]:= SH = {{0, 0.5, 0, 0}, {0.5, 0, 0.5, 0}, {0, 0.5, 0, 0.5}, {0, 0, 0.5, 0}}
Out[118]= {{0, 0.5, 0, 0}, {0.5, 0, 0.5, 0}, {0, 0.5, 0, 0.5}, {0, 0, 0.5, 0}}

In[119]:= SH // MatrixForm
Out[119]//MatrixForm=
```

$$\begin{pmatrix} 0 & 0.5 & 0 & 0 \\ 0.5 & 0 & 0.5 & 0 \\ 0 & 0.5 & 0 & 0.5 \\ 0 & 0 & 0.5 & 0 \end{pmatrix}$$

```
In[120]:= EV = Sort[Eigenvalues[SH], Greater]
Out[120]= {0.809017, 0.309017, -0.309017, -0.809017}

In[121]:= ED = DiagonalMatrix[Exp[-it EV]]
Out[121]= {{e^(-0.809017 it), 0., 0., 0.}, {0., e^(-0.309017 it), 0., 0.},
           {0., 0., e^(0.309017 it), 0.}, {0., 0., 0., e^(0.809017 it)}}

In[122]:= {V1, V2, V3, V4} = Simplify[Normalize /@ Eigenvectors[SH]]
Out[122]= {{0.371748, 0.601501, 0.601501, 0.371748},
           {0.371748, -0.601501, 0.601501, -0.371748},
           {-0.601501, -0.371748, 0.371748, 0.601501},
           {0.601501, -0.371748, -0.371748, 0.601501}}

In[123]:= V = {V2, V4, V3, V1}

In[124]:= Ut = Conjugate[V].ED.ConjugateTranspose[V]

In[126]:= CM = {{1, 0, 0, 0}, {0, 0, 0, 0}, {0, 0, 1, 0}, {0, 0, 0, 0}}
Out[126]= {{1, 0, 0, 0}, {0, 0, 0, 0}, {0, 0, 1, 0}, {0, 0, 0, 0}}

In[127]:= ID = IdentityMatrix[4]
Out[127]= {{1, 0, 0, 0}, {0, 1, 0, 0}, {0, 0, 1, 0}, {0, 0, 0, 1}}

In[128]:= M = ID - CM + CM.Ut

In[129]:= R = Det[M]

In[130]:= Simplify[Expand[Simplify[R]]]

In[131]:= LE = Abs[%]^2
Out[131]= Abs[5.55112 × 10^-17 - 1.38778 × 10^-17 e^(-1.61803 it) + 0.25 e^(-1.11803 it) + 1.38778 × 10^-17 e^(-0.618034 it) +
            0.25 e^(-0.5 it) + 0.25 e^(0.5 it) + 1.38778 × 10^-17 e^(0.618034 it) + 0.25 e^(1.11803 it)]^2
```

Appendix C

Python Algorithms

```
"""
Created by Ye Cheng (Lewis) Chen and Jesko Sirker
The non-interacting disordered SSH model
Calculation for Loschmidt echo using SPH and formula |det(1-C+C*exp(-iHt))|^2
"""
import numpy as np
import argparse

# parameters for entanglement calculations
parser = argparse.ArgumentParser(description=
'Calculation of Loschmidt echo for disordered fermions')
parser.add_argument('-L', type=int, default=4,
                    help='# system length L')
parser.add_argument('-W', type=float, default=0.0,
                    help='width box potential disorder')
parser.add_argument('-delta', type=float, default=-0.3,
                    help='# quench parameter delta')
parser.add_argument('-dt', type=float, default=0.01,
                    help='# discrete time interval first part')
parser.add_argument('-tint', type=float, default=0,
                    help='# maximum time range first part')
parser.add_argument('-tmax', type=float, default=20,
                    help='# maximum time range second part')
parser.add_argument('-sample', type=int, default=1,
                    help='# samples')
parser.add_argument('-openbc', type=int, default=1,
                    help='OBC = 1, PBC = 0')
args=parser.parse_args()

# construct Hamiltonian for SSH model with disorder in diagonal elements
# diagnonal elements are random numbers in [-W,W]
def construct_APDW(L,W):
    if args.W != 0.0:
        a = 2*W * np.random.random_sample(L) - W
    else:
        a = np.zeros(L)
    A = np.diag(a,0)
    return A

# construct single-particle Hamiltonian for SSH model
def construct_SPH(delta,L,openbc):
    H = np.zeros((L,L))
    for i in range(0,L-1):
        H[i,i+1]=1.0-delta*(-1)**i
        H[i+1,i]=1.0-delta*(-1)**i
    if openbc == 0:
        H[0][-1]=1.0+delta*(-1)**L
        H[-1][0]=1.0+delta*(-1)**L
    return H

# construct unitary time evolution operator Uexp(-iDt)U*
def construct_U(v,U,t):
    Ut = np.dot(U.conj(),np.dot(np.diag(np.exp(-1j*v*t)),(U.transpose()).conj()))
    return Ut
```

```
# construct two point correlation matrix
def construct_CM(U,L):
    m1=np.array([[1,0],[0,0]])
    smat=np.kron(m1,np.identity(int(L/2)))
    CM = np.dot(U,np.dot(smat,U.transpose()))
    return CM

# calculate LE using |det(1-C+C*exp(-iHt))|
def calc_detLE(v,U,CM,t):
    LE=np.zeros(len(t))
    for i in t:
        Ut = construct_U(v,U,i)
        k=t.tolist().index(i)
        LE[k]=np.abs(np.linalg.det(np.identity(args.L)-CM+np.dot(CM,Ut)))
    return LE

# Run the program for both cases
t=np.arange(args.tint,args.tmax+args.dt/2,args.dt)

# calculate single-particle Hamiltonian
SPHi = construct_SPH(args.delta,args.L,args.openbc)
SPHf = construct_SPH(-args.delta,args.L,args.openbc)

Store1=0
for samp in range(int(args.sample)):
    APDW = construct_APDW(args.L,args.W)
    SPHiW = SPHi + APDW
    SPHfW = SPHf + APDW
    vsi,Usi = np.linalg.eigh(SPHiW)
    vsf,Usf = np.linalg.eigh(SPHfW)
    CM = construct_CM(Usi,args.L)
    Store1 += calc_detLE(vsf,Usf,CM,t)

LE1=np.squeeze(Store1/args.sample)
RR1=-2*np.log(LE1)/args.L # return rate

for item in RR1:
    print(item)
```

```
"""
Created by Ye Cheng (Lewis) Chen and Jesko Sirker
The interacting disordered SSH model
Calculation for Loschmidt echo using SPH and formula |det(1-C+C*exp(-iHt))|^2
"""
import numpy as np
import argparse
from bisect import bisect_left as findIndex

# parameters for entanglement calculations
parser = argparse.ArgumentParser(description=
'Calculation of Loschmidt echo for disordered fermions')
parser.add_argument('-L', type=int, default=4,
                    help='# system length L')
parser.add_argument('-V', type=float, default=1.0,
                    help='V interaction term')
parser.add_argument('-W', type=float, default=0.0,
                    help='width box potential disorder')
parser.add_argument('-delta', type=float, default=-0.5,
                    help='# quench parameter delta')
parser.add_argument('-tint', type=float, default=0,
                    help='# initial time')
parser.add_argument('-tmax', type=float, default=20,
                    help='# maximum time range')
parser.add_argument('-dt', type=float, default=0.01,
                    help='# discrete time interval')
parser.add_argument('-sample', type=int, default=1,
                    help='# samples')
parser.add_argument('-openbc', type=int, default=1,
                    help='OBC = 1, PBC = 0')
parser.add_argument('-Vfix', type=int, default=1,
                    help='V is fixed = 1, Vary = 0')
args=parser.parse_args()

# State function configurations in spinless fermions
def manyPsi(particle,site):
    a=np.arange(2**site)
    bitcount=np.array([bin(x).count("1") for x in a])
    b=a.compress(bitcount==particle).tolist()[::-1]
    aList=[]
    for item in b:
        a=bin(int(item))[2:].zfill(site)
        aList.append(a)
    return aList

# C+C fermionic operators on Neel configurations
def cpc(l,j,Psi):
    Psi2=Psi.copy()
    for item in Psi2:
        k = Psi2.index(item)
        if item[j-1]=='0':
            Psi2[k]=list(item)
            Psi2[k][j-1]='1'
            Psi2[k]="".join(Psi2[k])
        if item[j-1]=='1':
            Psi2[k]=list(item)
            Psi2[k][j-1]='0'
```

```
            Psi2[k]="".join(Psi2[k])
    for item in Psi2:
        k = Psi2.index(item)
        if item[l-1]=='0':
            Psi2[k]=list(item)
            Psi2[k][l-1]='1'
            Psi2[k]="".join(Psi2[k])
        if item[l-1]=='1':
            Psi2[k]=list(item)
            Psi2[k][l-1]='0'
            Psi2[k]="".join(Psi2[k])
    return Psi2

# construct Hamiltonian for SSH model with disorder in diagonal elements
# diagnonal elements are random numbers in [-W,W]
def construct_MPDW(Psi,L,W):
    if args.W != 0.0:
        a = 2*W * np.random.random_sample(L) - W #mu in [-W,W]
    else:
        a = np.zeros(L)
    C = np.zeros(len(Psi))
    for i in range(len(Psi)):
        item=Psi[i]
        for j in range(len(item)):
            if item[j]=='1':
                C[i]+=a[j]
    A = np.diag(C)
    return A

def findMagnetizationStates(length,particlenumber):
    """
    constructs a table with the integer representations of all binaries
    with a given number of 1s
    """
    s = np.arange(2**length)
    bitcount = np.array([bin(x).count("1") for x in s])
    return s.compress(bitcount==particlenumber)

def bit(state,j,length):
    """return value of bit j"""
    return state >> (length-1-j) & 1

def bitFlip(state,j,k,length):
    """flip bits j and k of state if they are unequal"""
    return state ^ (2**(length-1-j)+2**(length-1-k))

# construct many-particle Hamiltonian for clean SSH model
def construct_MPH(V,delta,length,table):
    """construct clean Hamiltonian"""
    nos = len(table)
    h = np.zeros((nos,nos),np.float)
    for b,t in enumerate(table): # loop over eigenstates
        for j in range(length-args.openbc): # loop over sites
            k = (j+1)%length # right neighboring site
            # Heisenberg interaction for equal nearest neighbors
            if bit(t,j,length)==bit(t,k,length):
                h[b,b]+=0.25*V
```

```
            # Heisenberg interaction + tunneling for unequal nearest neighbors
            else:
                h[b,b]-=0.25*V
                bp = findIndex(table, bitFlip(t, j, k, length))
                #bp = findIndex(table, bitFlip(t, j, k, length))-1
                h[b,bp]=1.0-delta*(-1)**j
    return h

def calc_LE(vmi,Umi,vmf,Umf,t): # return rate starting from intial state
    """compute time evolution from ground state of MPHi"""
    Uindex=vmi.tolist().index(min(vmi))
    Ui=Umi[Uindex]
    LE = np.zeros(len(t))
    evol = np.exp(-1j*t[:,np.newaxis]*vmf[np.newaxis])
    vv=np.dot(Umf.transpose().conj(),Ui)
    """ |<Psi0|U*exp(-iEt)*U|Psi0>|"""
    LE=np.abs(np.inner(evol*vv[np.newaxis,:],vv[np.newaxis,:]))
    return LE

# Run the program for both cases
t=np.arange(args.tint,args.tmax+args.dt/2,args.dt)

# calculate many-particle Hamiltonian
particlenumber=args.L/2
Psi=manyPsi(particlenumber,args.L)
table = findMagnetizationStates(args.L,particlenumber)
# condition for fixing interaction strength V
if args.Vfix == 1:
    MPHi = construct_MPH(args.V,args.delta,args.L,table)
elif args.Vfix == 0:
    MPHi = construct_MPH(0,args.delta,args.L,table)
MPHf = construct_MPH(args.V,-args.delta,args.L,table)

Store2=0
for samp in range(int(args.sample)):
    MPDW = construct_MPDW(Psi,args.L,args.W)
    MPHiW = MPHi + MPDW
    MPHfW = MPHf + MPDW
    vmi,Umi = np.linalg.eig(MPHiW)
    Umi=Umi.transpose()
    vmf,Umf = np.linalg.eig(MPHfW)
    Store2 += calc_LE(vmi,Umi,vmf,Umf,t)

LE2=np.squeeze(Store2/args.sample)
RR2=-2*np.log(LE2)/args.L

for item in RR2:
    print(item)
```

```
"""
Created by Ye Cheng (Lewis) Chen and Jesko Sirker
The disordered XX model (non-interacting)
Calculation for Loschmidt echo using SPH and formula |det(1-C+C*exp(-iHt))|^2
"""
import numpy as np
import argparse


# parameters for entanglement calculations
parser = argparse.ArgumentParser(description=
'Calculation of Loschmidt echo for disordered fermions')
parser.add_argument('-L', type=int, default=4,
                    help='# system length L')
parser.add_argument('-W', type=float, default=1.0,
                    help='width box potential disorder')
parser.add_argument('-dt', type=float, default=0.01,
                    help='# discrete time interval first part')
parser.add_argument('-tint', type=float, default=0,
                    help='# maximum time range first part')
parser.add_argument('-tmax', type=float, default=20,
                    help='# maximum time range second part')
parser.add_argument('-sample', type=int, default=30,
                    help='# samples')
parser.add_argument('-openbc', type=int, default=1,
                    help='OBC = 1, PBC = 0')
args=parser.parse_args()

# construct Hamiltonian for SSH model with disorder in diagonal elements
# diagnonal elements are random numbers in [-W/2,W/2]
def construct_APDW(L,W):
    if args.W != 0.0:
        a = 2*W * np.random.random_sample(L) - W
    else:
        a = np.zeros(L)
    A = np.diag(a,0)
    return A

# construct single-particle Hamiltonian for SSH model
def construct_SPH(L,openbc):
    H = np.zeros((L,L))
    for i in range(0,L-1):
        H[i,i+1]=0.5
        H[i+1,i]=0.5
    if openbc == 0:
        H[0][-1]=0.5
        H[-1][0]=0.5
    return H

# construct unitary time evolution operator Uexp(-iDt)U*
def construct_U(v,U,t):
    Ut = np.dot(U.conj(),np.dot(np.diag(np.exp(-1j*v*t)),(U.transpose()).conj()))
    return Ut
```

```
# construct two point correlation matrix for HD
def construct_CM(L):
    Neel = np.zeros((int(L),int(L/2)))
    for i in range(0,int(L)):
        for j in range(0,int(L/2)):
            if i+1==2*(j+1)-1: Neel[i,j]=1
    CM = np.dot(Neel,Neel.transpose())          # CM in Ising basis
    return CM

# calculate LE using |det(1-C+C*exp(-iHt))|
def calc_detLE(v,U,CM,t):
    LE=np.zeros(len(t))
    for i in t:
        Ut = construct_U(v,U,i)
        k=t.tolist().index(i)
        LE[k]=np.abs(np.linalg.det(np.identity(args.L)-CM+np.dot(CM,Ut)))
    return LE


# Run the program
t=np.arange(args.tint,args.tmax+args.dt/2,args.dt)

# calculate part the single-particle Hamiltonian
SPH = construct_SPH(args.L,args.openbc)
vs,Us = np.linalg.eigh(SPH)
CM = construct_CM(args.L)

Store1=0
for samp in range(int(args.sample)):
    APDW = construct_APDW(args.L,args.W)
    SPHfW = SPH + APDW
    vsf,Usf = np.linalg.eigh(SPHfW)
    Store1 += calc_detLE(vsf,Usf,CM,t)

LE1=np.squeeze(Store1/args.sample)
RR1=-2*np.log(LE1)/args.L

for item in RR1:
    print(item)
```

```
"""
Created by Ye Cheng (Lewis) Chen and Jesko Sirker
The disordered XXZ model
Calculation for Loschmidt echo using SPH and formula |det(1-C+C*exp(-iHt))|^2
"""
import numpy as np
import argparse
from bisect import bisect_left as findIndex

# parameters for entanglement calculations
parser = argparse.ArgumentParser(description=
'Calculation of Loschmidt echo for disordered fermions')
parser.add_argument('-L', type=int, default=4,
                    help='# system length L')
parser.add_argument('-V', type=float, default=1.0,
                    help='V interaction term')
parser.add_argument('-W', type=float, default=0.0,
                    help='width box potential disorder')
parser.add_argument('-tint', type=float, default=0,
                    help='# initial time')
parser.add_argument('-tmax', type=float, default=50,
                    help='# maximum time range')
parser.add_argument('-dt', type=float, default=0.005,
                    help='# discrete time interval')
parser.add_argument('-sample', type=int, default=1,
                    help='# samples')
parser.add_argument('-openbc', type=int, default=1,
                    help='OBC = 1, PBC = 0')
args=parser.parse_args()

# State function configurations in spinless fermions
def manyPsi(particle,site):
    a=np.arange(2**site)
    bitcount=np.array([bin(x).count("1") for x in a])
    b=a.compress(bitcount==particle).tolist()[::-1]
    aList=[]
    for item in b:
        a=bin(int(item))[2:].zfill(site)
        aList.append(a)
    return aList

# C+C fermionic operators on Neel configurations
def cpc(l,j,Psi):
    Psi2=Psi.copy()
    for item in Psi2:
        k = Psi2.index(item)
        if item[j-1]=='0':
            Psi2[k]=list(item)
            Psi2[k][j-1]='1'
            Psi2[k]="".join(Psi2[k])
        if item[j-1]=='1':
            Psi2[k]=list(item)
            Psi2[k][j-1]='0'
            Psi2[k]="".join(Psi2[k])
    for item in Psi2:
        k = Psi2.index(item)
        if item[l-1]=='0':
```

```
            Psi2[k]=list(item)
            Psi2[k][l-1]='1'
            Psi2[k]="".join(Psi2[k])
        if item[l-1]=='1':
            Psi2[k]=list(item)
            Psi2[k][l-1]='0'
            Psi2[k]="".join(Psi2[k])
    return Psi2

def construct_MPDW(Psi,L,W):
    if args.W != 0.0:
        a = 2*W * np.random.random_sample(L) - W #mu in [-W,W]
    else:
        a = np.zeros(L)
    C = np.zeros(len(Psi))
    for i in range(len(Psi)):
        item=Psi[i]
        for j in range(len(item)):
            if item[j]=='1':
                C[i]+=a[j]
    A = np.diag(C)
    return A

def findMagnetizationStates(length,particlenumber):
    """
    constructs a table with the integer representations of all binaries
    with a given number of 1s
    """
    s = np.arange(2**length)
    bitcount = np.array([bin(x).count("1") for x in s])
    return s.compress(bitcount==particlenumber)

def bit(state,j,length):
    """return value of bit j"""
    return state >> (length-1-j) & 1
def bitFlip(state,j,k,length):
    """flip bits j and k of state if they are unequal"""
    return state ^ (2**(length-1-j)+2**(length-1-k))

# construct many-particle Hamiltonian for clean SSH model
def construct_MPH(V,length,table):
    """construct clean Hamiltonian"""
    nos = len(table)
    h = np.zeros((nos,nos),np.float)
    for b,t in enumerate(table): # loop over eigenstates
        for j in range(length-args.openbc): # loop over sites
            k = (j+1)%length # right neighboring site
            # Heisenberg interaction for equal nearest neighbors
            if bit(t,j,length)==bit(t,k,length):
                h[b,b]+=0.25*V
            # Heisenberg interaction + tunneling for unequal nearest neighbors
            else:
                h[b,b]-=0.25*V
                bp = findIndex(table, bitFlip(t, j, k, length))
                #bp = findIndex(table, bitFlip(t, j, k, length))-1
                h[b,bp]=0.5
    return h
```

```
# find Neel state in eigenbasis
def findNeelstate(length,particlenumber,table):
    """find positions of Neel states in table"""
    assert length==2*particlenumber, "need exactly half filling for Neel state"
    tot = 2**length-1
    N2 = tot//3   # integer representation of the Neel state 010101...
    N1 = tot-N2   # integer representation of the other Neel state 101010...
    return findIndex(table,N1), findIndex(table,N2)


def calc_LE(v,U,Neelpos,tint,tmax,dt): # return rate starting from Neel state
    t = np.arange(tint,tmax+dt/2,dt)
    """compute time evolution from Neel state"""
    vNeel=U[Neelpos[0]].conj()     # Neel state |1010> in eigenbasis |c1 c2 ...>
    LE = np.zeros(len(t))
    evol = np.exp(-1j*t[:,np.newaxis]*v[np.newaxis])
    """ <vNeel*U|U*exp(-iEt)*U|U*Neel>"""
    LE=np.abs(np.inner(evol*vNeel[np.newaxis,:],vNeel[np.newaxis,:]))
    return LE

# Run the program for both cases
t=np.arange(args.tint,args.tmax+args.dt/2,args.dt)

# calculate part the many-particle Hamiltonian
particlenumber=args.L/2
Psi=manyPsi(particlenumber,args.L)
table = findMagnetizationStates(args.L,particlenumber)
Neelpos = findNeelstate(args.L,particlenumber,table)
MPDW = construct_MPDW(Psi,args.L,args.W)
MPH = construct_MPH(args.V,args.L,table)
vmi,Umi = np.linalg.eigh(MPH)
Umi = Umi.transpose()


for i in range(args.dat):
    Store2=0
    for samp in range(int(args.sample)):
        MPDW = construct_MPDW(Psi,args.L,args.W)
        MPHfW = MPH + MPDW
        vmf,Umf = np.linalg.eigh(MPHfW)
        Store2 += calc_LE(vmf,Umi,Neelpos,args.tint,args.tmax,args.dt)

LE2=np.squeeze(Store2/args.sample)
RR2=-2*np.log(LE2)/args.L

for item in RR2:
    print(item)
```

Bibliography

[1] Rahul Nandkishore and David A Huse. Many-body localization and thermalization in quantum statistical mechanics. *Annu. Rev. Condens. Matter Phys.*, 6(1):15–38, 2015.

[2] Y Zhao, F Andraschko, and J Sirker. Entanglement entropy of disordered quantum chains following a global quench. *Phys. Rev. B*, 93(20):205146, 2016.

[3] Aart Lagendijk, Bart Van Tiggelen, and Diederik S Wiersma. Fifty years of anderson localization. *Physics Today*, 62(8):24–29, 2009.

[4] Alain Aspect and Massimo Inguscio. Anderson localization of ultracold atoms. *Physics Today*, 62(8):30–35, 2009. ISSN 0031-9228.

[5] János K. Asbóth, László Oroszlány, and András Pályi. *A Short Course on Topological Insulators*, volume 919 of *Lecture Notes in Physics*. Springer International Publishing, 2016. doi:10.1007/978-3-319-25607-8.

[6] Piers Coleman. *Introduction to many-body physics*. Cambridge University Press, 2015.

[7] R. Coldea, S. M. Hayden, G. Aeppli, T. G. Perring, C. D. Frost, T. E. Mason, S.-W. Cheong, and Z. Fisk. Spin waves and electronic interactions in La_2CuO_4. *Phys. Rev. Lett.*, 86:5377–5380, Jun 2001. doi:10.1103/PhysRevLett.86.5377.

[8] Wytse van Dijk, Calvin Lobo, Allison MacDonald, and Rajat K Bhaduri. Fisher zeros of a unitary bose gas. *Canadian Journal of Physics*, 93(8): 830–835, 2014.

[9] Markus Heyl. Dynamical quantum phase transitions: a review. *Reports on Progress in Physics*, 81(5):054001, 2018.

[10] Arseni Goussev, Rodolfo A Jalabert, Horacio M Pastawski, and Diego Wisniacki. Loschmidt echo. *arXiv preprint arXiv:1206.6348*, 2012.

[11] N. Sedlmayr, P. Jaeger, M. Maiti, and J. Sirker. Bulk-boundary correspondence for dynamical phase transitions in one-dimensional topological insulators and superconductors. *Phys. Rev. B*, 97:064304, Feb 2018. doi:10.1103/PhysRevB.97.064304.

[12] J Sirker, M Maiti, NP Konstantinidis, and N Sedlmayr. Boundary fidelity and entanglement in the symmetry protected topological phase of the ssh model. *Journal of Statistical Mechanics: Theory and Experiment*, 2014(10): P10032, 2014.

[13] J. Bardeen, L. N. Cooper, and J. R. Schrieffer. Theory of superconductivity. *Phys. Rev.*, 108:1175–1204, Dec 1957. doi:10.1103/PhysRev.108.1175.

[14] Yury Mnyukh and Vitaly Vodyanoy. Superconducting state and phase transitions. *arXiv:1607.04795*, 2016.

[15] Michael E. Fisher. Magnetism in one-dimensional systems—the heisenberg model for infinite spin. *American Journal of Physics*, 32(5):343–346, 1964. doi:10.1119/1.1970340.

[16] O. Babelon, H.J. de Vega, and C.M. Viallet. Analysis of the bethe ansatz equations of the xxz model. *Nuclear Physics B*, 220(1):13 – 34, 1983. ISSN 0550-3213. doi:https://doi.org/10.1016/0550-3213(83)90131-1.

[17] Maciej Lewenstein, Anna Sanpera, Veronica Ahufinger, Bogdan Damski, Aditi Sen, and Ujjwal Sen. Ultracold atomic gases in optical lattices: mimicking condensed matter physics and beyond. *Advances In Physics*, 56(2): 243–379, 2007.

[18] Giacomo Roati, Chiara D'Errico, Leonardo Fallani, Marco Fattori, Chiara Fort, Matteo Zaccanti, Giovanni Modugno, Michele Modugno, and Massimo Inguscio. Anderson localization of a non-interacting bose–einstein condensate. *Nature*, 453(7197):895, 2008.

[19] Alexander Altland. *Condensed matter field theory / Alexander Altland and Ben Simons.* Cambridge University Press, Cambridge ; New York, 2nd ed.. edition, 2010. ISBN 9780521769754.

[20] Piers Coleman. *Introduction to many-body physics.* Cambridge University Press, 2015.

[21] Lev Davidovich Landau. On the theory of phase transitions. I. *Phys. Z. Sowjet.*, 11:26, 1937.

[22] Ganesan Venkataraman, Debendranath Sahoo, and Venkataraman Balakrishnan. *Ergodicity Breaking*, pages 117–124. Springer Berlin Heidelberg, Berlin, Heidelberg, 1989. ISBN 978-3-642-83434-9. doi:10.1007/978-3-642-83434-9_8.

[23] Elbio Dagotto. Complexity in strongly correlated electronic systems. *Science*, 309(5732):257–262, 2005. ISSN 0036-8075. doi:10.1126/science.1107559.

[24] Subir Sachdev. Quantum magnetism and criticality. *Nature Physics*, 4(3): 173, 2008. doi:10.1038/nphys894.

[25] Mark Yosefin and Eytan Domany. Phase transitions in fully frustrated spin systems. *Phys. Rev. B*, 32:1778–1795, Aug 1985. doi:10.1103/PhysRevB.32.1778.

[26] Hung T Diep. *Magnetic systems with competing interactions: frustrated spin systems*. World Scientific, 1994.

[27] Michael Tinkham. *Introduction to superconductivity*. Courier Corporation, 2004.

[28] M. Z. Hasan and C. L. Kane. Colloquium: Topological insulators. *Rev. Mod. Phys.*, 82:3045–3067, Nov 2010. doi:10.1103/RevModPhys.82.3045.

[29] P. W. Anderson. Absence of diffusion in certain random lattices. *Phys. Rev.*, 109:1492–1505, Mar 1958. doi:10.1103/PhysRev.109.1492.

[30] P. Drude. Zur Elektronentheorie der Metalle. *Annalen der Physik*, 306: 566–613, 1900. doi:10.1002/andp.19003060312.

[31] Charles Kittel. *Introduction to Solid State Physics*. John Wiley & Sons, Inc., New York, 8th ed edition, 2004.

[32] Uichiro Mizutani. *Introduction to the Electron Theory of Metals*. Cambridge University Press, Cambridge, 2001. ISBN 9780511612626.

[33] Sima Dimitrijev. *Principles of semiconductor devices.* The Oxford series in electrical and computer engineering Principles of semiconductor devices. 2012. ISBN 1-62870-172-2.

[34] Giuseppe Grosso and Giuseppe Pastori Parravicini. *Solid State Physics.*, volume 2nd ed. Academic Press, 2013. ISBN 9780123850300.

[35] James D. Patterson and Bernard C. Bailey. *Solid-State Physics Introduction to the Theory.* Springer, New York, 2nd ed edition, 2010.

[36] David Ferry. *Semiconductor Transport.* CRC Press, 1 edition, May 2016. ISBN 9780748408665.

[37] R S Mulliken. Spectroscopy, molecular orbitals, and chemical bonding. *Science (New York, N.Y.)*, 157(3784), July 1967. ISSN 0036-8075.

[38] J. E. Lennard-jones. The electronic structure of some diatomic molecules. *Transactions of the Faraday Society*, 25:668–686, 1929. ISSN 0014-7672.

[39] L. I. Schiff and R. Hofstadter. Felix bloch: A brief professional biography. *Physics Today*, 18(12):42–43, December 1965. ISSN 0031-9228.

[40] H. Jones, N. F. Mott, and H. W. B. Skinner. A theory of the form of the x-ray emission bands of metals. *Phys. Rev.*, 45:379–384, Mar 1934. doi:10.1103/PhysRev.45.379.

[41] Linus Pauling. The nature of the interatomic forces in metals. *Phys. Rev.*, 54:899–904, Dec 1938. doi:10.1103/PhysRev.54.899.

[42] Walter A Harrison. *Electronic Structure and the Properties of Solids : The Physics of the Chemical Bond*. Dover Publications, New York, July 1989. ISBN 9780486660219.

[43] Howard C. Berg and Freeman Dyson. Random walks in biology. *Physics Today*, 40(3):73–74, March 1987. ISSN 0031-9228.

[44] Philip Charles Nelson. *Biological physics : energy, information, life*. W.H. Freeman and Co., New York, 2004. ISBN 0716743728.

[45] Albert Einstein. *Investigations on the theory of the Brownian movement,*. Methuen & co. ltd, London, 1926.

[46] Elena Agliari. *A Random Walk in Diffusion Phenomena and Statistical Mechanics*, page 43–141. Cambridge University Press, 2016. doi:10.1017/9781316403877.003.

[47] Oliver Mülken and Alexander Blumen. Continuous-time quantum walks: Models for coherent transport on complex networks. *Physics Reports*, 502(2):37 – 87, 2011. ISSN 0370-1573. doi:https://doi.org/10.1016/j.physrep.2011.01.002.

[48] Helmut Mehrer. *Diffusion in solids fundamentals, methods, materials, diffusion-controlled processes*. Springer Series in Solid-State Sciences, 155. Springer, Berlin ; [London], 2007. ISBN 1-280-95691-7.

[49] A. Abragam. The principles of nuclear magnetism. *American Journal of Physics*, 29(12):860–861, December 1961. ISSN 0002-9505.

[50] C. P. Slichter and Robert G. Griffin. Principles of magnetic resonance. *Physics Today*, 44(2):95–96, February 1991. ISSN 0031-9228.

[51] J Kempe. Quantum random walks: An introductory overview. *Contemporary Physics*, 44(4):307–327, 2003. doi:10.1080/0010715103100011077 6.

[52] F. Göbel and A.A. Jagers. Random walks on graphs. *Stochastic Processes and their Applications*, 2(4):311 – 336, 1974. ISSN 0304-4149. doi:https://doi.org/10.1016/0304-4149(74)90001-5.

[53] Philippe Blanchard. *Random walks and diffusions on graphs and databases an introduction*. Springer Series in Synergetics, 10. Springer, Berlin, 2011. ISBN 3-642-19592-X.

[54] E. P. Wigner. *Characteristic Vectors of Bordered Matrices with Infinite Dimensions I*, pages 524–540. Springer Berlin Heidelberg, Berlin, Heidelberg, 1993. ISBN 978-3-662-02781-3. doi:10.1007/978-3-662-02781-3_35.

[55] Madan Lal Mehta. *Random matrices*, volume 142. Elsevier, 2004.

[56] Fred Jendrzejewski, Alain Bernard, Killian Mueller, Patrick Cheinet, Vincent Josse, Marie Piraud, Luca Pezzé, Laurent Sanchez-Palencia, Alain Aspect, and Philippe Bouyer. Three-dimensional localization of ultracold atoms in an optical disordered potential. *Nature Physics*, 8(5):398, 2012.

[57] Maksym Serbyn and Dmitry A. Abanin. Loschmidt echo in many-body localized phases. *Phys. Rev. B*, 96:014202, Jul 2017. doi:10.1103/PhysRevB.96.014202.

[58] Daniel A. Lidar and K. Birgitta Whaley. *Decoherence-Free Subspaces and Subsystems*, pages 83–120. Springer Berlin Heidelberg, Berlin, Heidelberg, 2003. ISBN 978-3-540-44874-7. doi:10.1007/3-540-44874-8_5.

[59] J. Martin, B. Georgeot, and D. L. Shepelyansky. Time reversal of bose-einstein condensates. *Phys. Rev. Lett.*, 101:074102, Aug 2008. doi:10.1103/PhysRevLett.101.074102.

[60] E. L. Hahn. Spin echoes. *Phys. Rev.*, 80:580–594, Nov 1950. doi:10.1103/PhysRev.80.580.

[61] Fernando M. Cucchietti. Time reversal in an optical lattice. *J. Opt. Soc. Am. B*, 27(6):A30–A35, Jun 2010. doi:10.1364/JOSAB.27.000A30.

[62] W-K. Rhim, A. Pines, and J. S. Waugh. Time-reversal experiments in dipolar-coupled spin systems. *Phys. Rev. B*, 3:684–696, Feb 1971. doi:10.1103/PhysRevB.3.684.

[63] F. Andraschko and J. Sirker. Dynamical quantum phase transitions and the loschmidt echo: A transfer matrix approach. *Phys. Rev. B*, 89:125120, Mar 2014. doi:10.1103/PhysRevB.89.125120.

[64] D Bacon. Decoherence, control, and symmetry in quantum computers. *arXiv preprint quant-ph/0305025*, 2003.

[65] Wojciech Hubert Zurek. Decoherence, einselection, and the quantum origins of the classical. *Rev. Mod. Phys.*, 75:715–775, May 2003. doi:10.1103/RevModPhys.75.715.

[66] C. N. Yang and C. P. Yang. One-dimensional chain of anisotropic spin-spin interactions. i. proof of bethe's hypothesis for ground state in a finite system. *Phys. Rev.*, 150:321–327, Oct 1966. doi:10.1103/PhysRev.150.321.

[67] Alexander L. Fetter and John Dirk. Walecka. *Quantum theory of many-particle systems*. Dover Publications, 2003.

[68] Jun J. Sakurai and Jim Napolitano. *Modern Quantum Mechanics*. Cambridge University Press, 2017.

[69] Marcos Rigol, Vanja Dunjko, and Maxim Olshanii. Thermalization and its mechanism for generic isolated quantum systems. *Nature*, 452(7189):854, 2008.

[70] Mark Srednicki. Chaos and quantum thermalization. *Phys. Rev. E*, 50:888–901, Aug 1994. doi:10.1103/PhysRevE.50.888.

[71] J. M. Deutsch. Quantum statistical mechanics in a closed system. *Phys. Rev. A*, 43:2046–2049, Feb 1991. doi:10.1103/PhysRevA.43.2046.

[72] Ehud Altman and Ronen Vosk. Universal dynamics and renormalization in many-body-localized systems. *Annu. Rev. Condens. Matter Phys.*, 6(1): 383–409, 2015. doi:10.1146/annurev-conmatphys-031214-014701.

[73] Adam M Kaufman, M Eric Tai, Alexander Lukin, Matthew Rispoli, Robert Schittko, Philipp M Preiss, and Markus Greiner. Quantum thermalization through entanglement in an isolated many-body system. *Science*, 353(6301): 794–800, 2016.

[74] Neil W Ashcroft. *Solid state physics / Neil W. Ashcroft, N. David Mermin.* –. Saunders College, Philadelphia, 1976. ISBN 0030839939.

[75] JT Edwards and DJ Thouless. Numerical studies of localization in disordered systems. *Journal of Physics C: Solid State Physics*, 5(8):807, 1972.

[76] E. Abrahams, P. W. Anderson, D. C. Licciardello, and T. V. Ramakrishnan. Scaling theory of localization: Absence of quantum diffusion in two dimensions. *Phys. Rev. Lett.*, 42:673–676, Mar 1979. doi:10.1103/PhysRevLett.42.673.

[77] D.M. Basko. Metal-insulator transition in a weakly interacting many-electron system with localized single-particle states. *Annals of Physics*, 321(5), 2006. ISSN 0003-4916.

[78] Cord A Müller and Dominique Delande. Disorder and interference: localization phenomena. *arXiv preprint arXiv:1005.0915*, 2010.

[79] Rachida Dalichaouch, JP Armstrong, Sheldon Schultz, PM Platzman, and SL McCall. Microwave localization by two-dimensional random scattering. *Nature*, 354(6348):53, 1991.

[80] AA Chabanov, M Stoytchev, and AZ Genack. Statistical signatures of photon localization. *Nature*, 404(6780):850, 2000.

[81] RL Weaver. Anderson localization of ultrasound. *Wave motion*, 12(2):129–142, 1990.

[82] Eric Akkermans and Gilles Montambaux. *Mesoscopic physics of electrons and photons*. Cambridge university press, 2007.

[83] Juliette Billy, Vincent Josse, Zhanchun Zuo, Alain Bernard, Ben Hambrecht, Pierre Lugan, David Clément, Laurent Sanchez-Palencia, Philippe Bouyer, and Alain Aspect. Direct observation of anderson localization of matter waves in a controlled disorder. *Nature*, 453(7197):891, 2008.

[84] S Inouye, MR Andrews, J Stenger, H-J Miesner, DM Stamper-Kurn, and W Ketterle. Observation of feshbach resonances in a bose–einstein condensate. *Nature*, 392(6672):151, 1998.

[85] Denis M Basko, Igor L Aleiner, and Boris L Altshuler. Metal–insulator transition in a weakly interacting many-electron system with localized single-particle states. *Annals of physics*, 321(5):1126–1205, 2006.

[86] Maksym Serbyn, Z Papić, and Dmitry A Abanin. Universal slow growth of entanglement in interacting strongly disordered systems. *Physical review letters*, 110(26):260601, 2013.

[87] Maksym Serbyn, Z Papić, and Dmitry A Abanin. Local conservation laws and the structure of the many-body localized states. *Physical review letters*, 111(12):127201, 2013.

[88] David A Huse, Rahul Nandkishore, and Vadim Oganesyan. Phenomenology of fully many-body-localized systems. *Phys. Rev. B*, 90(17):174202, 2014.

[89] M Serbyn, Michael Knap, Sarang Gopalakrishnan, Z Papić, Norman Ying Yao, CR Laumann, DA Abanin, Mikhail D Lukin, and Eugene A Demler. Interferometric probes of many-body localization. *Physical review letters*, 113(14):147204, 2014.

[90] Maksym Serbyn, Z. Papić, and Dmitry A. Abanin. Local conservation laws and the structure of the many-body localized states. *Phys. Rev. Lett.*, 111: 127201, Sep 2013. doi:10.1103/PhysRevLett.111.127201.

[91] David A. Huse, Rahul Nandkishore, and Vadim Oganesyan. Phenomenology of fully many-body-localized systems. *Phys. Rev. B*, 90:174202, Nov 2014. doi:10.1103/PhysRevB.90.174202.

[92] Bela Bauer and Chetan Nayak. Area laws in a many-body localized state and its implications for topological order. *Journal of Statistical Mechanics: Theory and Experiment*, 2013(09):P09005, 2013.

[93] W. P. Su, J. R. Schrieffer, and A. J. Heeger. Solitons in polyacetylene. *Phys. Rev. Lett.*, 42:1698–1701, Jun 1979. doi:10.1103/PhysRevLett.42.1698.

[94] Eric J. Meier, Fangzhao Alex An, and Bryce Gadway. Observation of the topological soliton state in the su–schrieffer–heeger model. *Nature Communications*, 7, 2016. ISSN 2041-1723.

[95] Alan J. Heeger. Nobel lecture: Semiconducting and metallic polymers: The fourth generation of polymeric materials. *Rev. Mod. Phys.*, 73:681–700, Sep 2001. doi:10.1103/RevModPhys.73.681.

[96] John Hubbard. Electron correlations in narrow energy bands. *Proc. R. Soc. Lond. A*, 276(1365):238–257, 1963.

[97] Martin C Gutzwiller. Effect of correlation on the ferromagnetism of transition metals. *Phys. Rev. Lett.*, 10(5):159, 1963.

[98] Junjiro Kanamori. Electron correlation and ferromagnetism of transition metals. *Progress of Theoretical Physics*, 30(3):275–289, 1963.

[99] Philip W Anderson. New approach to the theory of superexchange interactions. *Phys. Rev.*, 115(1):2, 1959.

[100] Stephen Blundell. *Magnetism in Condensed Matter*. Oxford University Press, 2014. ISBN 9780198505914.

[101] Rodney J Baxter. *Exactly solved models in statistical mechanics / Rodney J. Baxter*. Dover Publications, Mineola, N.Y., dover ed.. edition, 2007. ISBN 9780486462714.

[102] Hans Bethe. Zur theorie der metalle. *Zeitschrift für Physik*, 71(3-4):205–226, 1931.

[103] Jacques Des Cloizeaux and JJ1 Pearson. Spin-wave spectrum of the antiferromagnetic linear chain. *Phys. Rev.*, 128(5):2131, 1962.

[104] C. N. Yang and C. P. Yang. One-dimensional chain of anisotropic spin-spin interactions. i. proof of bethe's hypothesis for ground state in a finite system. *Phys. Rev.*, 150:321–327, Oct 1966. doi:10.1103/PhysRev.150.321.

[105] C. N. Yang and C. P. Yang. One-dimensional chain of anisotropic spin-spin interactions. ii. properties of the ground-state energy per lattice site for an infinite system. *Phys. Rev.*, 150:327–339, Oct 1966. doi:10.1103/PhysRev.150.327.

[106] C. N. Yang and C. P. Yang. One-dimensional chain of anisotropic spin-spin interactions. iii. applications. *Phys. Rev.*, 151:258–264, Nov 1966. doi:10.1103/PhysRev.151.258.

[107] Rodney J Baxter. One-dimensional anisotropic heisenberg chain. *Annals of Physics*, 70(2):323–337, 1972.

[108] Rodney J Baxter. Partition function of the eight-vertex lattice model. *Annals of Physics*, 70(1):193–228, 1972.

[109] Michael Karabach, Gerhard Müller, Harvey Gould, and Jan Tobochnik. Introduction to the bethe ansatz i. *Computers in Physics*, 11(1):36–43, 1997.

[110] Fabio Franchini. *An introduction to integrable techniques for one-dimensional quantum systems*, volume 940. Springer, 2017.

[111] E. Lieb, T. Schultz, and D. Mattis. Two soluble models of an antiferromagnetic chain. *Annals of Physics*, 16:407–466, December 1961. doi:10.1016/0003-4916(61)90115-4.

[112] Ping Lu, Gerhard Muller, and Michael Karbach. Quasiparticles in the xxz model. *arXiv preprint arXiv:0909.2728*, 2009.

[113] Alexander Weiße and Holger Fehske. *Exact Diagonalization Techniques*, pages 529–544. Springer Berlin Heidelberg, Berlin, Heidelberg, 2008. ISBN 978-3-540-74686-7. doi:10.1007/978-3-540-74686-7_18.

[114] N Sedlmayr, P Jaeger, M Maiti, and J Sirker. Bulk-boundary correspondence for dynamical phase transitions in one-dimensional topological insulators and superconductors. *Phys. Rev. B*, 97(6):064304, 2018.

[115] F. Andraschko and J. Sirker. Dynamical quantum phase transitions and the loschmidt echo: A transfer matrix approach. 89(12), December 2013. ISSN 1098-0121.

[116] C. N. Yang and T. D. Lee. Statistical theory of equations of state and phase transitions. i. theory of condensation. *Phys. Rev.*, 87:404–409, Aug 1952. doi:10.1103/PhysRev.87.404.

[117] Konrad Knopp. *Theory of functions / by Konrad Knopp ; translated by Frederick Bagemihl.* Dover Publications, New York, 2nd american ed.. edition, 1996.

[118] Michael E Fisher. The theory of condensation and the critical point. *Physics Physique Fizika*, 3(5):255, 1967.

[119] Ioana Bena, Michel Droz, and Adam Lipowski. Statistical mechanics of equilibrium and nonequilibrium phase transitions: the yang–lee formalism. *International Journal of Modern Physics B*, 19(29):4269–4329, 2005.

[120] Gerald L Jones. Complex temperatures and phase transitions. *Journal of Mathematical Physics*, 7(11):2000–2005, 1966.

[121] Chanchal K Majumdar. Analytic properties of the onsager solution of the ising model. *Phys. Rev.*, 145(1):158, 1966.

[122] S Grossmann and W Rosenhauer. Temperature dependence near phase transitions in classical and quant. mech. canonical statistics. *Zeitschrift für Physik*, 207(2):138–152, 1967.

[123] Ryuzo Abe. Logarithmic singularity of specific heat near the transition point in the ising model. *Progress of Theoretical Physics*, 37(6):1070–1079, 1967.

[124] Ryuzo Abe. Singularity of specific heat in the second order phase transition. *Progress of Theoretical Physics*, 38(2):322–331, 1967.

[125] S Grossmann. Phase transitions and distribution of zeros in the complex temperature plane. *Physics Letters A*, 28(2):162–163, 1968.

[126] S Grossmann and W Rosenhauer. Phase transitions and the distribution of temperature zeros of the partition function. *Zeitschrift für Physik A Hadrons and nuclei*, 218(5):437–448, 1969.

[127] Xinhua Peng, Hui Zhou, Bo-Bo Wei, Jiangyu Cui, Jiangfeng Du, and Ren-Bao Liu. Experimental observation of lee-yang zeros. *Phys. Rev. Lett.*, 114: 010601, Jan 2015. doi:10.1103/PhysRevLett.114.010601.

[128] Kay Brandner, Ville F. Maisi, Jukka P. Pekola, Juan P. Garrahan, and Christian Flindt. Experimental determination of dynamical lee-yang zeros. *Phys. Rev. Lett.*, 118:180601, May 2017. doi:10.1103/PhysRevLett.118.180601.

[129] Markus Heyl, Anatoli Polkovnikov, and Stefan Kehrein. Dynamical quantum phase transitions in the transverse-field ising model. *Physical review letters*, 110(13):135704, 2013.

[130] André LeClair, Giuseppe Mussardo, H Saleur, and S Skorik. Boundary energy and boundary states in integrable quantum field theories. *Nuclear Physics B*, 453(3):581–618, 1995.

[131] Markus Heyl. Quenching a quantum critical state by the order parameter: Dynamical quantum phase transitions and quantum speed limits. *Phys. Rev. B*, 95:060504, Feb 2017. doi:10.1103/PhysRevB.95.060504.

[132] D.L. Shepelyansky. Some statistical properties of simple classically stochastic quantum systems. *Physica D: Nonlinear Phenomena*, 8(1):208 – 222, 1983. ISSN 0167-2789. doi:10.1016/0167-2789(83)90318-4.

[133] G. Casati, B. V. Chirikov, I. Guarneri, and D. L. Shepelyansky. Dynamical stability of quantum "chaotic" motion in a hydrogen atom. *Phys. Rev. Lett.*, 56:2437–2440, Jun 1986. doi:10.1103/PhysRevLett.56.2437.

[134] Shmuel Fishman, D. R. Grempel, and R. E. Prange. Chaos, quantum recurrences, and anderson localization. *Phys. Rev. Lett.*, 49:509–512, Aug 1982. doi:10.1103/PhysRevLett.49.509.

[135] D. R. Grempel, R. E. Prange, and Shmuel Fishman. Quantum dynamics of a nonintegrable system. *Phys. Rev. A*, 29:1639–1647, Apr 1984. doi:10.1103/PhysRevA.29.1639.

[136] Wojciech Hubert Zurek. Sub-planck spots of schroedinger cats and quantum decoherence. January 2002.

[137] Ph. Jacquod, P.G. Silvestrov, and C.W.J. Beenakker. Golden rule decay versus lyapunov decay of the quantum loschmidt echo. *Phys. Rev. E*, 64: 055203, Oct 2001. doi:10.1103/PhysRevE.64.055203.

[138] Rodolfo A. Jalabert and Horacio M. Pastawski. Environment-independent decoherence rate in classically chaotic systems. *Phys. Rev. Lett.*, 86:2490–2493, Mar 2001. doi:10.1103/PhysRevLett.86.2490.

[139] Atanu Rajak and Uma Divakaran. Effect of double local quenches on the loschmidt echo and entanglement entropy of a one-dimensional quantum system. *Journal of Statistical Mechanics: Theory and Experiment*, 2016(4), April 2016. ISSN 1742-5468.

[140] Davide Rossini, Tommaso Calarco, Vittorio Giovannetti, Simone Montangero, and Rosario Fazio. Decoherence induced by interacting quantum spin baths. *Phys. Rev. A*, 75:032333, Mar 2007. doi:10.1103/PhysRevA.75.032333.

[141] Leonid S. Levitov, Hyunwoo Lee, and Gordey B. Lesovik. Electron counting statistics and coherent states of electric current. *Journal of Mathematical Physics*, 37(10):4845–4866, 1996. doi:10.1063/1.531672. URL https://doi.org/10.1063/1.531672.

[142] I. Klich. Full counting statistics: An elementary derivation of levitov's formula. September 2002.

[143] H. T. Quan, Z. Song, X. F. Liu, P. Zanardi, and C. P. Sun. Decay of loschmidt echo enhanced by quantum criticality. *Phys. Rev. Lett.*, 96:140604, Apr 2006. doi:10.1103/PhysRevLett.96.140604.

[144] Szabolcs Vajna and Balázs Dóra. Topological classification of dynamical phase transitions. *Phys. Rev. B*, 91:155127, Apr 2015. doi:10.1103/PhysRevB.91.155127.

[145] Ronen Vosk and Ehud Altman. Many-body localization in one dimension as a dynamical renormalization group fixed point. *Physical review letters*, 110 (6):067204, 2013.

[146] Romain Vasseur, Aaron J Friedman, SA Parameswaran, and Andrew C Potter. Particle-hole symmetry, many-body localization, and topological edge modes. *Phys. Rev. B*, 93(13):134207, 2016.

[147] D. N. Aristov. Bosonization for wigner-jordan-like transformation : Backscattering and umklapp-processes on fictitious lattice. 57(20), March 1998. ISSN 0163-1829.